creative commons
COMMONS DEED

저작자표시-비영리-변경금지 2.0 대한민국

이용자는 아래의 조건을 따르는 경우에 한하여 자유롭게

- 이 저작물을 복제, 배포, 전송, 전시, 공연 및 방송할 수 있습니다.

다음과 같은 조건을 따라야 합니다:

저작자표시. 귀하는 원저작자를 표시하여야 합니다.

비영리. 귀하는 이 저작물을 영리 목적으로 이용할 수 없습니다.

변경금지. 귀하는 이 저작물을 개작, 변형 또는 가공할 수 없습니다.

- 귀하는, 이 저작물의 재이용이나 배포의 경우, 이 저작물에 적용된 이용허락조건을 명확하게 나타내어야 합니다.
- 저작권자로부터 별도의 허가를 받으면 이러한 조건들은 적용되지 않습니다.

저작권법에 따른 이용자의 권리는 위의 내용에 의하여 영향을 받지 않습니다.

이것은 이용허락규약(Legal Code)을 이해하기 쉽게 요약한 것입니다.

Disclaimer

dCollection

Ph.D. DISSERTATION

Development of Implantable Electronics as Novel Approaches to Obstructive Sleep Apnea

폐쇄성 수면 무호흡에 대한

새로운 접근법으로써의 이식형 전자 장치 개발

BY

Jungmin Seo

AUGUST 2019

DEPARTMENT OF ELECTRICAL
AND COMPUTER ENGINEERING
COLLEGE OF ENGINEERING
SEOUL NATIONAL UNIVERSITY

Development of Implantable Electronics as Novel Approaches to Obstructive Sleep Apnea

지도교수 김 성 준

이 논문을 공학박사 학위 논문으로 제출함

2019년 8월

서울대학교 대학원

전기·정보공학부

서 정 민

서 정 민의 공학 박사 학위 논문을 인준함

2019년 8월

위 원 장 남 상 욱 (인)

부위원장 김 성 준 (인)

위 원 김 정 훈 (인)

위 원 최 진 우 (인)

위 원 정 준 수 (인)

ABSTRACT

Obstructive sleep apnea (OSA) is a disorder with high prevalence that 13 % of men and 6 % of women in North America suffer from. It is often regarded as a mere discomfort at night though, chronic OSA may involve sequelae such as insulin resistance, vascular diseases, and impaired quality of life due to excessive sleepiness. Although there are existing therapies such as continuous positive airway pressure (CPAP), oral appliances, and surgical operations, those therapies are not applicable to some patients due to low effectiveness, low adherence, or high invasiveness. Therefore, it is necessary to develop break-through therapies which can overcome the limitations of the conventional therapies.

In this dissertation, two implantable electronic devices are suggested as novel approaches to treat OSA. They provide unique methods to retain patency of the retrolingual and the retropalatal region which are considered as main contributors to pharyngeal collapse. First, a magnetic cuff system was designed and fabricated for stimulating the hypoglossal nerve which the innervates the extrinsic tongue muscle, the genioglossus. The system consists of a magnet-embedded nerve cuff electrode and a stimulation pulse generator. The substrate material used for the electrode is a liquid crystal polymer (LCP), characterized by properties of biocompatible, flexible, and near-hermetic. The electrode can be easily installed on and removed from the nerve repeatedly, owing to magnetic forces of the embedded rare-earth magnets. To demonstrate feasibilities of the system in hypoglossal nerve

stimulation, *in vivo* as well as *in vitro* evaluations were conducted. Electrochemical impedance spectroscopy (EIS) was measured in a PBS solution using a three-electrode cell to figure out magnitude and phase of the impedance in the frequency ranging 1 Hz− 100 kHz. The electrode was further evaluated *in vivo* to stimulate the hypoglossal nerve of a rabbit. With the applied stimulation, protrusion of the tongue and the contraction of the genioglossus was observed with bare eyes and C-arm fluoroscopy respectively.

A preliminary study was conducted to figure out the effect of the electrical stimulation on the retropalatal opening under a hypothesis that the electrical stimuli contracts the soft palate. Through the study, elevation of the soft palate was shown via a C-arm fluoroscopy with stimulation pulse parameters of 1.00 mA, 636 μs, and 100 Hz for an amplitude, duration, and frequency, respectively.

Based on the finding, a palatal implant system was designed and fabricated. The system consists of two main parts, an intra-oral device that receives stimulation parameters via ZigBee from an external controller and an implant that receives power and data from the intra-oral device via an inductive link. The intra-oral device has a shape of a mouth-piece to easily get equipped in the mouth and the whole device is packaged by a silicone elastomer. The implant consists of multiple LCP sheets on which metals composing a coil, circuit, and electrode pattern are patterned.

To evaluate wireless performance of the fabricated system, power-related terms such as a total power efficiency, supplied/received power, and received peak

voltage were measured varying the distance between the transmitter and the receiver antenna coils. An averaged duty-cycle error of recovered PWM signals at the receiver was also calculated based on the measurement in the range of the distances to evaluate data telemetry of the wireless transmission. Further assessments were conducted *in vitro* to demonstrate feasibility of the stimulation electrodes in a metal-electrolyte interface using a PBS solution. Impedance, charge storage capacity, and charge injection capacity of the fabricated electrode were obtained and analyzed using an electrochemical impedance spectroscopy. After the evaluations, the system was applied to a rabbit and the soft palate stimulation was conducted *in vivo*. As expected, contraction of the soft palate was shown via a C-arm fluoroscopy when the electrical stimulation was applied. Finally, several discussions on the developed devices were addressed.

Keywords: obstructive sleep apnea, implantable electronics, liquid crystal polymer, hypoglossal nerve stimulation, soft palate stimulation, inductive link

Student Number: 2014-21648

CONTENTS

List of Figures

List of Tables

List of Abbreviations

Abbreviation	Term
ASIC	Application-Specific Integrated Circuit
CPAP	Continuous Positive Airway Pressure
EMG	Electromyogram
FEM	Finite Element Method
FFC	Flexible Flat Cable
HNS	Hypoglossal Nerve Stimulation
IC	Integrated Circuit
IOD	Intra-Oral Device
LAUP	Laser-Assisted Uvuloplatoplasty (LAUP)
LCP	Liquid Crystal Polymer
MAD	Mandibular Advancement Device
MENCE	Magnet-Embedded Nerve Cuff Electrode
MMA	Maxilo-Mandibular Advancement
OSA	Obstructive Sleep Apnea
PCB	Printed Circuit Board
PWM	Pulse-Width Modulation
SPICE	Simulation Program with Integrated Circuit Emphasis
SPS	Soft Palate Stimulation
UPPP	Uvulopalatopharyngoplasty

◆ Note

Some parts of this dissertation are extracted and adapted from the following publications which were published during the course of this study:

- Seo, J., Wee, J. H., Park, J. H., Park, P., Kim, J. W., & Kim, S. J. (2016). Nerve cuff electrode using embedded magnets and its application to hypoglossal nerve stimulation. Journal of neural engineering, 13(6), 066014.

- Seo, J., Kim, J. W., Cho, S. W., Shim, S., Choi, J. W., & Kim, S. J. (2018, July). Preliminary Study of Palatal Implant for Sleep Apnea Control. In 2018 40th Annual International Conference of the IEEE Engineering in Medicine and Biology Society (EMBC) (pp. 1498-1501). IEEE.

Chapter 1

Introduction

1.1. Obstructive Sleep Apnea (OSA)

Obstructive sleep apnea (OSA) is becoming a common disease in the modern society, reported that 13 % of men and 6 % of women suffer from OSA in North America [1]. Easily confused with snoring, OSA is often overlooked as a mere discomfort at night. However, persistent OSA may lower a quality of life with excessive sleepiness and chronic fatigue. Patients having an apnea-hypopnea index (AHI), the number of apnea or hypopnea occurred per night hour, of 15 or more may suffer critical sequelae such as insulin resistance, dyslipidemia, vascular disease, and even death [2]. Therefore, it is important to apply effective therapies consistently to patients for treating OSA.

1.1.1. Pathogenesis of OSA

Obstructive sleep apnea (OSA) is the most common type of sleep apnea. It is caused by partial or complete obstruction of the upper airway due to the surrounding muscles of the pharynx, regardless of respiratory effort of the lung. There are forces that promotes the upper-airway collapse such as intraluminal negative pressure, surface tension, and gravity, while tonic and phasic activity of muscles and wakefulness are the examples that contribute to the airway patency [3]. The forces applied to the surrounding muscles are balanced in normal, so that the upper airway does not collapse as shown in the left figure in Figure 1.1.1. However, the upper airway collapse is mainly involved in either/both the retrolingual or/and the retropalatal region when the balance of the forces is broken, as shown in the

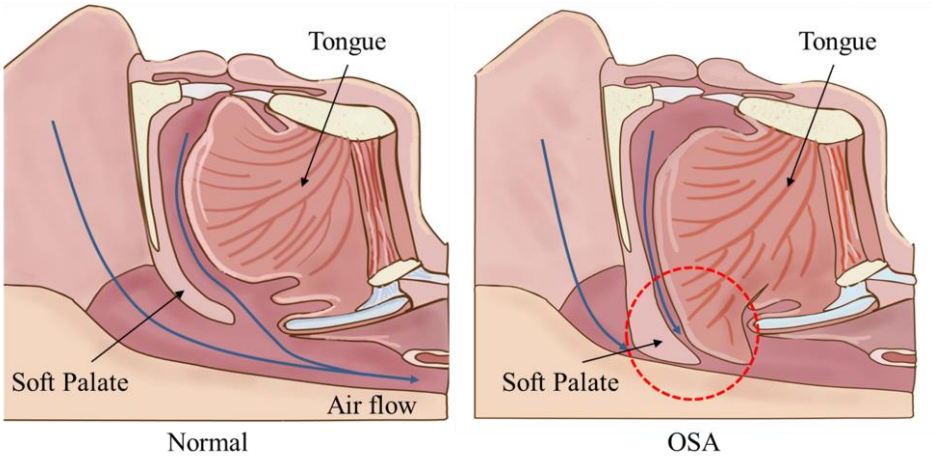

Figure 1.1.1 Illustrations of the upper airway and its surrounding muscles in case of normal (left) and OSA (right).

right figure in Figure 1.1.1. Therefore, for an effective treatment, it is necessary to figure out first where the collapse has occurred and then to provide an appropriate therapy. Retrolingual opening can be accomplished by modifying position of the tongue and retropalatal opening can be accomplished by modifying position or stiffness of the soft palate.

1.1.2. Conventional Therapies

As stated in 1.1.1., two major pharyngeal muscles, the tongue and the soft palate, are the main contributors to the pharyngeal collapse. Continuous positive airway pressure (CPAP) helps maintaining patency at both retrolingual and retropalatal regions by supplying pressurized air. Maxilomandibular advancement (MMA), mandibular advancement device (MAD), and oral appliances are the therapies that open the retrolingual region by modifying the tongue position. Uvulopharyngopalatoplasty (UPPP), laser assisted uvulopalatoplasty (LAUP), and

pillar implants are therapies related to the soft palate modification for retropalatal opening. Detailed explanations of the therapies are following in 1.1.2.1 and 1.1.2.2.

1.1.2.1. Continuous Positive Airway Pressure

Continuous positive airway pressure (CPAP) is the most popular therapy owing to its non-invasiveness and high efficacy. CPAP delivers positively pressurized air into the upper airway via a nasal mask and a tube connected to a pump, thereby patency of the upper airway can be recovered by pushing out collapsed muscles from the upper airway [4]. CPAP has been reported to be very effective if correctly applied with an acceptable usage rate, over 4 hours per night [5]. However, it also has been reported that under 50 % of patients use CPAP over 4 hours per night after 6 months and the percentage of patients drops to 17 % after 5 years, due to discomfort and inconvenience in using CPAP [6, 7]. The poor adherence lowers effectiveness of the CPAP therapy considering that the effectiveness of the therapy can be expressed in product of efficacy and adherence of patients to the therapy.

1.1.2.2. Therapies of Tongue-related OSA

Therapies of the tongue-related OSA focus on recovering retrolingual patency by modifying position of the tongue. Maxilomandibular advancement (MMA), an orthognathic surgery that includes advancement of the mandible, is a surgical operation to the tongue-related OSA patients. Often performed simultaneously with Genioglossus advancement (GA), MMA has been

demonstrated to be one of the most effective therapy for treating sleep apnea having AHI reduction of 87 % [8]. However, MMA has been reported to accompany negative functional changes as well as cosmetic changes after the operation. Significant percentages (20– 50 %) of patients presented disorders related to the masticatory apparatus, gum pain, dental wear, and long-lasting postoperative sensory disorders. Furthermore, 89.4 % of patients reported changes in their facial appearances and 18.3 % were unsatisfied with their changed faces [9].

An oral appliance is a mouth-equipping device during sleep to advance position of the mandible and thereby, advances the tongue as well. As the appliance is non-invasive and easily applicable, it is recommended to patients who failed to adhere to the CPAP treatment. The average efficacy of the oral appliances is reported to be 45 %, which is far lower than that of CPAP, 87 %. However, the average adherence is 95 %, while the adherence remains under 50 % for CPAP treatment [10, 11]. The excellent adherence of the oral appliance compensates the poor efficacy of the oral appliance treatment, making the therapy comparably effective to the CPAP.

1.1.2.3. Therapies of Palate-related OSA

Uvulopharyngopalatoplasty (UPPP) is a commonly performed surgical procedure for retropalatal opening. UPPP involves removal and rearrangement of the tonsils, adenoids, uvula, soft palate, and pharynx to increase the upper airway size and thereby tissue collapse can be prevented [12]. Laser-assisted uvulopalatoplasty (LAUP), similar to UPPP regarding removal of the upper airway

tissues, utilizes a laser to vaporize the uvula or a specified portion of tissues under local anesthesia. Both UPPP and LAUP are direct methods to remove the excessive tissues, but there are a few side-effects reported: respiratory compromise, bleeding, and death in 0 % to 16 % of patients [13-16]. Persistent side-effects were also reported in a mean of 59 %, including difficulty in swallowing, globus sensation, voice changes, smell disturbances, and velopharyngeal stenosis after LAUP [17-22]. To say about efficacy, 20 % decrease in the mean AHI was reported for LAUP, and 24 % to 33 % for UPPP, which are not satisfactory results considering possibilities of the side-effects [23, 24].

Pillar implant system (Medtronic, USA), introduced as a simple treatment for snoring in 2003, enhances stiffness of the soft palate through a mechanical support [25, 26]. Three pillars are implanted into the soft palate to support the soft palate, achieving submucosal thickening by creating fibrotic capsules around the implants. Easy implantation procedure under local anesthesia in an office environment is a significant advantage of the pillar implant. However, efficacy of the pillar implant has been reported to be limited [27, 28]. According to Server *et al.*, no statistically significant differences on the Epwort sleepiness scale (ESS) and AHI were detected while the average of the visual analog scale (VAS) was decreased by only 18.1 % [29]. The low efficacy seems to be due to the pillars' passive supporting, not an active contraction of the muscle.

1.2. Electrical Stimulation for OSA treatment

As mentioned in 1.1.2., the conventional therapies have their own

shortcomings. Therefore, there is a necessity to develop a new treatment method that overcomes such drawbacks. Here we suggest an electrical stimulation as an alternative treatment method for OSA.

1.2.1. Neural and Neuromuscular stimulation

Nerves represent their firing data in polarized voltages, called action potentials, across their membranes. When the firing data are delivered to the innervating sensory or motor cells, their corresponding functions appear. Therefore, the functions can be modulated by forcing the polarization of the membrane potential using electric pulses. There have been many neuro-prosthetic devices developed using principle of neuromodulation. Cochlear implants are appraised to be one of the most successful neural prostheses until now [30-33]. The implant substitutes impaired hair cells, which play role in transducing sounds to electric pulses, by applying electric stimulation to the cochlea's hearing nerve. A retinal implant takes a similar strategy but to stimulate the retina's optic nerve [34-36]. There are further neural prostheses such as a spinal cord stimulation, deep brain stimulation, and hypoglossal nerve stimulation to modulate certain neural functions [37-41].

Neuromuscular stimulation induces muscle contraction using electric pulses similar to that used in the neural prostheses. The pulses mimic action potentials from the central nerve system, causing the muscles to contract by stimulating either innervating nerves or neuromuscular junction. The neuromuscular stimulation has been used for clinical applications to provide either

a functional or therapeutic effect. The functional neuromuscular stimulation includes activation of paralyzed muscles, support of standing or ambulatory activities, or control of respiration and bladder function [42-46]. The therapeutic effect of the neuromuscular stimulation contains motor relearning referring recovery of motor skills that have been lost due to damage to the central nerve system [47, 48].

1.2.2. Hypoglossal Nerve Stimulation (HNS)

With the advances of neural prostheses, a hypoglossal nerve stimulation has been developed to treat OSA by stimulating the innervating nerve of the genioglossus, the extrinsic muscle of the tongue, to accomplish retrolingual opening. In 1980, Brouillette *et al.* firstly found that control of the genioglossus, the extrinsic muscle of the tongue, may contribute to inspiratory activity [49]. Inspired by the possibility, a hypoglossal nerve stimulation has been investigated from the late 90's, under the fact that the hypoglossal nerve innervates to the genioglossus [50-53]. Recently, a clinical study using an implantable hypoglossal nerve stimulator (Inspire Medical Systems, USA), was reported in *New England Journal of Medicine* to announce that median AHI score at 12 months decreased by 68 %, from 29.3 events per hour to 9.0 events per hour with the overall rate of series adverse events less than 2 %, through a 12-month follow-up on patients using the stimulator [38]. Furthermore, an interesting phenomenon has been found through other clinical studies that the hypoglossal nerve stimulation also induces retropalatal opening despite the fact that the stimulation originally targets the

retrolingual opening. This phenomenon, called palatoglossus coupling, is due to palatoglossus muscle that connects the anterior pillar from the uvula and the sides of the tongue. The elicited coupling was reported to exist in nearly 80 % of patients implying possibility of multi-region opening from the single stimulation on those population [54].

1.2.3. Soft Palate Stimulation (SPS)

The palatal muscles play an important role in the upper-airway patency considering that the pharyngeal collapse often occurs in the velopharyngeal region [55]. The palatal muscles consist of five major muscles parts: the muscles controlling the stiffness (*tensor veli palatini*) and position (*levator veli palatini*) of the palate, tongue (palatoglossus), pharynx (palatopharyngeus), and the shape of the uvula (musculus uvulae).

Despite the importance of the palatal muscles to upper-airway obstruction, few trials were conducted to control those muscles due to their harder accessibility compared to the genioglossus. In 1996, Schwartz conducted a study to figure out whether an electrical stimulation to the soft palate has effect on ceasing either snoring or OSA [56]. Seven men between the ages of 35 and 49 were selected from a pool of patients who were diagnosed as sleep apnea with snoring. Oral appliances used in the study had two wire electrodes and voltage pulses were applied to the soft palate via the electrodes. The result showed that 25 % of patients experienced cessation of snoring and varied effects on OSA with voltage amplitude of 2.5− 9.0 V, without arousal. More sophisticated experiment was conducted by selective

stimulation of the *tensor veli palatini* muscle while monitoring the upper airway patency represented in critical pressure. There was a significant reduction in the critical pressure, indicating therapeutic effect of the palatal stimulation for the OSA treatment [57].

1.3. Suggested Approaches

Here we suggest two novel approaches for OSA treatments as alternatives to the conventional therapies. In this thesis, two implantable electronics are suggested, each of which is for retrolingual opening and retropalatal opening, respectively. First, an introduction is provided about the biocompatible polymer used in the devices, and then brief descriptions of the devices are following.

1.3.1. Liquid Crystal Polymer (LCP)

The suggested devices are implantable electronics that should remain in the body for a long time. Therefore, it is important to use a biocompatible and hermetic material which allows the device to stay safe and stable in the body. Metals have been widely used as packaging materials for implantable devices. Among them, titanium is a very popular material until now as it provides long-term biocompatibility and resistant to corrosion by the body fluid when alloyed with other elements. However, there are a few problems of using metal packages. First, the metal packages cannot be fabricated as light and small as other packages, specifically polymers. The bulky and heavy package are usually placed in the chest

where plenty space exists. Therefore, it essentially requires long connection lines to stimulation electrodes which are far from the package. This involves an invasive operation to place the connection lines under the skin. Furthermore, as the metal packages cannot be monolithically integrated with the electrodes, there are hermeticity issues on the feed-throughs. The hetero-junction of the lead-lines and the package increases the possibility of device failure at the feed-through.

Polymers are another material options for packaging implantable devices. Polyimide, parylene-C, silicone elastomer, and liquid crystal polymer (LCP) are such polymers, all of which are frequently utilized as the packaging materials. Among them, LCP has extremely low water absorption under 0.04 %, which is the value one hundred times lower than that of the polyimide at maximum [58]. Due to its high hermeticity over the other polymers, LCP is regarded as a suitable material for polymer packaging. Another strong point of using LCP is that the entire implantable device, including the electrodes, connection lines, feed-throughs, and the pulse generators, can be fabricated and packaged monolithically. Prior arts of LCP-based retinal implant devices, cochlear implants, and depth probes have been

	LCP (Vecstar)	**Polyimide (PI2525)**	**PDMS**
Melting Temp. (°C)	**280~335**	>400	200-250
Tensile Strength (MPa)	**270~500**	128	2.24
Young's Modulus (GPa)	**2~10**	1.8−15	0.1−0.87
Water absorption (%)	**< 0.04**	0.24−4	0.1−1.3
Dielectric Constant (@1MHz)	**2.9**	3.3	2.6

Table 1.3.1 Comparison table of biocompatible polymers on physical properties

reported, provided with their reliability demonstrations and long-term evaluations [59-61]. In addition, LCP is compatible with various conventional manufacturing processes, from UV laser machining to the microfabrication processes of photolithography, metal deposition and wet/dry etching in a wafer unit. The glass-transition temperature and melting temperature are relatively low, 150 °C– 335 °C, therefore multi-layered device can be easily fabricated through a lamination procedure. Also, Young's modulus of LCP complies with other flexible polymers such as polyimide or parylene-C and the rigidity of the device can be easily controlled by varying its thickness [62, 63] . Finally, LCP has good high frequency properties, the relative permittivity of 2.9 and the tangent loss of 0.0022 at 25 GHz [64]. Table 1.3.1 provides the comparison between LCP and the other polymers.

1.3.2. Magnetic Cuff System for HNS

The hypoglossal nerve is a twelfth cranial nerve that innervates the genioglossus, an extrinsic muscle of the tongue. In humans and mammals, terminating branches of the hypoglossal nerve are connected to both retractors and protrusors of the tongue [65]. The hyoglossus muscle, the retractor of the tongue, is comprised of between two and five branches which are laterally divided from the hypoglossal nerve, therefore it is harder to distinguish each other [66]. Furthermore, even a single excited branch of the hyoglossus muscle can induce the retract behavior of the tongue [54]. Accordingly, correct placement of the electrode is crucial for success of the therapy [67].

Cuff electrodes have been introduced and researched owing to their

exclusive advantages related to the interfacing of nerves. Conventional cuff electrodes consist of metal sites on an insulating substrate sheet which is flexible enough to wrap a nerve with a form of a cuff. The cuff electrodes have attractive features not found in other types of electrodes, including a low threshold level, a reduced probability of lead failure, and the capability of use regardless of the surrounding muscle length [68].

To take advantage of the cuff electrodes properly, there have been a few trials to close and secure a slit of the split-cylinder cuff. Suturing was one of the closing method found to be useful during installation, as this method closes and secures the cuff electrode by tying the seam and stitching the substrate of the electrode along the nerve [69, 70]. Waxing and sealing with an adhesive such as silicone elastomer was also attempted. After wrapping the cuff electrode around the nerve, a small bead of silicone was applied along the seam for binding. A shape memory alloy was utilized for another closing method. Three sets of an armature consisting of a nickel-titanium wire split ring were positioned on the silicone rubber cuff. The cuff opened at a low temperature and closed at body temperature due to the memory effect of the armatures [71, 72]. A spiral cuff with a self-spiraling characteristic also has been introduced to overcome the drawbacks of the split-cylinder cuff [73-76]. One group reported fabrication of a self-spiraling cuff by bonding together two sheets of silicone rubber with different natural resting lengths, while another group maintained a curled shape of a cuff with heat deformation at 350 □ under a nitrogen atmosphere [70, 75]. These self-spiraling cuff electrodes do not require closing methods because the cuffs curl themselves in a natural state [73,

75, 76].

Unfortunately, none of the introduced closing methods provide both repeated and ensured closing. The methods using waxing, sealing adhesives, shape-memory alloys provide irreversible closing methods, while the self-spiraling and self-closing cuffs are likely to be easily slipped off. The repeated and ensured closing is especially important for the hypoglossal nerve stimulation in terms of finding a correct place to install the cuff, as aforementioned.

Here, we propose magnetic cuff system comprised of a new type of neural cuff electrode, the magnet-embedded neural cuff electrode (MENCE), and a pulse generator that provide stimulation pulses to the electrode. Rare-earth magnets are embedded in the cuff and are fully encapsulated by LCP. The MENCE is both closed and secured by magnetic force, which enables easy installation and removal, repeatedly without any damage to the nerve. A two-channel MENCE is fabricated using microfabrication processes including a photolithography, E-gun evaporation, and wet/dry etch as well as thermal lamination and laser machining. An external pulse generator board is designed and fabricated using an ASIC and a commercial timer IC to create a train of biphasic pulses. The fabricated MENCE is evaluated *in vivo* as well as *in vitro*, to demonstrate its feasibility. In the *in vitro* evaluations, electrochemical impedance spectrum (EIS) and cyclic voltammetry (CV) are measured in the PBS solution. After the *in vitro* evaluations, the MENCE is installed on the hypoglossal nerve of a rabbit to demonstrate its feasibility as a stimulation cuff electrode. The installed MENCE is connected to the fabricated external pulse generator and current stimuli were delivered to the electrode. During

the stimulation, response of the tongue is observed with bare eyes and the upper airway is recorded via a C-arm fluoroscopy. Finally, discussions are addressed regarding safety, magnetic forces, cost, and extension to multi channels.

1.3.3. Palatal Implant System for SPS

An effect of soft palate stimulation was partly demonstrated on ceasing snoring in the prior arts [56, 57]. To clearly demonstrate the effect of the electrical stimulation on the soft palate, a pilot study is conducted by applying stimuli to the soft palate of the rabbit with an observation of the upper airway through a C-arm fluoroscopy.

Based on the result of the pilot study, a palatal implant system is developed. The system consists of two main parts, an implant that electrically stimulates the soft palate, and an intra-oral device (IOD) that transmits power and data to the implant. There is an auxiliary device called a wireless controller, which provides a user-interface to send stimulation parameters setting to the IOD via ZigBee. The implant is fabricated by laminating multiple LCP layers comprised of coil, electrode, circuit, and adhesion layers. The IOD includes a rechargeable battery, ZigBee receiver, amplifier, and transmitting coil antenna, all of which are integrated and pack aged by a silicone elastomer. The inductive link is evaluated in terms of power transmission and data reliability on telemetry distances varying 2−8 mm. Further assessments are conducted *in vitro* to evaluate feasibilities of the electrode. Electrochemical impedance spectroscopy (EIS), cyclic voltammetry (CV), and voltage transient measurements are performed by a three-electrode cell

in a PBS solution. Then the system is applied to a rabbit and response of the soft palate is observed through a C-ram fluoroscopy. Finally, several discussions including reliability, genioglossus coupling, and possible developments, are addressed.

\

1.4. Objectives of this Dissertation

A goal of this study is to develop neural prostheses for OSA treatment. As OSA involves either retrolingual or retropalatal collapse, two implantable electronics are devised and developed for each purpose (Table 1.4.1).

First, a magnetic cuff system is developed for hypoglossal nerve stimulation. The hypoglossal nerve stimulation is an effective tool for retrolingual opening, but it requires iterative trials for finding correct installation place. The developed cuff electrode can play a role in that it provides an easy, repetitive installation and removal using magnetic forces.

For retropalatal opening, a palatal implant system is firstly proposed. Despite the development of the hypoglossal nerve stimulation, some patients still suffer from retropalatal collapse. The problem can be solved by contracting the soft palate with electric stimuli. The system can help palate-related patients who cannot benefit from the conventional therapies.

Goal	Design	Fabrication	Evaluation
Development of magnetic cuff system for **retrolingual** opening	– For hypoglossal nerve stimulation – Repeatedly installable cuff electrode using magnetic force	– Photolithography, E-gun evaporation, dry/wet etching – UV Laser machining – Thermal lamination	– Electro-impedance spectroscopy – Cyclic Voltammetry – *In Vivo* Stimulation
Development of palatal implant system for **retropalatal** opening	– For soft palate stimulation – Palatal implant with intra-oral device	– Fabrications above – Component mounting – PCB design and fabrication – Encapsulation using silicone elastomer	– Telemetry Reliability – Electro-impedance spectroscopy – Cyclic Voltammetry – Voltage Transient – *In Vivo* Stimulation

Table 1.4.1 Objectives and brief descriptions of this dissertation.

Chapter 2

Methods

2.1 Magnetic Cuff System for HNS

2.1.1. Overview

The proposed system consists of a cuff electrode which provides a novel closing method using magnetic force, and an external pulse generator which generates a train of pulses and delivers it to the electrode. The magnet-embedded nerve cuff electrode (MENCE) has a pair of rare-earth magnets for repeated opening and closing of the cuff. There are a pulse generator ASIC and a timer IC to stimulate the hypoglossal nerve for a second and rest for four seconds.

2.1.2. Magnet-Embedded Nerve Cuff Electrode

2.1.2.1. Electrode Design

Figure 2.1.1 illustrates an overview of a magnet embedded nerve cuff electrode (MENCE). The MENCE consists of three parts: the LCP substrate, gold metal sites, and two samarium-cobalt (Sm-Co) magnets. The magnets are near-hermetically enclosed by LCP substrates for implantation. The 50 μm-thickness gives MENCE flexibility, so that the MENCE can wrap the nerve. The two connector pads are designed to fit a commercial flat flexible cable (FFC) while the other sides of the FFC are connected to the external pulse generator.

2.1.2.2. Fabrication

A brief sequence of the LCP microfabrication process is illustrated in

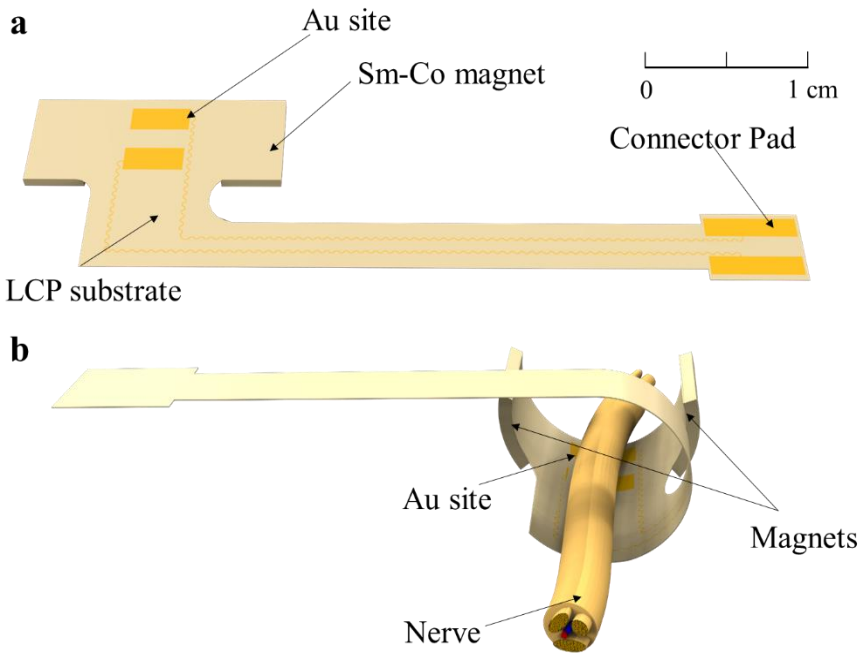

Figure 2.1.1 Overview of MENCE: **a,** LCP based MENCE in the natural state **b,** curled MENCE about to be installed on a nerve.

Figure 2.1.2. First, silicone elastomer (MED-6233, Nusil Technology, USA) was spin-coated to attach a bottom layer LCP film with a high melting temperature (HT-LCP; 330 °C, Vecstar CT-Z series, Kuraray, Japan) and was then cured at 100 °C for eight hours. After attaching the bottom layer LCP film, the wafer was cleansed with acetone, methanol, and isopropyl alcohol in sequence for one minute, in each case. The surface of the LCP film was exposed by oxygen plasma (150 W, 100 sccm, 3 min; Plasmalab 80 plus, Oxford Instruments, U.K.) before the metal deposition step for better adhesion. An adhesion layer of 50 nm of Ti and a seed layer of 100 nm of Au were deposited on the LCP with an e-gun evaporator (ZZS550-2/D, Maestech). A photoresist (AZ 4620; Clariant, USA) was patterned onto the Au seed layer with a MA6/BA6 aligner (vacuum contact, 70 sec; SUSS MicroTec, Germany)

after the spin coating process of 40 sec at 2000 rpm in order to achieve a thickness of 10 μm. Subsequently, Au electroplating was conducted until a layer thickness of 5 μm was created on the non-patterned area of the seed layer. After removing the photoresist using AZ 700 MIF, aqua regia was used for etching Au seed layer, followed by Ti adhesion layer etching using diluted hydrofluoric acid in a wet station. Surface activation and cleaning were conducted through oxygen plasma (150 W, 100 sccm, 3 min) before a lamination process. Meanwhile, an LCP cover layer film with a low melting temperature (LT-LCP; 280 °C, Vecstar CT-F series, Kuraray, Japan) was prepared. The two LCP films, the bottom layer and the cover layer, were aligned in an aluminum jig and laminated in a heating press (30 min, 285 °C, 4.21 kgf/cm^2; model 4330, Carver, USA). After the lamination step, the

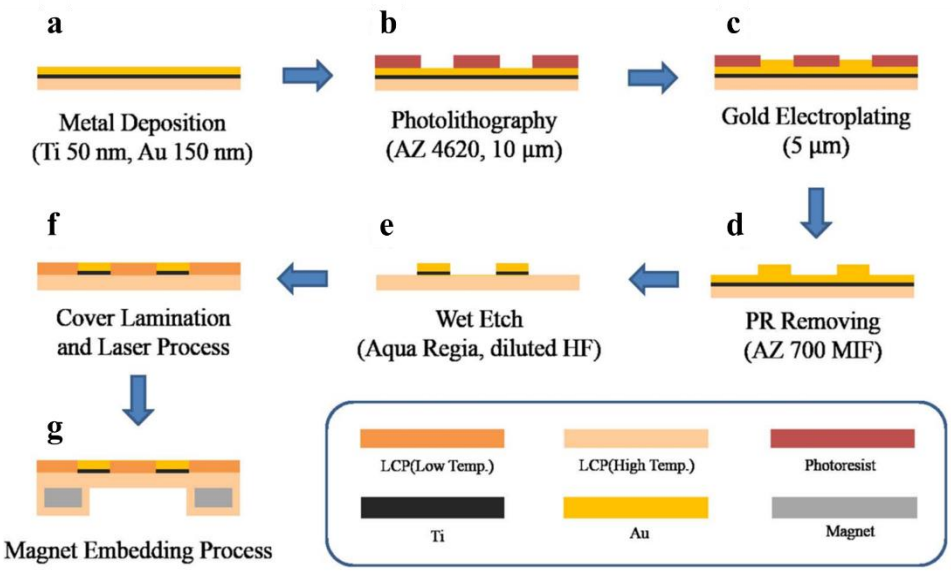

Figure 2.1.2 MENCE fabrication process: **a,** deposition of a 100 nm Au seed layer on a 500 nm Ti adhesion layer, **b,** 10 μm photoresist patterning, **c,** 5 μm gold plating, **d,** photoresist removal, **e,** wet etching of Au seed layer (aqua regia; HCl:HNO_3=3:1) and Ti wet etching (diluted HF), **f,** LCP cover lamination and laser process, and **g,** magnet embedding process.

metal site areas were ablated with a laser machine (355 nm UV, Samurai system, DPSS, USA). Finally, the electrode was cut along a boundary, yielding seven electrodes per wafer.

A pair of magnets were prepared for embedding magnets. Samarium-Cobalt magnets were selected due to their high magnetic flux density and thermal stability. Because the magnet-embedding process takes place at a high temperature process at 285 °C, the magnets should retain their characteristics even after the process is carried out. Regarding the magnetic properties, the surface magnetic flux density, the residual flux density, the coercivity, and the intrinsic coercivity of the magnet were 0.140 T, 1.06 T, 0.791MA/m, and 2.08MA/m in each case.

A 100 μm-thick HT-LCP film, a 25 μm-thick LT-LCP film and the fabricated LCP electrode were activated by the oxygen plasma (150 W, 100 sccm,

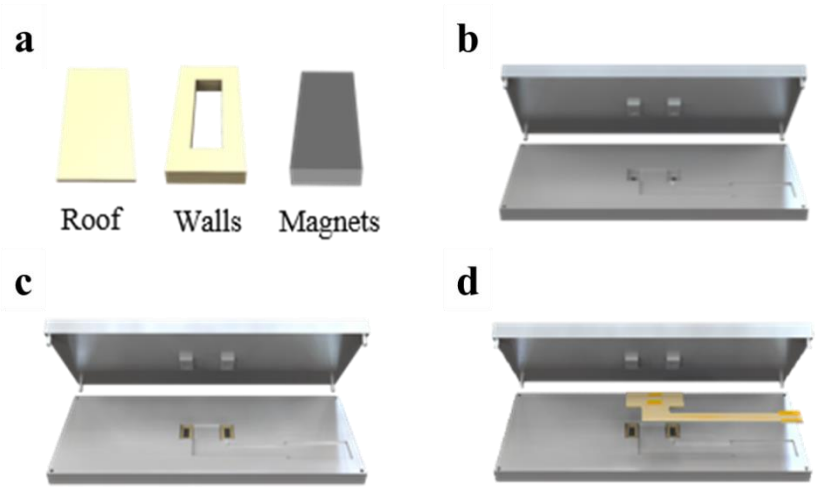

Figure 2.1.3 Magnet-embedding process: **a,** LCP fragments which are supposed to be roofs and walls for encapsulation as well as magnets were prepared. **b,** An aluminum jig was carefully designed to exert pressure onto only the walls in order to prevent the breakage of the magnets. **c,** All components were assembled in the jig. **d,** Finally, an LCP electrode was joined and laminated.

3 min). Later, the HT-LCP film and LT-LCP film were cut into small pieces in the shape of a rectangular donut and a rectangle, to serve as walls and roofs for the embedding of the magnet. The LT-LCP pieces were used as adhesives to glue HT-LCP films, as only the LT-LCP films melt at 285 °C. The electrode and the small pieces were put together into a small aluminum jig and laminated by a heating press (30 min, 285 °C 15.65 kgf/cm^2). The overall magnet-embedding process is depicted in Figure 2.1.3 for a better understanding of the described process.

2.1.3. External Pulse Generator

2.1.3.1. Circuit Description

A schematic design of the pulse generator is shown in Figure 2.1.4. An ASIC (Samsung CMOS 0.18 μm) in the reference was used for generating a biphasic current pulse. As the ASIC inputs parallel bits of parameters, amplitude, duration, and pulse rate, mechanical switches were used for setting the parameters. A commercial timer IC (LM555CM, Texas Instruments, U.S.) was used to control durations of 'ON' and 'OFF' states of the stimulation, one second and four seconds, respectively.

2.1.3.2. Fabrication

The pulse generator was fabricated on a printed circuit board having a dimension of 100 mm x 50 mm including a battery holder of 50 mm x 50 mm. The ASIC was wire-bonded on the board while all other components were soldered.

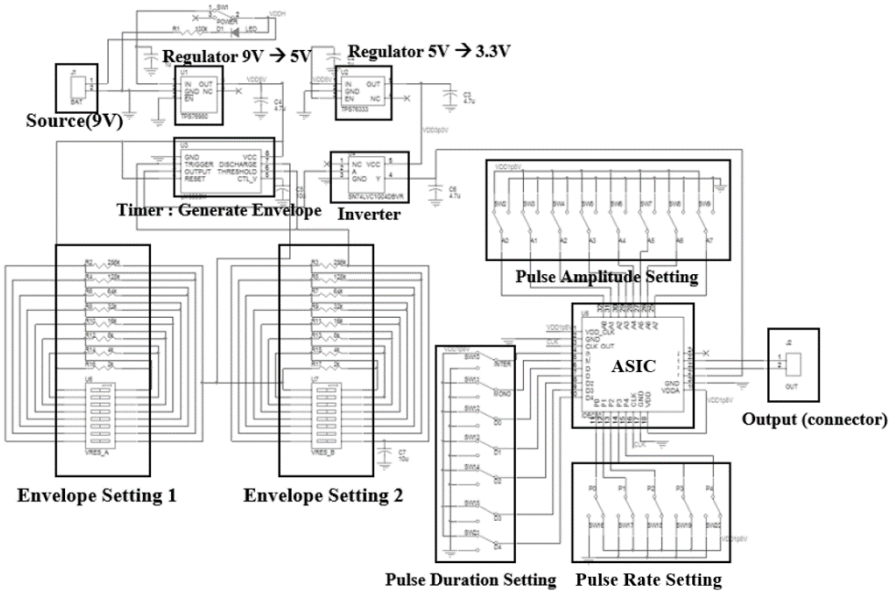

Figure 2.1.4 Schematic design of the external pulse generator consisting of ASIC chip and its peripheral circuits to control timings.

Two male connectors were connected to the outputs of the ASIC via DC-blocking capacitors which was used for safety of the stimulation.

2.1.4. Evaluations

2.1.4.1. Electrochemical Measurements *In Vitro*

The electrochemical impedance spectrums (EISs) and cyclic voltammetries (CVs) were measured (n = 10) with the Solatron 1260 and 1287 systems (Solatron, U.K.) in a three-electrode cell using an Ag|AgCl reference electrode and a mesh-type Pt counter electrode in PBS solution (Gibco, Thermo Fisher Scientific, U.S). The EIS was measured for frequencies from 0.1 Hz to 10 kHz by applying a sinusoidal of 10 mV amplitude without an offset. The CV curve was recorded in the range of -0.6 – 0.8 V at a scan rate of 1 mV/s at which the CVs

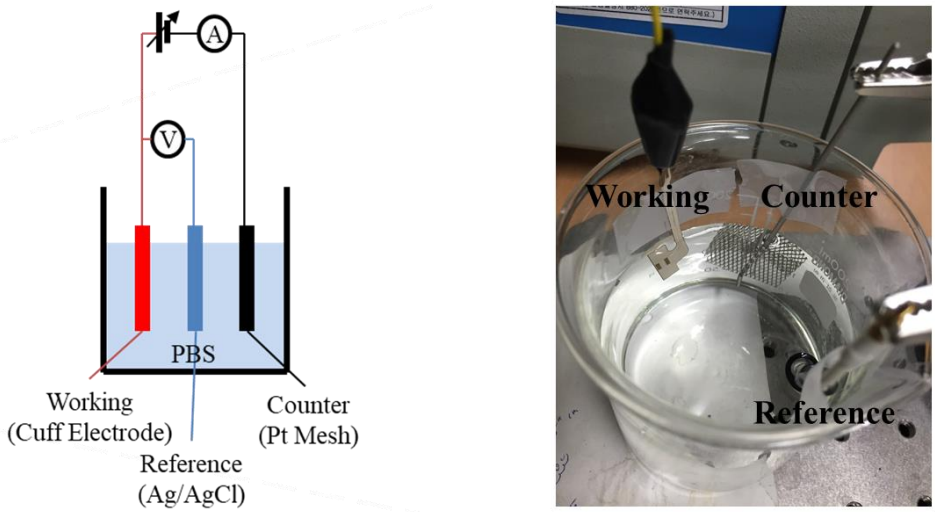

Figure 2.1.5 Illustration (left) and picture (right) of *in vitro* electrochemical measurement setup of magnetic cuff using three-electrode cell.

of the electrodes could be measured in the steady state [77]. The cathodic charge storage capacity (CSC_c) was calculated by integrating the cathodic area of the CV curve using the CorrView software package. The setup of the *in vitro* evaluation is depicted in Figure 2.1.5.

2.1.4.2. Animal Testing *In Vivo*

All the following experimental procedures were approved by the International Animal Care and Use Committee in Seoul National University Bundang Hospital. Seven-month-old New Zealand White male rabbits weighing 2.1 to 2.6 kg were used in this study. All the rabbits were acclimated in the new environment for the first week and used for further experiments. Sedation was induced by intramuscular injection of 0.3 mL/kg of Zoletil (tiletamine hydrochloride plus zolazepam hydrochloride; Virbac) and 0.25mL/kg of Rompun

(xylazine; Bayer AG) at the same time. After sleep was induced, a midline neck incision around hyoid bone was made. The main trunk of the hypoglossal nerve was identified at the lateral side of the hypoglossus muscle over the external carotid artery. The nerve was dissected to place the stimulation cuff electrode. Then the MENCE was installed on the hypoglossal nerve of the rabbit. The electrode was percutaneously connected to a pulse generator with a mounted ASIC chip (Samsung 0.18 μm CMOS), which supports various amplitudes, duty cycles, frequencies and pulse rates of the output current. The output current was conducted in a train-of-pulse series lasting for 1.15 sec with a rest of 3.93 sec. The pulse amplitude, rate, and duration were 0.106 mA, 0.635 kHz and 0.375 ms, respectively. The upper airways of the subjects were observed with C-arm fluoroscopy (Philips, Netherlands) during the stimulation. The experimental setup is depicted in Figure 2.1.6.

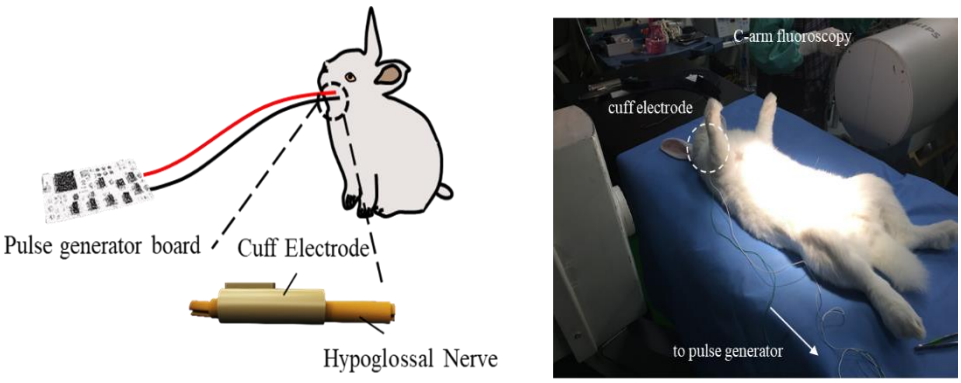

Figure 2.1.6 Illustration of the *in vivo* experimental setup (left) and its picture (right). Installed cuff was percutaneously connected to pulse generator board and behavior of upper airway was recorded via C-arm fluoroscopy.

2.2 Palatal Implant System for SPS

2.2.1. Pilot Study *In Vivo*

A pair of a stimulation electrode and a reference electrode were prepared for the experiment (needle-type, 20 degrees, A-M Systems Inc., U.S.). Each electrode was made of stainless steel with a diameter of 0.254 mm and exposed at the end of the tip by 3 mm. A custom-made pulse generator was used for the stimulation. A stimulator ASIC was surface-mounted on the PCB of the pulse generator with parameter-controlling interfaces [78].

A seven-month-old New Zealand white male rabbit was prepared for the experiment. The rabbit was acclimated to the new environment for the first week. Sedation was induced by intramuscular injection of 0.3 ml/kg of Zoletil (tiletamine hydrochloride, zolazepam hydrochloride; Virbac) and 0.25 ml/kg of Rompun (xylazine; Bayer AG) at the same time. After sleep was induced, the prepared needle-type electrodes were inserted into the soft palate of the rabbit. Then, current

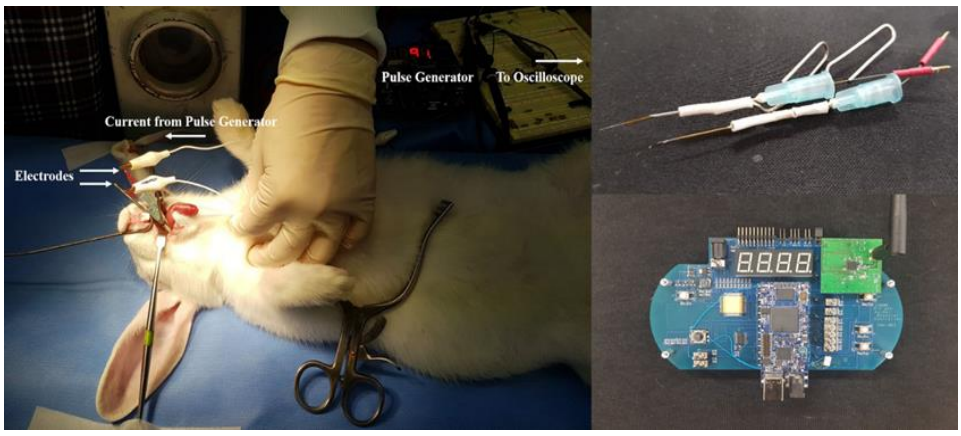

Figure 2.2.1 *In vivo* test setup of the pilot study (left) using commercial electrodes (right-top) and custom-made pulse generator (right-bottom).

was provided from the pulse generator through the connected cable. Frequencies were swept from 20 Hz to 200 Hz while maintaining a voltage level at 9 V, and duration at 636.3 μs. Next, the threshold level was evaluated by decreasing the current level. Simultaneously, the upper airway of the rabbit was observed with C-arm fluoroscopy (Philips, Netherlands). The setup and tools for the *in vivo* test are arranged in Figure 2.2.1.

A mock-up insertion test of the implant was also performed. First, high-temperature (HT-LCP; 330 °C, Vecstar CT-Z series, Kuraray, Japan) and low-temperature (LT-LCP; 280 °C, Vecstar CT-F series, Kuraray, Japan) LCP films with 100 μm-thickness were prepared. Then the LCP films were cut into the desired shape using a laser machine (355 nm UV; Samurai system, DPSS, U.S.) and cleansed with acetone, methanol, and isopropyl alcohol in sequence each for a

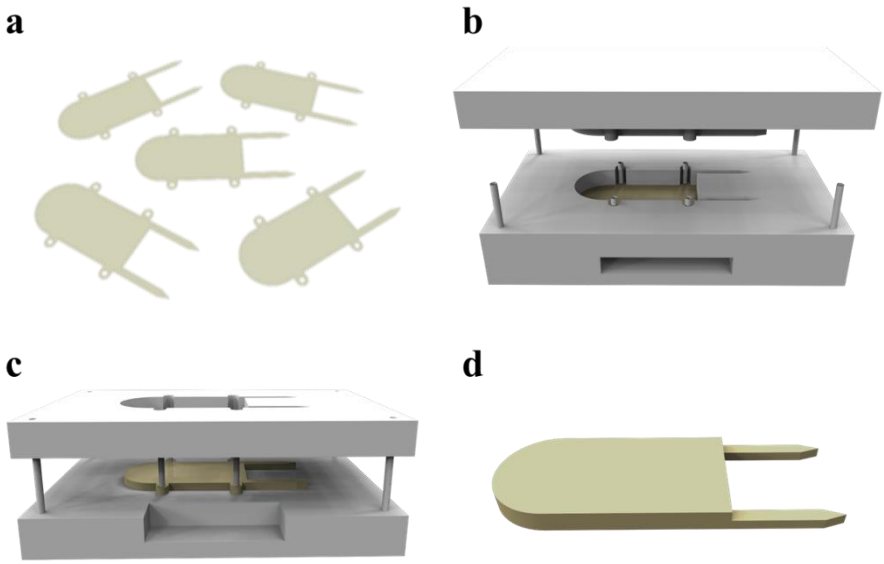

Figure 2.2.2 Fabrication process of palatal implant: **a,** preparation of LCP pieces, **b,** lamination, **c,** lift-up of the jig sidewall, and **d,** completion of the fabrication with laser-machining.

minute each. Next, the LCP pieces were exposed to oxygen plasma (150 W, 100 sccm, 3 min; Plasmalab 80 plus, Oxford Instruments, U.K. Subsequently, the HT-LCP and the LT-LCP pieces were stacked into a custom-designed aluminum jig in turn and laminated by a heating press (30 min, 285 °C, 3 MPa). The aluminum jig was designed to have a 3-layer structure to easily remove the laminated mock-up after the process. The jig was coated with teflon of 0.1 mm thickness to prevent the LCP from sticking to itself after the process. The fabricated mock-up was then autoclaved at 121 °C for 20 min before implantation (Unisteri, BMT Medical Technology, CZE). The fabrication process of the PI mock-up is illustrated in Figure 2.2.2.

A New Zealand white rabbit was prepared and induced to the sleep following the same procedure stated above. An incision was made along the lateral axis of the hard palate, to obtain enough space for the mock-up to be implanted. Then the mock-up was inserted toward the soft palate along the incised space. After the insertion, the wound was closed by suturing. Antibiotics with 50 mg/ml (enrofloxacin; Bayer AG) were injected to the subject every day after the surgery to prevent further inflammations. All the experimental procedures were approved by the International Animal Care and Use Committee in Seoul National University Bundang Hospital.

2.2.2. Overview

Figure 2.2.3 illustrates an overview of the palatal implant system. The system consists of two major parts: the implant and the intra-oral device (IOD). The implant has a multi-layered structure consists of a coil, electrodes, and a circuit. Two electrodes exist on each shank upward and downward to generate a bipolar current around the tip. The implant receives power and data via an inductive link from the IOD through the hard palate skin and deliver generated current stimulation pulses to the electrode interfacing the soft palate.

The IOD is a device in the shape of an oral appliance which can be

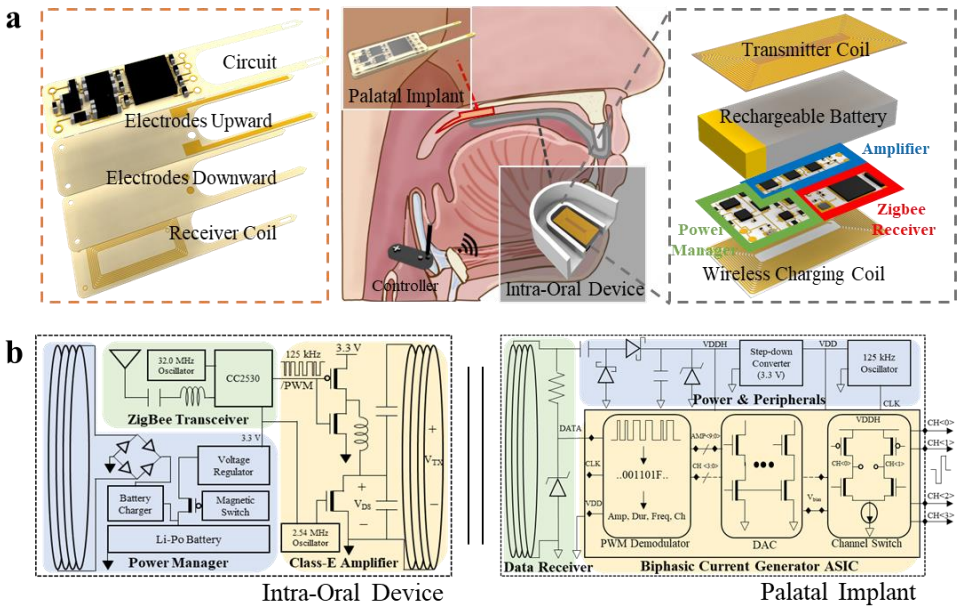

Figure 2.2.3 Overview of the proposed palatal implant system. **a,** Overview of the palatal implant system. The palatal implant has a pair of electrodes at the end of each shank to stimulate the soft palate. The intra-oral device, designed to be equipped in the oral cavity, transmits RF signals to the implant to operate it. The detailed structure of each device is illustrated at the left and the right. **b,** Circuit diagrams of the system. The intra-oral device modulates and amplifies a data signal received via ZigBee. Then the implant utilizes the received signal as both power and data to operate the ASIC that supplies biphasic current pulses to the electrodes.

equipped in the mouth. It contains a transmitter coil, PCB, battery, and wireless charging coil, all of which are fully packaged by silicone elastomer elastomer (MED-6233, NuSil Technology Inc., U.S.). In the circuit, there is a commercial ZigBee transceiver IC (CC2530, Texas Instrument, U.S.) which receives a command signal transmitted from the controller. The received command signal is then modulated and amplified by the class-E amplifier, and delivered to the implant via an inductive link. The circuit in the IOD is fully-powered by the embedded rechargeable battery of 1.11 Wh capacity.

An auxiliary device, the wireless controller, is a portable device that provides a user-interface for setting stimulation parameters such as duration, frequency, and amplitude. The determined parameter, which serves as a command signal to the ASIC in the implant, is transmitted to the IOD via ZigBee.

2.2.3. Palatal Implant

2.2.3.1. Circuit Description

The circuit of the implant consists of an RF receiver that receives a modulated signal and a stimulation current pulse generator ASIC with its peripheral components. First, the RF receiver is comprised of a planar coil and a capacitor constructing a parallel resonance whose impedance becomes maximum at the resonance frequency. From the Ampere's circuital law, the induced current density of the coil has a relationship with a magnetic flux intensity H as follows.

$$\nabla \times H = J \tag{2.1}$$

Equation (2.1) implies that the magnetic field created by a transmitter coil induces a current on the receiver coil via an inductive link. Therefore, a high voltage level, which is necessary for obtaining enough compliance voltage for the stimulation output, can be achieved by the parallel resonator that maximizes its impedance. To achieve the parallel resonance, the inductance of the receiver coil at the carrier frequency of 2.54 MHz measured using a network analyzer (MS4630B, Anritsu, Japan). Then the capacitor value was selected to construct the resonance at the frequency as follows,

$$C = 1/(w^2 L_R) \tag{2.2}$$

where L_R is the inductance of the receiver coil and w is the angular frequency. The LC resonance can be affected by either a load attached to the resonator or a mutual inductance of the inductive link. However, as a Q-factor of the receiver coil is normally small in implantable devices, the efficiency does not vary large due to the reciprocal relationship between Q and the bandwidth. The received signal is divided into two pathways, the power and the path. In the power path, the signal passes through a voltage clamper consisting of a capacitor and a Schottky diode. The voltage clamper places the bottom peak of the voltage to the reference level, literally 'clamping' the voltage to the reference. The highest peak voltage of the voltage becomes approximately twice, specifically $2V_p - V_f$, where V_p is the peak voltage and V_f is the forward bias of the diode. The clamped voltage is then rectified by the half-wave rectifier, creating VDDH the compliance level of the stimulation output. As the voltage is clamped to positive, there is little power loss except the dissipated power of the diode. A Zener diode with the Zener-voltage of 20 V is

placed additionally to the rectifier for a safety, so as not to exceed the maximum acceptance voltage level of the ASIC. VDDH is further fed to a step-down converter (NCP715, ON Semiconductor, U.S.). The step-down converter can receive the input voltage up to 20 V and output VDD the constant voltage level of 3.3 V. The generated VDD is supplied to both the ASIC and the oscillator (LTC6906, Analog Devices, U.S.). The oscillator is programmed by a resistor to input a 2.54 MHz pulse rate. Additional bypass capacitor is parallelly added to the resistor to remove an AC interference caused by a magnetic field of the receiver coil. The output pulse is used as a clock of the digital part of the ASIC. On the other hand, a simple voltage clipper is implemented in the data path. The signal is clipped by the Zener diode to limit the voltage level of DATA to VDD to be fed into the digital part of the ASIC. The value of the resistor in the clipper should be carefully selected. If the resistance becomes too small, the voltage across the resonator decreases as the decreased

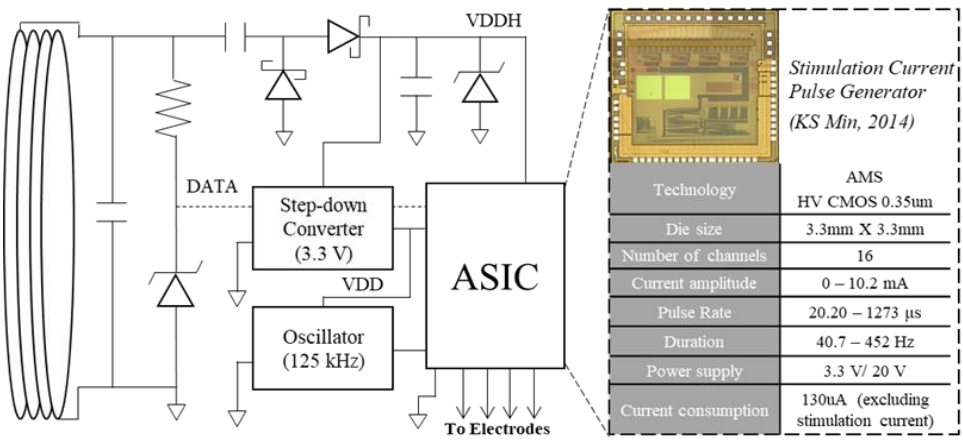

Figure 2.2.4 Circuit diagram of the palatal implant. The RF receiver comprised of LC parallel resonance gains high levels of the voltage. The receiver rectifies and clips to use the signal as power and data for current generator ASIC. The ASIC is capable of generate biphasic current pulses with variable amplitude, pulse rate, and duration, as arranged in the rightmost table.

resistance determines the equivalent load of the circuit. If the resistance becomes too large, the clipped voltage may decrease under the threshold of the ASIC. The resistance value is selected to 1 kΩ, experimentally.

The ASIC inputs VDDH, VDD, and DATA to generate a biphasic stimulation current pulse. The ASIC extracts frequency, duration, and level information of the output pulse from DATA. According to the information, the ASIC generates the output pulse having a compliance level of VDDH.

2.2.3.2. Fabrication

2.2.3.2.1. Electrode Layers

The electrode layers were fabricated on 50 μm-thick LCP substrates using the fabrication process of the magnet embedded nerve cuff electrode, as previously described in 2.1.2.2. Each layer had two 0.5 mm-width lead lines depart from a rectangular pad which was connected to the circuit layer through a via. Figure 2.2.5

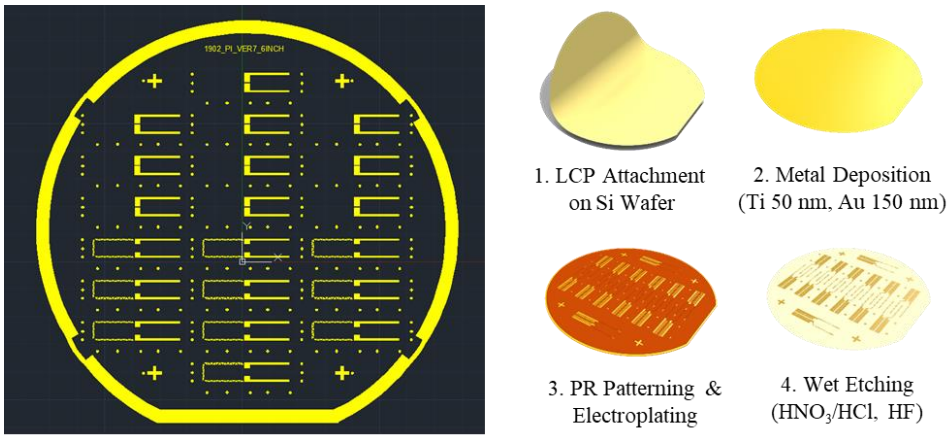

Figure 2.2.5 Photolithography mask of the electrode layer (left) and brief illustrations of the fabrication process of the palatal implant.

depicts a design of the photolithography mask used for the fabrication (left) and brief illustrations of the fabrication method (right).

2.2.3.2.2. Antenna Coil and Circuit Layers

A planar coil was drawn having a pitch and a width of 100 μm in a 13 mm x 6.5 mm rectangle with twenty turns. Both ends of the coil were connected to pads which have a diameter of 1.0 mm with 0.2 mm drill. Two additional pads were patterned on the right side of the coil as stoppers in the laser process which will be described later.

The circuit described in 2.2.3.1, was drawn in a layout reflecting all physical dimensions including pads and packages. The commercial chip packages and passive components were carefully selected to minimize their foot prints on the limited board size. The circuit had six via pads, two for connecting the coil and four for connecting the electrodes. The design of the antenna coil and the circuit are shown in Figure 2.2.6 (left).

A conventional PCB fabrication process was used to fabricate an antenna

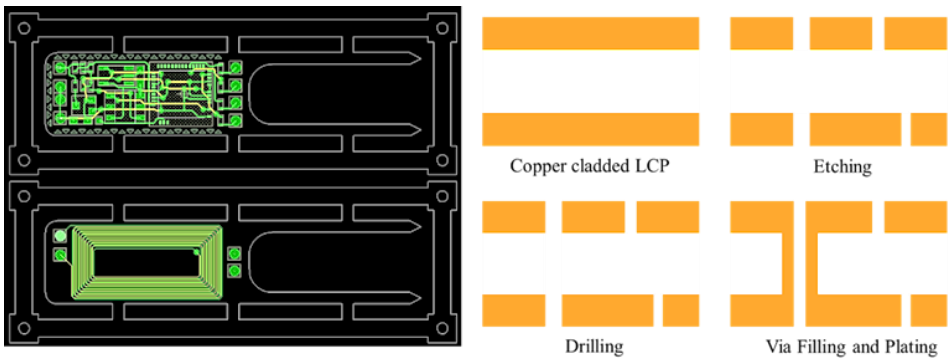

Figure 2.2.6 Layouts of circuit and coil layers of the palatal implant (left) and its fabrication methods (right).

coil layer and a circuit layer. A double-sided, copper cladded LCP sheet was prepared (Ultralam 3850, Rogers Corporation, U.S.). On the 50 μm-thick LCP substrate, a 17.8 μm-thick copper sheet was cladded on each side. The metals on the both sides were etched and patterned using a mask. Then vias were drilled by a UV laser and filled with coppers. Finally, additional 17.8 μm-thick Au was plated on the copper. The fabrication process is depicted in Figure 2.2.6 (right).

2.2.3.2.3. Multi-layer Lamination

The implant was fabricated by laminating multiple LCP layers including a coil, a circuit, electrodes, and insulation layers (Figure 2.2.7**a**). As the laminating temperature is between the melting temperatures of the CT-Z and CT-F, CT-F layers served as adhesives bonding the CT-Z layers each other. Therefore, it is desirable

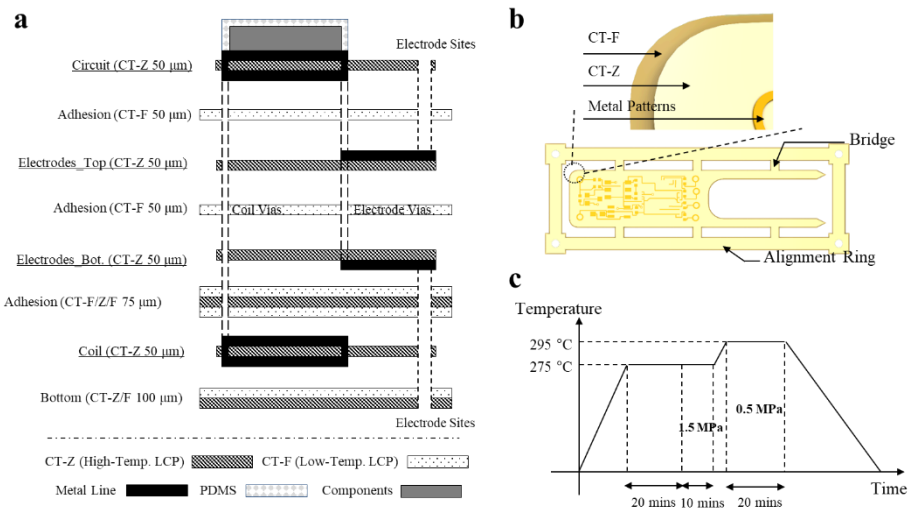

Figure 2.2.7 a, Lamination profile of the palatal implant fabrication. Multiple LCP sheets including functional layers as well as adhesion layers were aligned and laminated. **b,** High temperature (CT-Z) and low temperature (CT-F) LCPs were stacked in turn. **c,** Plot of temperature and pressure condition for the lamination.

to pattern metals on the CT-Z layers to avoid migration of lines during the lamination process, not on CT-F. CT-F and CT-Z layers were stacked in turn, but the size of the CT-F layers was designed to 100 μm from the border of the CT-Z layers (Figure 2.2.7**b**). This is to cover the inter-layer junctions with CT-F, utilizing its melting property on the operation temperature of 290 °C. The detailed layer configurations of the package are described as follows. First, an insulation layer of 100 μm was placed at the bottom. Then a coil layer and adhesion layers were loaded in order. Between the bottom electrode layer and the coil layer, there was a buffer layer comprised of one CT-Z layer surrounded by two CT-F layers. The role of the buffer layer was to prevent migration of patterns on the electrode layer, which receives a sheer stress from the patterns on the coil layer. The electrode layer was then placed on the adhesion layer with patterns downward. Another electrode layer was placed on the adhesion layer upward, and finally a circuit layer was placed at the top.

After stacking all the layers, heat and pressure were applied to the layers to fabricate in to one body. The lamination condition of pressure and temperature was plotted in Figure 2.2.7**c**. First, the temperature was increased from the room temperature without pressure. When the temperature reached 275 °C, the sample remained untreated for 20 mins to make sure that the sample reached the temperature. Then a pressure of 1.5 MPa was applied to the sample for 10 mins. As both CT-F and CT-Z were crystalized in the temperature, they bond together when the pressure was applied. The temperature was further increased to 295 °C where CT-F totally melts. The pressure of 0.5 MPa iwass applied to the sample for filling

spaces between the layers for 20 mins. Finally, the sample was cooled down slowly in the room temperature.

The Figure 2.2.8 illustrates an aluminum lamination jig for the lamination. The jig was coated by teflon to prevent adherence of the LCP to the aluminum after the lamination. The jig consisted of three parts; the bottom part for loading the LCP layers, the middle part for limiting spread of the melted CT-F, and the top part for applying a force to the LCP sample. First, the LCP samples were loaded to the bottom part of the jig. In the bottom part, there were four stainless-steel poles to fix the position. After the LCP samples are loaded into the jig, the middle part was joined to the bottom part with screws. If the parts are not screwed, melted CT-F may flow through the small gap between the parts. Finally, the top part was assembled to the middle-bottom part along the assembly poles. Ceramic sponges covered by aluminum foils were placed on the top and under the bottom part to apply the force evenly to the sample during the lamination.

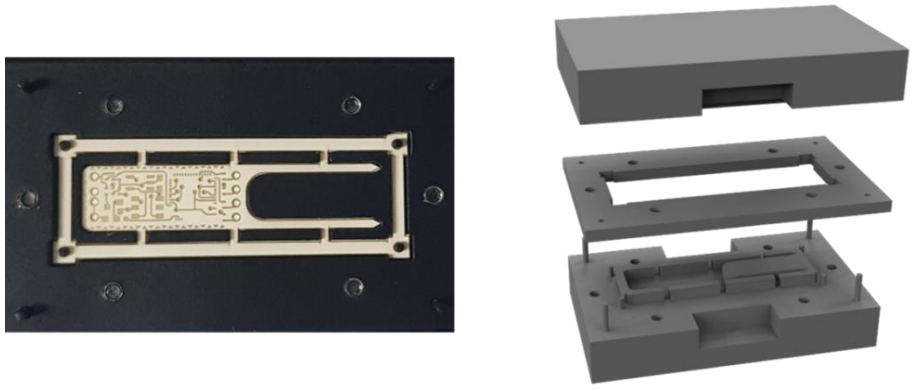

Figure 2.2.8 LCP sheets aligned and stacked into the jig (left) and illustrated parts of the jig (right).

2.2.3.2.4. Post-lamination Process

After the lamination was completed, vias were created to connect layers each other. A laser machine (355 nm UV, Samurai system, DPSS, USA) was used for the via creation parameters having laser power of 400 mW, mark speed of 500 mm/s, frequency of 20 kHz, and pulse width of 20 μs. Holes with a diameter of 700 μm were drilled from the circuit to the coil layer and to the electrode layers until the pads were visible through a microscope. Lines with 180 μm-spacing were drawn using a CAD program (AutoCAD, Autodesk, U.S.) to generate the ablation pattern. The electrode sites were also opened using the parameters stated above. A rectangular area of 2 mm x 0.5 mm was ablated for each electrode site. After the laser ablation process was done, the sample was cleaned using oxygen plasma (150 W, 100 sccm, 3 min; Plasmalab 80 plus, Oxford Instruments, U.K.). Then Iridium oxide was electroplated from an aqueous solution of 4 mM $IrCl_4$ in a supporting electrolyte of 40 mM oxalic acid and 340 mM K_2CO_3, obeying the method our group previously published [79]. Fifty instances of triangular waveforms ranging 0− 0.55 V (vs. Ag/AgCl reference) at a 50 mV/s sweep rate were followed by 1800 rectangular pulses at 0.55 V (1 Hz frequency, 0.5s duration).

The constructed vias were filled with silver epoxy (H20E, Epoxy Technology, Inc., U.S.) to electrically connect the layers. Thereby, layers of coil-circuit-electrode could be electrically connected through the filled vias. Then the silver epoxy was cured for 12 hours at 50 °C. After the curing was done, measurements on resistance and inductance were conducted to ensure status of the sample. Electronic components having minimized footprints were selected to

reduce layout dimension of the sample. The components were soldered with the soldering temperature of 300 °C where high-temperature LCP (CT-Z) substrate does not melt. Finally, the package was encapsulated by silicone elastomer (MED-6233, NuSil Technology Inc. U.S.) except the electrode shanks. Two parts of the silicone (MED-6233A, MED-6233B) were mixed with 1:1 ratio using an electric mixer. The mixed silicone was loaded into a centrifuge and then loaded into a vacuum chamber to extract bubbles from it. An aluminum mold was designed and manufactured for the packaging. The silicone elastomer was injected through the feed at the top to fill cavity in the mold. Two air outlets were drilled to emit the airs so that no air was trapped in the elastomer.

2.2.4. Intra-oral Device

2.2.4.1. Circuit Description

In the intra-oral device (IOD), a wireless charging coil, rechargeable battery, and transmitter coil were connected to a printed circuit board (PCB). As the whole parts of the IOD were packaged by silicone elastomer for oral-equipment, wireless charging technique was adopted for the rechargeable Li-Po battery. A command signal, received via ZigBee from the external controller, was ASK modulated and amplified by a class-E amplifier. Then the modulated signal was transmitted to the receiver coil in the palatal implant via an inductive link.

2.2.4.1.1. ZigBee Receiver

A commercial ZigBee compliant RF transceiver chip and antenna was

used for implementing the ZigBee receiver (CC2530, Texas Instrument, USA; 2450AT42A100E, Johanson Technology Inc., USA). The transceiver includes an 8051 CPU core and 256 Kb flash programmable memory. The transceiver was programmed to generate PWM based on the message signal from an external controller. The message signal contained information about parameters of the stimulation current pulse, including duration, frequency, amplitude and output channels of the pulse. Table 2.2.1 shows a protocol of the message signal. There were 'F' bits located at the both ends of the word to inform the ASIC of either the start or the end of the word. Also, 'P' bits were located at the second least significant bit to perform an even parity check. Each word consisted of 18 bits with six modes; four modes for settings and the two for stimulations. The parameters of the stimulation pulse could be set by inputting SET 1− 4 and the stimulation could be started or stopped with STM 1− 2. The array of the words generated by the ZigBee transceiver was fed into the ASK modulator to modulate the message on the carrier

Bits	17	16	15	14	13	12	11	10	9	8	7	6	5	4	3	2	1	0
SET1	F	0	0	0	x	x	R0	R1	R2	R3	R4	R5	x	x	x	x	P	F
SET2	F	0	0	1	I0	I1	D0	D1	D2	D3	D4	D5	x	x	x	x	P	F
SET3	F	0	1	0	C1	C2	A0	A1	A2	A3	A4	A5	A6	A7	A8	A9	P	F
SET4	F	0	1	1	C1	C2	S0	S1	S2	S3	I0	I1	B	ON	x	x	P	F
STM1	F	1	0	0	x	x	x	x	x	x	x	x	x	x	x	x	P	F
STM2	F	1	0	1	x	x	x	x	x	x	x	x	x	x	x	x	P	F

Table 2.2.1 Digital protocol of the pulse generator ASIC. Bit '17' and '0' means the most significant bit (MSB) and the least significant bit (LSB), respectively. Prefix 'R', 'I', 'D', 'C', 'A', 'S' means pulse rate, index, duration, current source, amplitude, and site, respectively. 'F' and 'P' stands for announcing start/end of the frame and parity check.

wave.

2.2.4.1.2. Class-E Amplifier

The class-E amplifier is a popular amplifier class for RF applications owing to its high efficiency, ideally 100 %. The class-E amplifier operates in a switched-mode where the transistor behaves as a switch with rail-to-rail pulse gate drivers. The different thing from other switched mode amplifiers such as a class-D amplifier is that the class-E amplifier utilizes the shunt capacitor, including the parasitic capacitor of *Q*, as a resonant agent. In the other classes, the shunt capacitor in *Q* is considered as a 'bad' component that needs to be removed, as it induces power loss by prohibiting sharp transition between ON and OFF. However, the class-E amplifier overcome the problem by utilizing the shunt capacitor as a resonance agent. The capacitors C_1 and C_2 in Figure 2.2.9 comprise a resonance with L_{Tx} the transmitter coil, while L_{choke} feeds a constant current to *Q*. There are

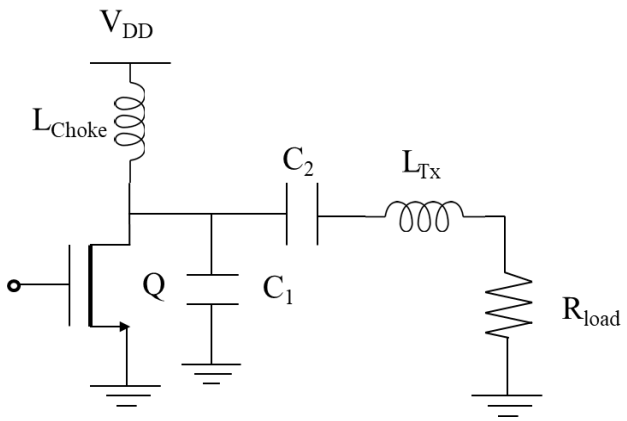

Figure 2.2.9 Schematic of basic class-E amplifier. L_{choke} serve as DC pass and C_1, C_2, L_{TX} comprises a resonance at both ON and OFF state of the transistor *Q*.

two resonance frequencies depending on the state of Q. When Q is ON, C_1 virtually shunt out as the drain and the source of Q is connected through the on-resistance which is normally under few ohms. Therefore, only C_2 and L_{Tx} participate in comprising the on-state resonant frequency:

$$f_{on} = \frac{1}{2\pi C_2 L_{Tx}} \tag{2.3}$$

On the other hand, when Q is OFF, C_1, C_2 and L_{Tx} take part in comprising the off-state resonant frequency as follows,

$$f_{off} = \frac{1}{2\pi (C1 || C_2) L_{Tx}} \tag{2.4}$$

while L_{choke} is assumed to be large enough that AC signals do not pass through. For the current to have a sinusoidal waveform, switching frequency f_{sw} should take

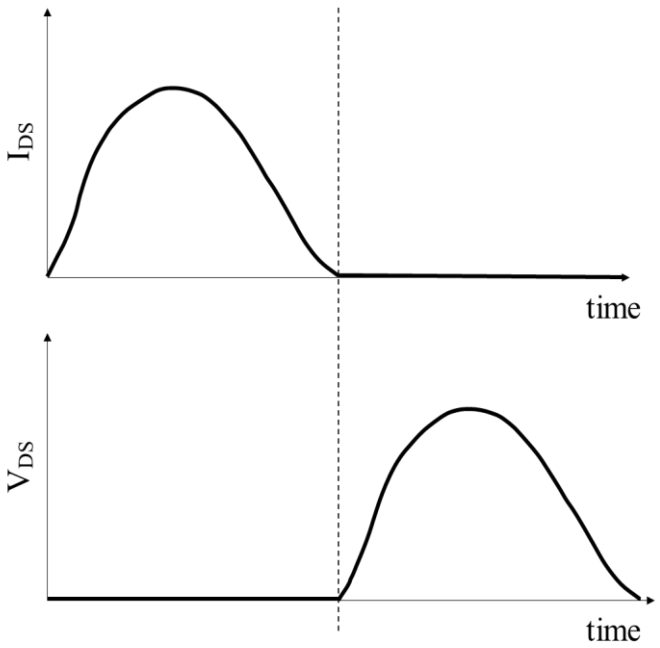

Figure 2.2.10 Current (top) and voltage (bottom) waveforms at the drain-source nodes of Q under zero-voltage switching (ZVS) condition. Designed not to have V_{DS} and I_{DS} at the same time, the class-E amplifier ideally has zero power loss.

place between (2.3) and (2.4), *i.e.*,

$$f_{on} < f_{sw} < f_{off} \tag{2.5}$$

It is desirable for f_{on} and f_{off} to be within 10 % of f_{sw} meeting an arithmetic mean in practice. From the equations (2.3− 2.5), initial values of C_1 and C_2 can be defined.

For the amplifier to be efficient, the switching loss of Q should be minimized. The switching loss usually occur when the transistor starts to switch the state, when both I_D and V_{DS} are likely to be exist at the same time. Thus, it is important to meet a zero-voltage switching (ZVS) condition, as shown in Figure 2.2.10. The key point of ZVS is to delay the rise of I_D until V_{DS} reaches zero and to delay the rise of V_{DS} until I_D reaches zero, allowing both transitions only at $V_{DS} = 0$. Thereby, the power dissipation at the transistor can become ideally zero, neglecting its ON-resistance, R_{on}. The ZVS of the amplifier depends on the value of R_{load} including equivalent series resistances (ESR) of the capacitors, a resistance of L_{Tx}, and a reflected resistance from the counterpart coil. Therefore, further fine adjustment of C_1 and C_2 are further required in addition to the condition (2.5). The detailed tuning method is well described in previous research, providing a guideline to tune C_1 and C_2 according to measured voltage waveforms of the transistor [80]. The tunning procedure is quite tricky though, as both the condition (2.5) and ZVS should be met simultaneously through iterations. It is recommended to use a transistor with low output capacitance, C_{oss}, compared to C_1. As C_{oss} affects to the resonance when the transistor is OFF, it may results in discrepancy between the calculation value and the actual value of the output frequency if the value is too high. However, the transistors with low C_{oss} normally have larger R_{on}, which

dissipates the power in terms of heat in every half period. Therefore, it is important to select an appropriate transistor considering the trade-off.

2.2.4.1.3. ASK Modulation

Amplitude-shift keying (ASK) is a kind of amplitude modulation which represents digital data as amplitude variations of a carrier wave. Strong point of the ASK is simplicity in implementation, requiring only a pair of MOSFETs comprising an inverter added to the power supply. The power supplied to the amplifier was synchronized to the control signal driving the gate, consequently, the envelope of the carrier wave can be modulated by the signal. Though ASK has poor accuracy compared to other modulation methods such as the frequency-shift keying (FSK) and phase-shift keying (PSK), its simplicity gives flexibility and feasibility on designing a low-power and miniaturized circuit.

2.2.4.1.4. Power Management

The intra-oral device (IOD) contained a rechargeable battery in it, as the IOD delivers power to the implant. The whole part of the IOD were encapsulated by silicone elastomer to prevent penetration of saliva. Therefore, power managements including charging and switching the power should be enabled in non-contact methods. Strategies of an inductive link powering and magnetic switching were used for the purpose.

A wireless charger unit based on a class-E amplifier was designed and fabricated to transmit 2.54 MHz-electromagnetic wave to the IOD. A heat sink was

mounted on the ground pad of the board using a silver epoxy (H20E, Epoxy Technology Inc., U.S.) to prevent overheating. A commercial transmitter coil (760308104113, Wurth Electronics Inc., Germany) was used for the transmitter antenna. For higher charging efficiency, the optimal geometric values were selected from the reference [81].

Transmitted electromagnetic was received by the receiver coil (AWCCA-28R15H08-C01-B, Abracon LLC, U.S) in the IOD. The coil was comprised of parallel resonance with a capacitor having the value of $1/(w^2L)$, where w is an angular velocity at 2.54 MHz. The received RF signal was rectified by a full-wave rectifier followed by a Zener diode with Zener voltage of 6 V. The diode was added to avoid an overvoltage to protect a battery charger IC (BQ21040, Texas Instruments Inc., U.S.). The battery charger delivered the rectified power to the lithium polymer battery, thereby the battery could be recharged.

A magnetic switch was implemented to control the power. The switch was comprised of a magnetic sensor and a D flip-flop to behave as a toggle switch. The sensor prints a digitized output after comparing values of the detected magnetic flux and its threshold level. Then the output was fed to the clock pin of the D flip-flop whose output was connected to the input 'D' to implement the toggle behavior. In this principle, the power of the IOD could be switched by a permanent magnet in a non-contact method.

2.2.4.2. Fabrication

The described circuit was fabricated on a printed circuit board and all the

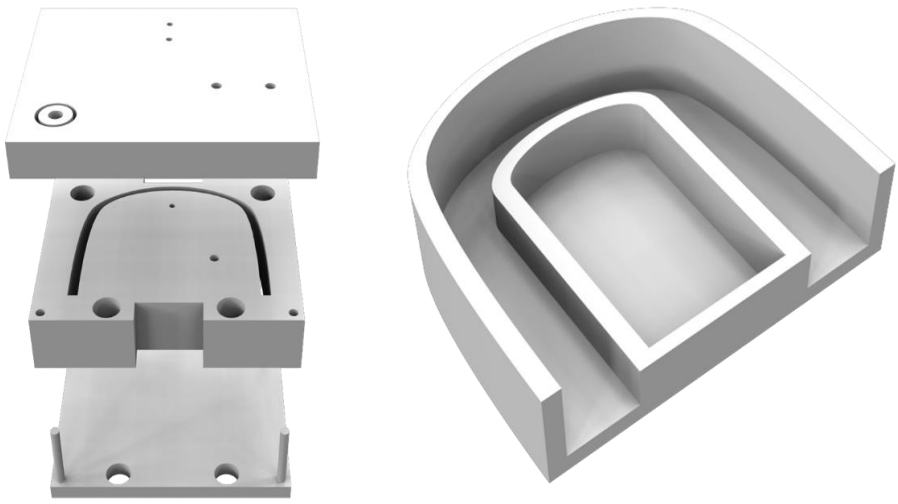

Figure 2.2.11 Design of aluminum mold depicting separated parts (left) and illustration of silicone frame of IOD. Electronics as well as battery is to be placed in the empty space in the middle.

components comprising the ZigBee IC, class-E amplifiers, transmitter coil, and power management circuits were soldered on the board manually. Finally, a 1.11 Wh litium-polymer battery (TW 801630, Taiwoo, China) was soldered to the board.

The fabricated IOD should be encapsulated as it is supposed to be applicated to the mouth. A design of the mold and the its output are illustrated in Figure 2.2.11. Medical-grade silicone elastomer (MED-6233, NuSil Technology Inc. U.S.) was used to fabricate the shape, following the method in 2.2.3.2.4. In the empty space of the fabricated frame, electronic components of IOD as well as a battery were inserted and further encapsulated by the silicone elastomer.

2.2.5. Inductive Link

The palate does not have enough spatial capacity for bulky devices to be implanted. Therefore, it is necessary to remove a battery from the implant for

miniaturization. Furthermore, conventional wireless communications using ISM band of 2.4− 2.485 GHz, requires IC chips and their peripheral components having relatively large footprints compared to available dimension of the implant. As the first priority is to meet the dimensional criteria, both the battery and the conventional communications are not used in the implant. Instead, the implant receives power and data simultaneously from an RF receive coil, via an inductive link.

2.2.5.1. Design of Coil Antennas

Coils are widely used as antennas for wireless power transmission via an inductive link. Several considerations on the transmission design are required in our application in that they are performed in bio-medium and data is transmitted simultaneously with power.

Tissue absorption of EM waves tends to increase as the wave frequency increases. However, the tendency is not correct in every frequency range. This is because the low frequency wave reflects on the kin-air interface while a high frequency wave is absorbed by tissues. Indeed, Vaillancourt demonstrated that the minimum power loss can be achieved near few mega-hertz from his research. From the power-loss graph in the literature, the RF frequency of 2.54 MHz was selected for our application [82].

Implantable devices normally have strict dimensional restrictions depending on the implantation site. From our pilot study, the dimension of the receiver antenna was determined to a 13 mm x 6.5 mm rectangle. The receiver

antenna was designed to be a rectangular planar type coil patterned on the both sides of an LCP sheet when the number of turns go higher, the higher inductance can be achieved. However, due to the gain-bandwidth relationship, it also narrows the bandwidth of the ASK-modulated signal, prohibiting sharp transitions between the 'ON' state and the 'OFF' state. Between the trade-off, the number of turns per layer was determined to be eleven with an inner dimension of a 9.3 x 2.6 mm rectangle. Both the pitch and the line width were 100 μm, which was the minimum value from the factory.

To estimate an inductance of the designed coil, the modified Wheeler formula was used for the calculation [83]. The inductance can be obtained from the formula as follows,

$$L = K_1 \mu_0 n^2 d_{avg} / (1 + K_2 \rho) \tag{2.6}$$

where K_1, K_2 are layout constants, n is the number of turns, μ_0 is the vacuum permeability, $d_{avg} = (d_{out} + d_{in})/2$, and $\rho = (d_{out} - d_{in})/(d_{out} + d_{in})$. As the formula is based on an assumption of a symmetric coil, such as spiral, square, or hexagonal, the major axis of the designed coil was scaled to a square having length of the short axis. And then the calculated value was multiplied to the scaled proportion and further multiplied by four times for the double layer. Through the calculation, the inductance of the designed coil was obtained to be 5.424 μH.

The transmitter coil was also designed and fabricated in a similar way of the receiver coil. The transmitter coil had a dimension of 30 mm x 15 mm with 14 turns at each layer, yielding a calculated inductance of 19.06 μH. The specification of the designed coil is shown in Table 2.2.2.

2.2.5.2. FEM Simulation

A finite element method (FEM) simulation was conducted to figure out a coupling coefficient between the transmitter antenna and the receiver antenna and self-inductances of the antennas. Both antennas were modeled into the designed dimensions and two lumped ports are attached to each antenna for a 2-port analysis, as shown in Figure 2.2.12. The thicknesses of the metal patterns were not modeled to achieve faster calculation,s as the thicknesses are small enough compared to the metal width. The models were split into meshes and the solution was iterated until it converges to the given criteria, maximum delta S of 0.02. As the calculation result

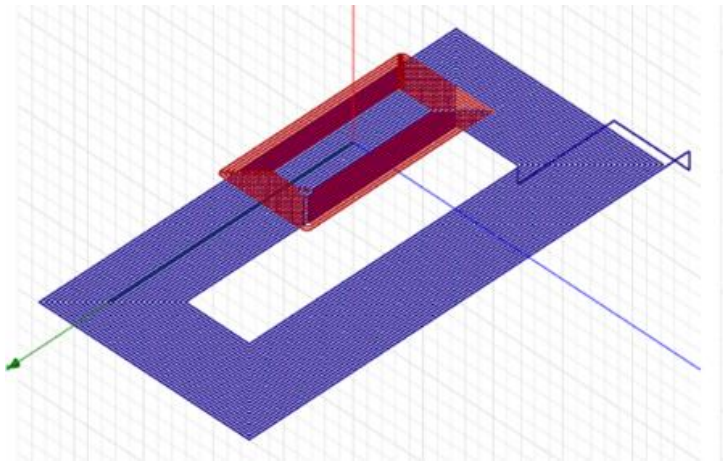

Figure 2.2.12 Finite-element method (FEM) simulation drawing using a software HFSS, ANSYS. The receiver and the transmitter coils were moldeled into the designed dimensions and their self inductances and t he mutual inductance were calculated from

Antenna Coil Specifications	Tx (intra-oral device)	Rx (implant)
Dimension	30 mm x 15 mm	13 mm x 6.0 mm
Pitch & Line-width	100 μm	100 μm
Number of turns	28 turns / 1 layer	20 turns / 2 layers
Simulated inductance	18.43 μH	4.88 μH

Table 2.2.2 Dimensions and physical properties of the designed coil antennas.

was expressed in terms of port impedances, Z_{11}, Z_{12}, Z_{21} and Z_{22}, self inductances and the mutual inductance were calculated from the port impedances using the following relationships:

$$L_{self} = img(Z_{11\ or\ 22})/(2\pi f) \tag{2.7}$$

$$L_{mutual} = img(Z_{12\ or\ 21})/(2\pi f) \tag{2.8}$$

Where L_{self} and L_{mutual} indicate the self inductance and mutual inductance respectively, *img*(Z) refers the imaginary part of Z, and f is the carrier frequency, 2.54 MHz in this application. The coupling coefficient k was calculated from the

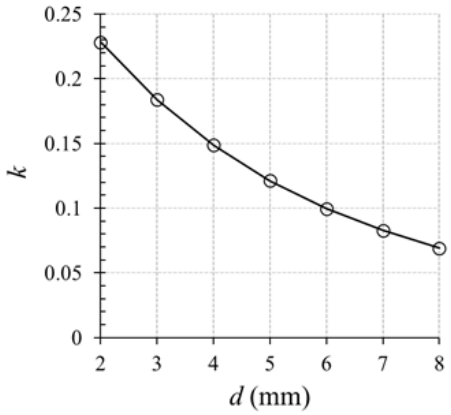

Figure 2.2.13 Calculated k plotted over distance from FEM simulation. As expected, k decreases as d increases. The obtained value of k was further used in SPICE simulation.

mutual inductance with the following relationship.

$$k = L_{mutual}/\sqrt{L_T L_R} \tag{2.9}$$

The obtained values of the self inductances were compared to the calculation results from (2.7). The coupling coefficient was plotted over the transmission distance ranging from 2 mm to 8 mm, in Figure 2.2.13.

2.2.5.3. SPICE Simulation

Using the obtained coupling coefficient, the circuit in Figure 2.2.14**a** was simulated using a SPICE simulation (OrCad PSPICE 16.6, *Cadence*, USA) to figure out powers supplied and received. The ASK modulator was disabled for the simulation because the time duration for transmitting the modulated signal was negligible over the operation time. Every component was modeled reflecting practical values including vendor-provided IC chip models. The powers at the supply and the load were measured on the telemetry distances. The results are plotted in Figure 2.2.14**b**. Each point of the coupling coefficient *k* was referenced

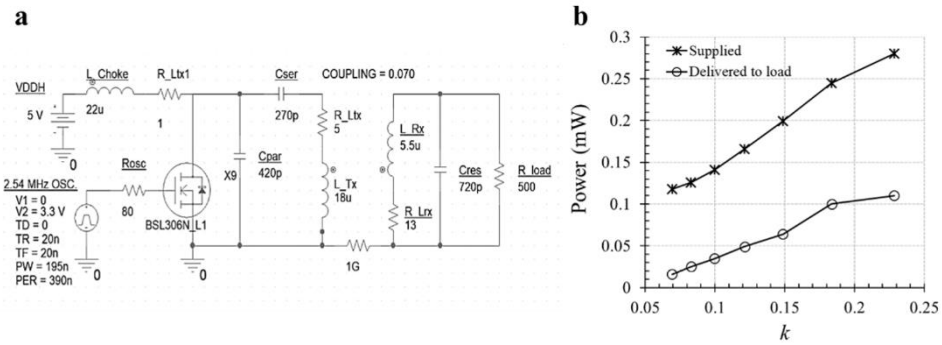

Figure 2.2.14 a, Schematic of the simulated circuit for inductive link **b,** results plotting power supplied and delivered over *k*. The values of *k* were referenced from Figure 2.2.13.

from the result in Figure 2.2.13, which represents a relationship between the telemetry distance and *k*. For every distance, the supplied power did not exceed 300 mW, which is a marginal limit for around 4-hour operation. As it is expected to operate at the distance of 5 mm in practice, the supplied power of 160 mW gives around 7-hour operation, which is a sufficient operation time for the night hours of sleep. At the time, the power delivered to the load was calculated to be around 50 mW, which was considered to be an enough value in that most of the supplied power is required for generating biphasic pulses, around 6 mW for our application.

2.2.6. Evaluations

2.2.6.1. Wireless Power Transmission

First, power efficiency of the class-E amplifier was measured. To measure the efficiency, a resistive load was connected after the transmitter antenna to represent the reflecting resistance of the receiver circuit seen from the transmitter. The reflecting resistance can be written assuming a weakly-coupled case ($k \ll 1$) as follows,

$$R_{reflect} = k^2(L_T/L_R)R_L \tag{2.10}$$

where R_L is the load resistance of the receiver [81]. The values of L_T and L_R at the target frequency were measured using a network analyzer (MS4630B, Amritsu, Japan). The value of R_L not only includes non-linear components such as diodes and transistors, but also includes active devices of which power varies over time. To estimate R_L, a test board was fabricated having the same L-C resonator in the receiver circuit and the resistive load parallelly attached to the resonator. The load

resistance was found when the voltage across the L-C resonator in the test board was the most similar to that on the actual inductive link and then the value was regarded as the equivalent load resistance of the receiver. From the equivalent resistance, $R_{reflect}$ was calculated. The circuit board having the R-L-C parallel resonance was designed and fabricated to measure the amplifier efficiency (η_{PA}), which can be expressed as follows

$$\eta_{PA} = \frac{{V_{reflect}}^2 / 2R_{reflect} + {V_{Rtx}}^2 / 2R_{Rtx}}{V_S I_S} \tag{2.11}$$

where $V_{reflect}$ is the voltage across the $R_{reflect}$ and the ground and V_s and I_s are the voltage and current from the 5 V-power supply. The total power efficiency (η_{tot}) can be obtained using the following equation:

$$\eta_{tot} = \frac{{V_{load}}^2 / 2R_{load}}{V_S I_S} \tag{2.12}$$

where V_{load} and R_{load} is the voltage and the resistance across the load, respectively. To further assess an effect of the bio-medium, measurements ont the total power efficiency and VDDH (the voltage obtained by rectifying the received signal) were conducted both on the air and the bio-medium.

2.2.6.2. Wireless Data Transmission

In our ASK demodulation strategy based on the over-threshold detection, the demodulation result may vary along the distance between the antennas because the magnitude of the received voltage varies. To mitigate the possible errors, the ASIC was programmed to permit PWM signals having duty cycles with one-tenth

period of difference. Therefore, it is important to measure duty-cycle errors of the demodulated PWM to figure out whether the error is within the error margin over operating distances. To evaluate the errors, around 10^6 bits, comprised of '0', '1', and 'F' denoted in 2.2.4.1.1., were transmitted at each distance of 0, 2, 4, 6, and 8 mm. The duty-cycle error of each demodulated bit was obtained through a software code (Matlab R2019a, MathWorks, U.S.) and their averages and standard-deviations were calculated.

2.2.6.3. Electrochemical Measurements *In Vitro*

The electrochemical impedance spectrums (EISs) and cyclic voltammetries (CVs) were measured on both Au and electrodeposited iridium oxide film (EIROF) using Solatron 1260 and 1287 systems (Solatron, U.K.) in a three-electrode cell comprised of an Ag/AgCl reference electrode and a mesh-type Pt counter electrode in a PBS solution (Gibco, Thermo Fisher Scientific, U.S). The measurement methods were similar to that in 2.2.3.1. The EIS was measured for frequencies from 1 Hz to 10 kHz by applying a sinusoidal of 10 mV amplitude without an offset. The CV curve is recorded in the range of -0.6 – 0.8 V at a scan rate of 1 mV/s at which the CVs of the electrodes can be measured in the steady state. The charge storage capacity (CSC_c) was calculated by integrating the cathodic area of the CV curve using the CorrView software package.

Voltage-transient waveforms of the electrodes were further assessed in a PBS solution to evaluate a charge injection capacity. The three-electrode cell was

again constructed and the voltage of the electrode over the reference electrode was measured while applying biphasic current pulses of 1 mA amplitude, pulse rate of 100 Hz, and duration of 540 μs. The current level was increased until the most negative (E_{mc}) and the most positive polarization (E_{ma}) were within the water window, -0.6− 0.8 V. The method from the reference [84] was used to figure out E_{mc}, by adding ($\Delta V - V_a$) on a bias level, where ΔV is the voltage transient and V_a is the access voltage.

2.2.6.4. Animal Testing *In Vivo*

An animal testing was conducted to evaluate the feasibility of the palatal implant system on soft palate stimulation. The preparation procedure of the subject was similar to the method in 2.2.1. A seven-month-old New Zealand white male rabbit was prepared and acclimated to the new environment for the first week. Sedation was induced by intramuscular injection of 0.3 ml/kg of Zoletil (tiletamine hydrochloride, zolazepam hydrochloride; Virbac) and 0.25 ml/kg of Rompun (xylazine; Bayer AG) at the same time. After sleep was induced, an incision was made along the lateral axis of the hard palate, to obtain enough space for the implant to be implanted. Then the implant was inserted toward the soft palate along the incised space. The implantation procedure is shown in Figure 2.2.15. After the insertion, the wound was closed by suturing. To deliver power and data to the implant, a transmitter coil was aligned and connected to a board of the intra-oral

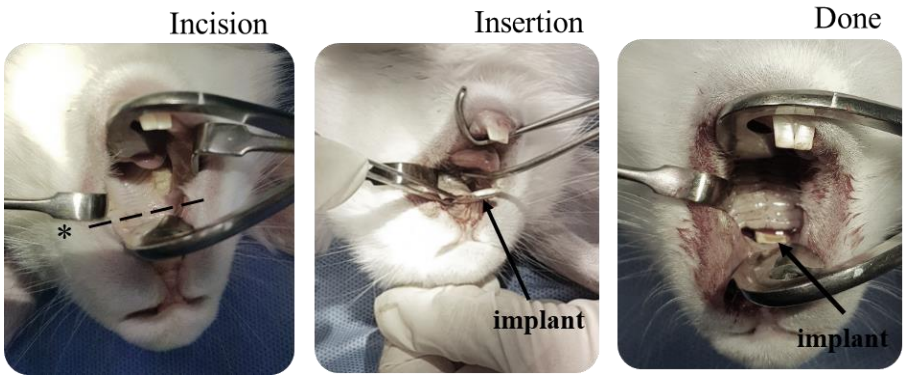

Figure 2.2.15 Insertion procedure of the palatal implant. First, a lateral incision was made on the hard palate. Then the implant was inserted from the tips. After enough insertion, implantation of the device was finished.

device. Commands to generate current stimuli having parameters of pulses of 1 mA amplitude, pulse rate of 100 Hz, and duration of 540 μs were transmitted from an external controller via ZigBee. Simultaneously, snapshots of the upper-airway were obtained using C-arm fluoroscopy (Phillips, Netherlands) in both cases where the stimuli were present and absent. All the experimental procedures were approved by the International Animal Care and Use Committee in Seoul National University Bundang Hospital.

Chapter 3

Results

3.1 Magnetic Cuff System for HNS

3.1.1. Fabricated System

The fabricated system is depicted in Figure 3.1.1. The MENCE had two electrode sites for a neural interface and connector pads to access to the pulse generator (Figure 3.1.1**a**). The stimulation site area was 5.6 mm^2 with a width of 3.5 mm and a height of 1.6 mm. The internal cuff radius was 1.27 mm, which targets a hypoglossal nerve (Figure 3.1.1**b**). The measured magnetic flux density of the magnet was 0.112 T, which is lowered by 20 % compared to that before the lamination process, with both measured at room temperature. The external pulse generator is shown in Figure 3.1.2. On the board, there were 9 V battery for powering the device and multiple mechanical switches for parameter setting. The portable pulse generator was able to be connected to the MENCE through a FFC connector.

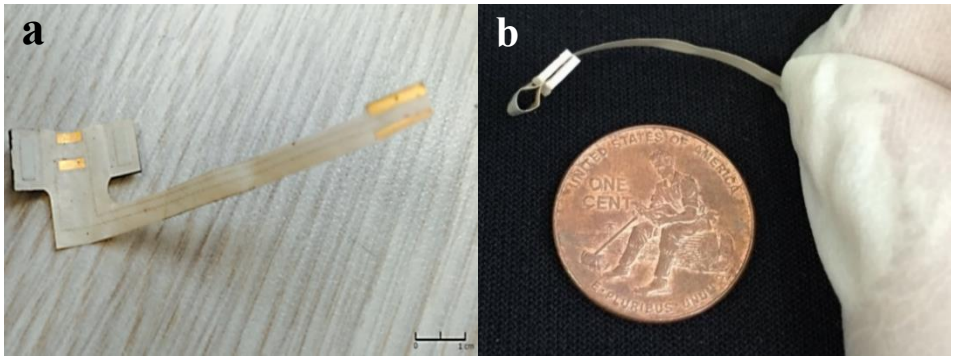

Figure 3.1.1 a, Fabricated magnet-embedded nerve cuff electrode (MENCE) and **b,** its side view in closed form

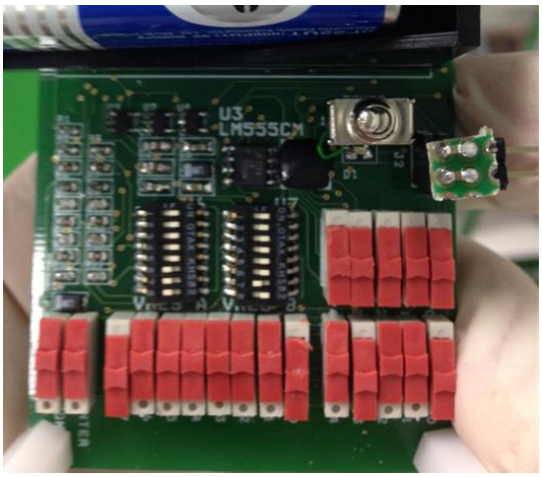

Figure 3.1.2 The external pulse generator fabricated on PCB. Mechanical switches were soldered on the board to set stimulation parameters.

3.1.2. Electrochemical Measurements *In Vitro*

Figure 3.1.3**a** shows the EIS result of the fabricated electrodes (n=10). The average values and error rates of the samples are plotted over the frequency ranging from 0.1 Hz to 100 kHz. The impedance was 0.638∠-67.8° kΩ (± 0.210∠-3.27° kΩ) at 1 kHz and 5.27∠-82.1° kΩ (± 0.694∠-1.07° kΩ) at 100 Hz. The average values of access resistance and cut-off frequency were 0.145 kΩ (± 1.74 Ω) and 3.98 kHz (± 3.84 Hz), respectively. The magnitude of the impedance was a lot lower than that of prior arts due to its high site area [79, 85]. A representative CV curve of the electrode is plotted in Figure 3.1.3**b**. The average value of the CSCc was 1.69 mC/cm2 (± 0.602 mC/cm2). For the site area of 5.6 mm^2, the CSC_c yields the capacity of 94.6 μC, which is enough value for the required amount of charge of 13 nC, for our application.

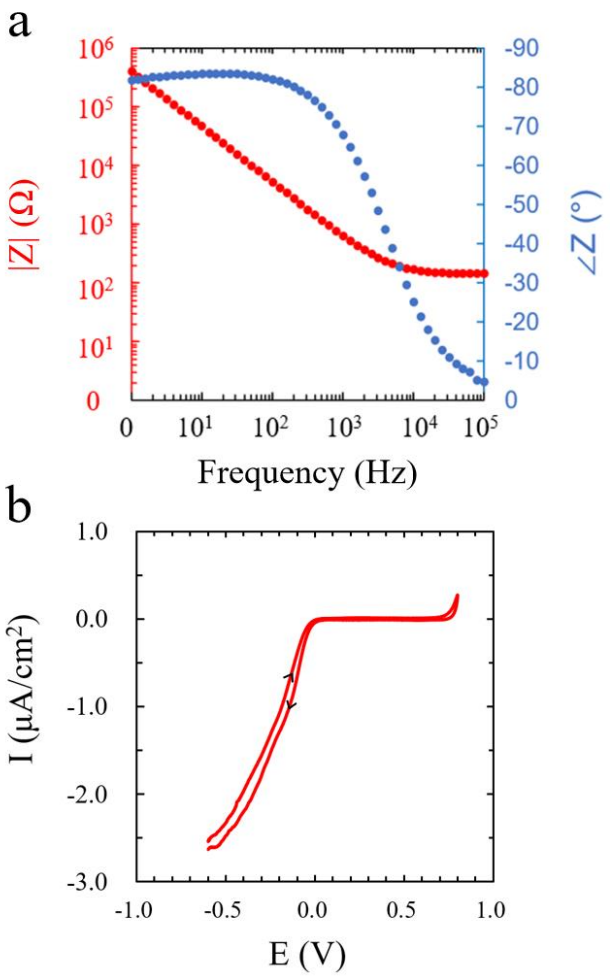

Figure 3.1.3 Results of *in* vitro assessments of MENCE **a** Absolute value and phase degree of the impedance, **b** cyclic voltammogram

3.1.2. Animal Testing *In Vivo*

In vivo results of the hypoglossal nerve stimulation are shown in Figure 3.1.4. Tongue protrusion was clearly observed with bare eyes during the stimulation (Figure 3.1.4**a**). The stimulation threshold of 41.0 μA induced a mild reaction while strong protrusion of the tongue was observed over 53.2 μA. Further research will be necessary to determine the optimum level of the stimulation for actual

application. Figure 3.1.4**b** shows the corresponding C-arm fluoroscopy snapshots of the experiment. It is seen from the figure that the strong contraction of the genioglossus changed position of the cuff electrode toward to the mandible. Figure

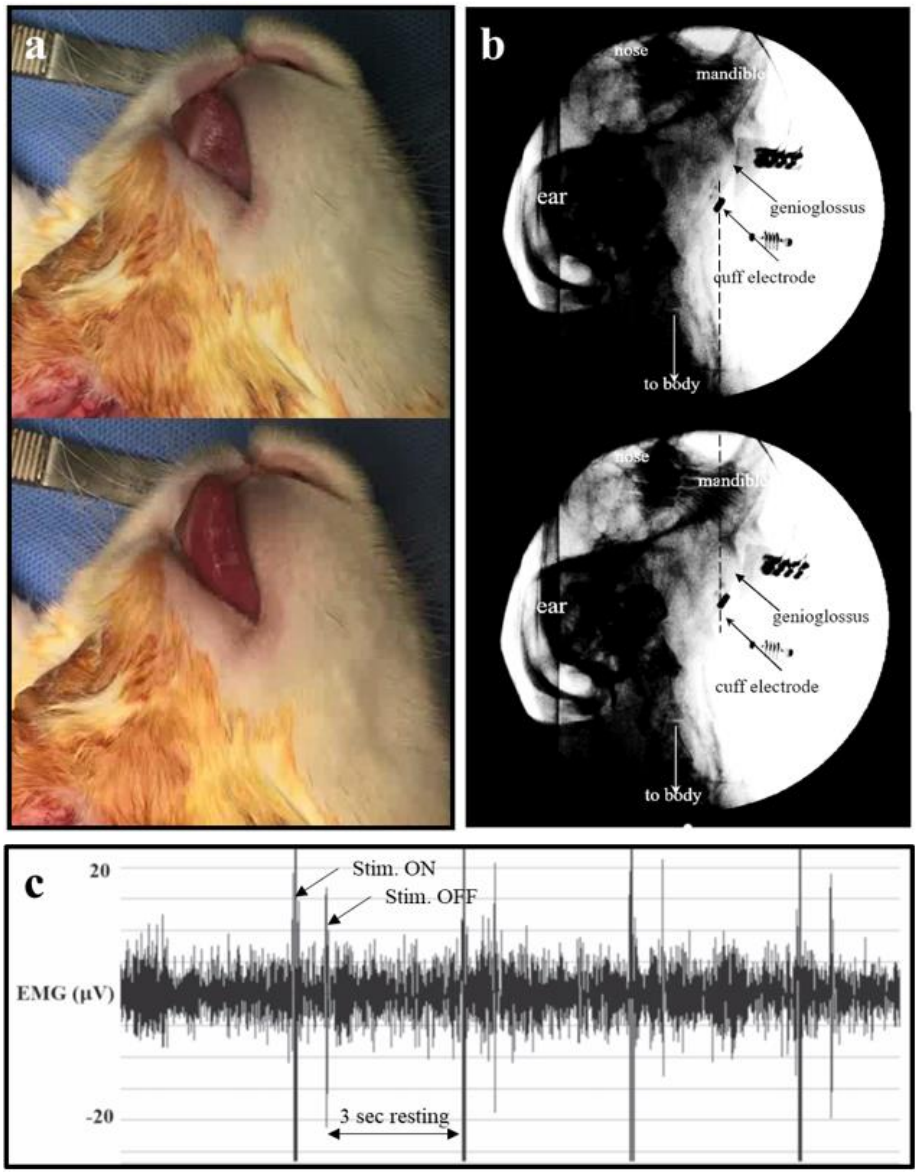

Figure 3.1.4 Stimulation results of hypoglossal nerve stimulation observed with **a,** bare eyes, **b,** C-arm fluoroscopy, and **c,** EMG. Protrusion of the tongue was observed with bare eyes and the cuff electrode was forced to the mandible due to the contraction of the genioglossus. The synchronized peak of EMG supports the evidence of the contraction.

3.1.4**c** shows EMG signal recorded at the neck at the same time. Large peaks were detected the start and the end of the stimulation with three seconds of resting. The synchronized EMG peaks supports the evidence of the genioglossus contraction.

3.2. Palatal Implant System for SPS

3.2.1. Pilot Study *In Vivo*

With stimulation in the frequency range of 70–120 Hz, the strongest contraction behaviors on the soft palate were observed. There were mild responses in the range of 130–150 Hz but no responses under 60 Hz and over 160 Hz. The threshold level was 1.10 mA with duration and frequency of 636.3 μs and 100 Hz, respectively. The upper airway was recorded with C-arm fluoroscopy as shown in Figure 3.1.4. Both snapshots were taken at points when the soft palate was maximally relaxed. Elevation of the soft palate was observed when the stimulation was applied. As a result, broaden retropalatal region was observed as shown in the bottom in Figure 3.2.1.

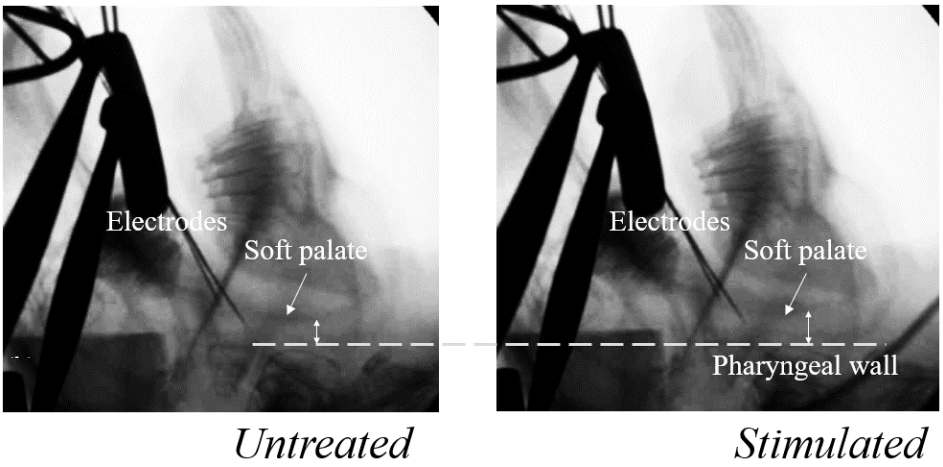

Figure 3.2.1 Snapshots of the upper airway without stimulation (top) and with stimulation (bottom) recorded via C-arm fluoroscopy. The soft palate was elevated when the stimulation was applied, resulting in retropalatal opening.

The fabricated implant mock-up is shown in Figure 3.2.2**a**. The body of the mock-up had a dimension of 21 mm x 10 mm, with a thickness of 2 mm. The two shanks, each with 13 mm-long, have 1.5 mm widths with 0.7 mm-thickness. In the series of pictures in Figure 3.2.2**b**− **d**, the insertion process of the fabricated mock-up is shown. There was no evidence of any adverse events after the mock-up was inserted. The mock-up stayed well for two months but protruded after the period. It seemed that the protrusion was due to the bulky size of the implant, therefore dimension of the implant was modified when fabricating an actual implant.

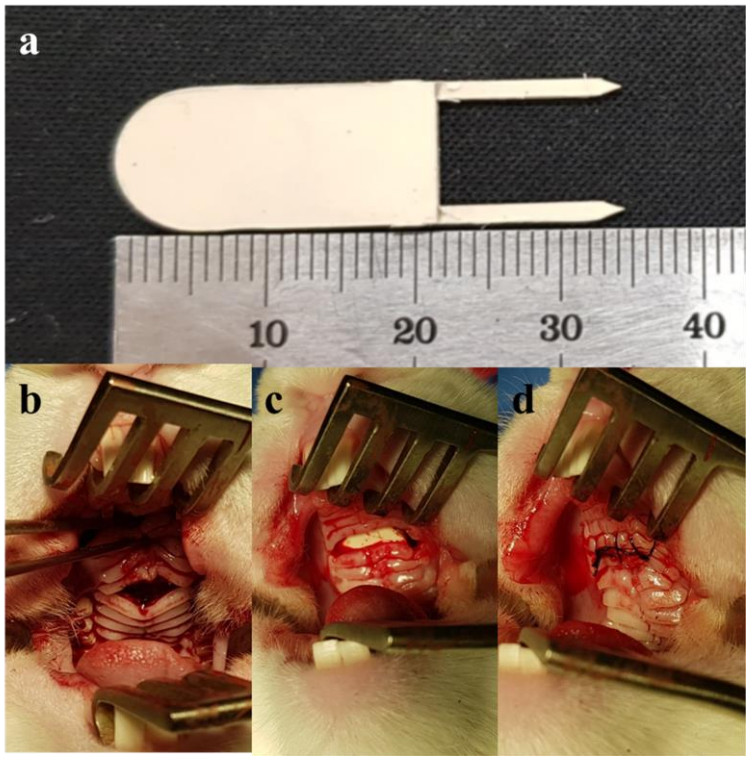

Figure 3.2.2 a, Fabricated implant mock-up and its insertion process to the palate. **b,** Incision of the hard palate, **c,** implantation of the mock-up, and **d,** suturing of the wound.

3.2.2. Fabricated System

The fabricated palatal implant system is shown in Figure 3.2.3**a**. The implant consists of multiple LCP layers including functional layers of the coil, electrodes facing top and bottom, and adhesion layers (Figure 3.2.3**b**). The

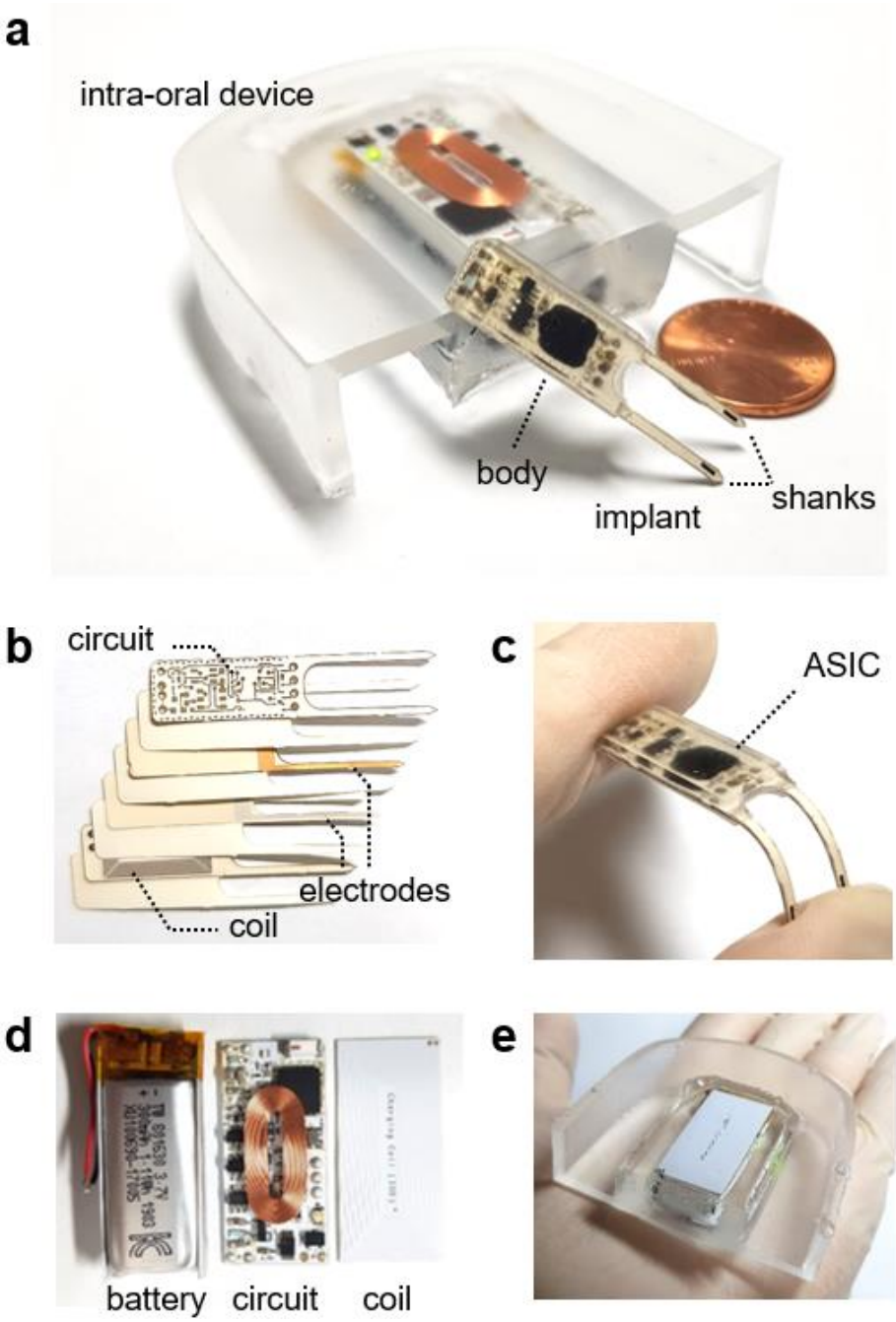

Figure 3.2.3 Fabricated palatal implant system. **a,** Intra-oral device and palatal implant. **b,** Layer configurations of the implant (unnoted layers to be adhesion layers). **c,** Flexible shanks of the implant. **d,** Electronic parts of the intra-oral device, consisting of rechargeable battery, circuit board, and coil. **e,** The intra-oral device seen at the other side.

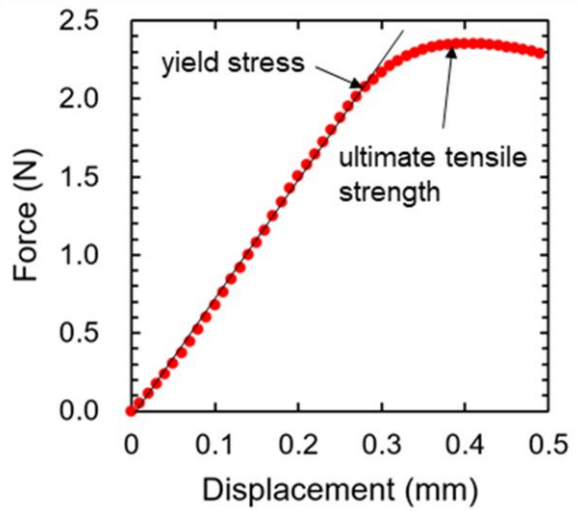

Figure 3.2.4 A representative plot of the buckling test conducted to the implant. One side of the shank was fixed to a force sensor attached to a data acquisition (DAQ) unit (Nano 17, ATI Industrial Automation Inc., U.S.) and the other side was pinned to an acrylic plate placed on the bottom. A single-axis oil hydraulic micromanipulator attached with a motor driver (MO-81, Narishige, Japan) and the force sensor, moved downward at a speed of 100 μm/s. The force exerted on the shank was recorded by the function of the displacement.

fabricated implant had a dimension of 19 mm x 8.0 mm with thickness of 3 mm including the encapsulation silicone at the body. The size of each shank was 13 mm x 1.5 mm with thickness of 0.7 mm. The shanks were rigid enough to be inserted to the soft palate muscle but also flexible so that they could be easily bendable with hands (Figure 3.2.3**c**). To characterize the mechanical property of the shank,

Material (width x thickness)	LCP shank (1200 μm x 700 μm)	Tungsten rod (Φ = 200 μm)	Silicon probe (100 μm x 100μm)	COP (650 μm x 200 μm)
Elastic modulus (GPa)	1.322 (n = 5)	5.868 (n = 5)	2.964 (n = 5)	2.001 (n = 4)
Yield strength (N)	2.51 ± 0.32	0.23 ± 0.11	0.27 ± 0.1	0.22 ± 0.008

Table 3.2.1 Result of the buckling tests on LCP shanks and its comparison to previous studies.

	Dimension	Turns	L	R	Q_L
Transmitter	30 mm x 15 mm	28 (2 layers)	17.50 μH	16.30 Ω	16.86
Receiver	13 mm x 6.0 mm	20 (2 layers)	5.475 μH	13.05 Ω	2.990

Table 3.2.2 Properties of fabricated antenna coil. Absolute value (red) and phase degree (blue) of the electrode impedance (left), cyclic voltammogram of the electrode (right).

buckling tests (n = 5) were performed and the force-displacement plot was drawn (Figure 3.2.4). The average yield strength was calculated to be 2.51 N (± 0.32) and the elastic modulus was 1.32 GPa (± 0.17). The result indicates that the LCP shank with 700 μm thickness give more flexibility than the tungsten rod, silicon probe, and COP, while giving a higher yield strength (Table 3.2.1) {Lee, 2012 #169; Shim, 2019 #168}. A lithium-polymer rechargeable battery (Tw801630, Taiwoo,China; 1.11 Wh), circuit board with charging coil, and transmitter coil are the electronic components of the intra-oral device (Figure 3.2.3**d**). The device was able to operate for 6 hours with heat dissipation of 2 °C increase in the soak test, which will be discussed in 4.2.1. Figure 3.2.3**e** provides the opposite view of the IOD from Figure 3.2.3.**a**.

Properties of the fabricated coil antennas are arranged in Table 3.2.2. Dimension of each coil was determined based on the constraint of the biological dimension. Quality factor, Q, of each coil was intentionally lowered to obtain enough bandwidth for ASK modulation. As the gain and the bandwidth are inversely proportional to each other due to the gain-bandwidth product, smaller Q was selected at the expense of lowered power efficiency.

3.2.3 Wireless Power Transmission

First, coupling coefficient k was measured by varying the distance between the coils. The value of k was measured to be 0.050− 0.208, which is the value roughly 22 % lower than the simulation results in 2.2.5.2, at the distance of 2− 8 mm. The discrepancy between the results of measurement and simulation, might be due to misalignment in the measurement and simplified model of the simulation. Received peak-to-peak voltage at the coil, V_{Rpp}, has a proportional relationship with k as follows,

$$V_{Rpp} = Ak\sqrt{\frac{L_R}{L_T}}Q'_T Q'_R V_s \tag{3.1}$$

where A is the voltage gain of the amplifier, L_R and L_T are inductances of receiver and transmitter respectively, Q'_T and Q'_R are the loaded Q's of the receiver and the transmitter respectively, and V_s is the supply voltage. The coupling coefficient k and the received peak-to-peak voltage V_{pp}, are plotted in Figure 3.2.5**a** showing a trend of linear relationship**.** The minimum value of V_{pp} was 5.9 V, which is still a valid compliance considering that the required minimum compliance voltage was 2 V in a PBS solution for our 1 mA stimulation and the compliance *in vivo* was reported to be about 3 times higher than *in vitro* [86].

Reflected resistance was calculated from equation (2.10) using the obtained k and the amplifier efficiency was measured at each distance. The averaged amplifier efficiency was 65.6 % (Figure 3.2.5**b**), which is lower than routinely-reported efficiencies of 85% from other references [80]. This is due to relatively low Q'_T, as our application aims both power and data transmission.

Supplied power from the source in the intra-oral device and power delivered to the load in the implant were plotted in blue dots in Figure 3.2.5**c**. The maximum supplied power was 255 mW, which gives 4.35 hours of operation. The measured total power efficiency, P_s/P_l, is shown in red dots in Figure 3.2.5**c**. The efficiency was 4.87− 20.7 % in the telemetry distance. At the distance of 8 mm, which was the maximum distance that the circuit in the implant operated, the load power was measured to be 10 mW. Figure 3.2.5**d** shows a comparison plot of the

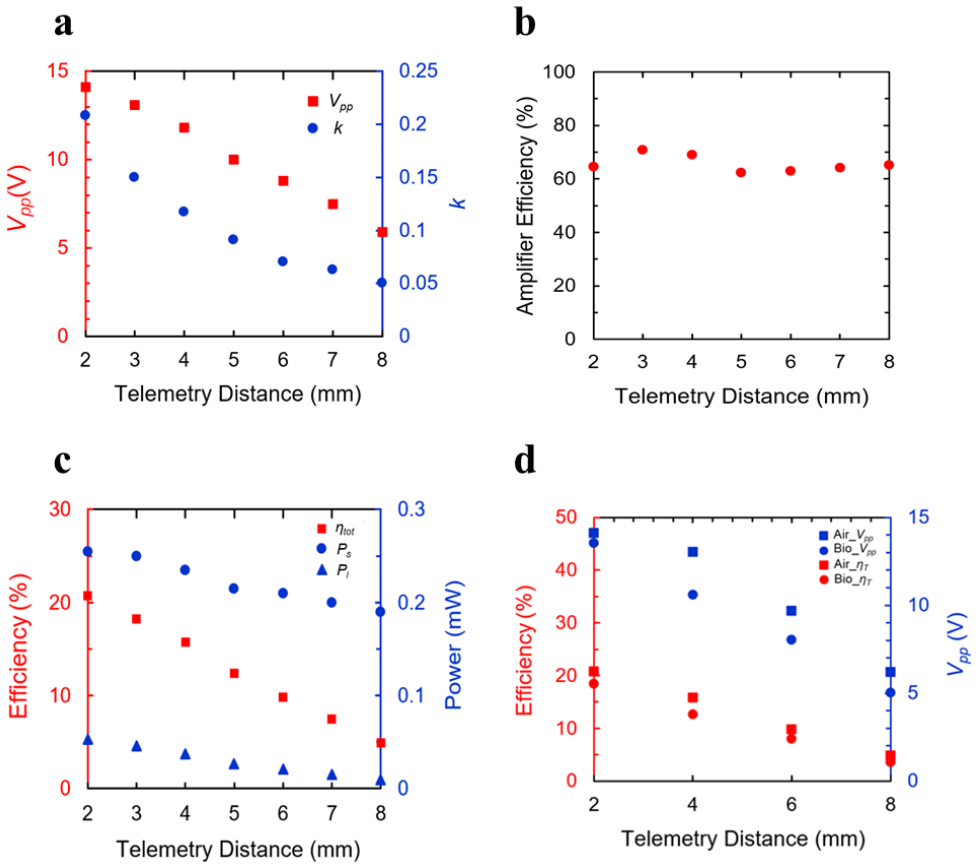

Figure 3.2.5. Power transmission results of the palatal implant system varying telemetry distance ranging 2− 8 mm. **a,** VDDH and *k* **b,** measured amplifier efficiency **c,** total power efficiency and power of supply and load **d,** comparison of air and bio-medium in terms of VDDH and total power efficiency.

air and the bio-medium in terms of V_{pp} and the total efficiency η_T by varying the distance. Both V_{pp} and η_T were lowered in the bio-medium than the air as expected, but the decreases were not significant but have a minor effect on the decreased compliance.

3.2.4. Wireless Data Transmission

The result of the duty-cycle measurement is shown in Figure 3.2.6. Every bit, 0, 1, and F, represented as duty-cycle of PWM, was measured to have an averaged error within the margin, 10 %, at all telemetry distances ranging 2− 8 mm. The error increased at the telemetry distances over 4 mm, where the large drop of V_{pp} in air was observed from Figure 3.2.5**d**. It seems that the decreased signal level affected the performance of the ASK demodulator. Yet, the errors were in tolerance,

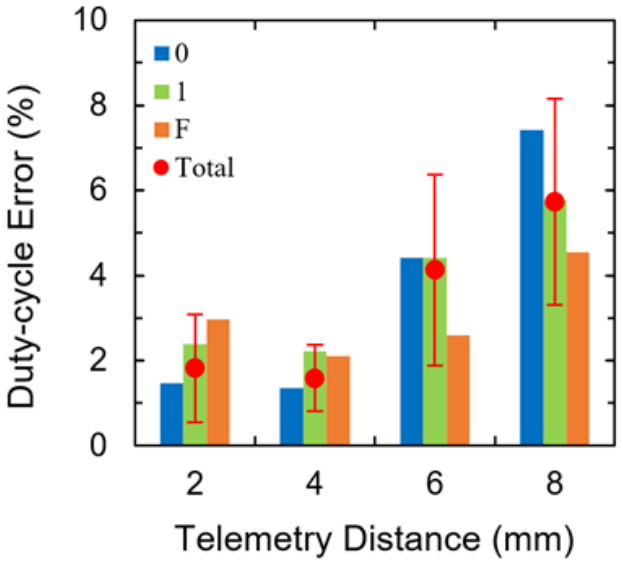

Figure 3.2.6 Measured telemetry error in terms of duty-cycle. Error values of each bit and their averages are plotted over the telemetry distance.

implying successful data transmission at the tested distances.

3.2.5. Electrochemical Measurements *In Vitro*

Averaged EIS results (n = 8) of the fabricated Au and EIROF electrodes are shown in Figure 3.2.7, representing averaged values of magnitude and phase of the measured impedances with their standard deviation noted. The low cut-off of

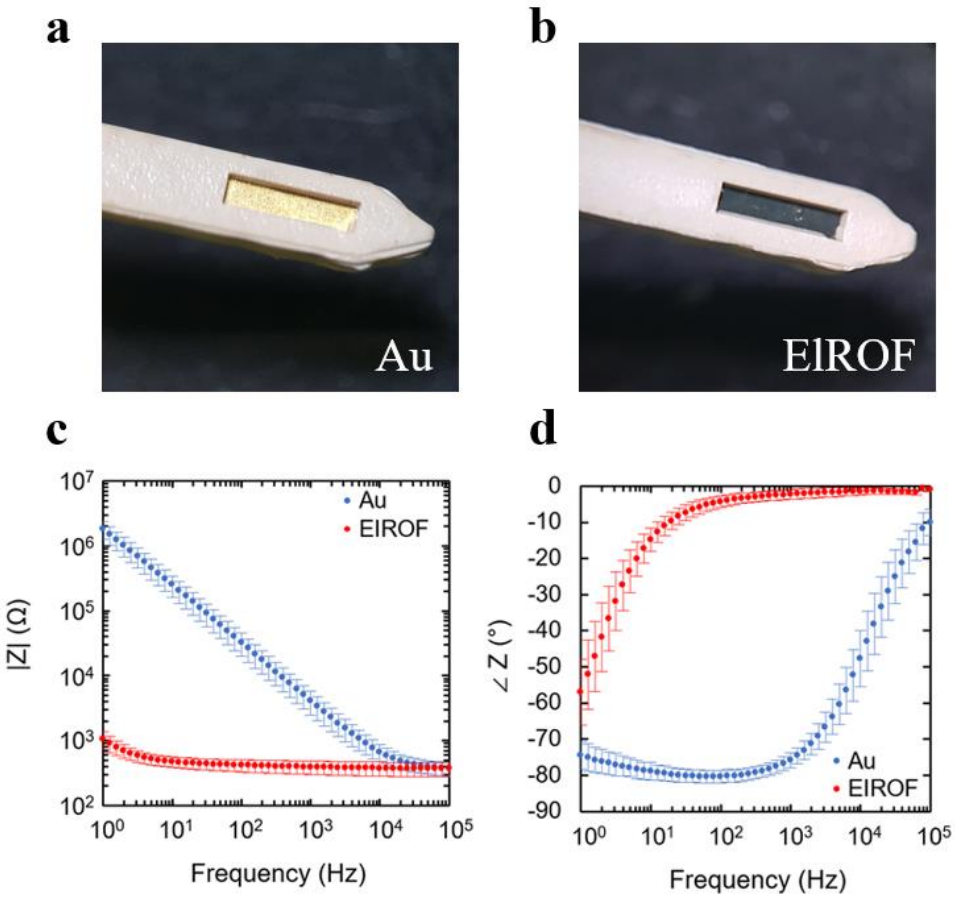

Figure 3.2.7 Fabricated **a,** Au and **b,** EIORF electrode image and results of EIS. The impedance of EIROF was nine-times lower than that of Au. **c,** The magnitude in logarithmic scale. **d,** Phase in degree. EIROF exhibits resistive impedance at 1 kHz while Au remains capacitive.

EIROF is due to EIROF's high porosity which is a highly desirable property for a stimulation electrode [87]. The magnitude of EIROF was measured to be 390 Ω at 1 kHz, which is nine folds lower than that of Au, 4.13 kΩ, and the EIROF already exhibits a near-resistive phase while Au stays capacitive at 1 kHz. The high porosity of EIROF electrode contributes to a higher charge injection/storage capacity, as shown in Figure 3.2.8.

Figure 3.2.9 shows a representative plot of cyclic voltammetry conducted on Au and EIROF. The averaged cathodal charge storage capacity (CSC_c) of EIROF was 62.25 mC/cm^2 with the standard deviation of 19.17 mC/cm^2, while 0.7019 mC/cm^2 with 0.2695 mC/cm^2 for Au. EIROF having the porous surface has a higher electrochemical surface area (ESA) per unit geometric surface area (GSA), thereby exhibits a about ninety-times higher CSC_c than Au. The amount of cathodal charge, which is to be used in this experiment, is 270 nC (1 mA x 270 μs). Therefore, both CSC_c's of Au and EIROF were measured to be enough for the stimulation.

Voltage transients of Au and EIROF are plotted in Figure 3.2.10**a** and

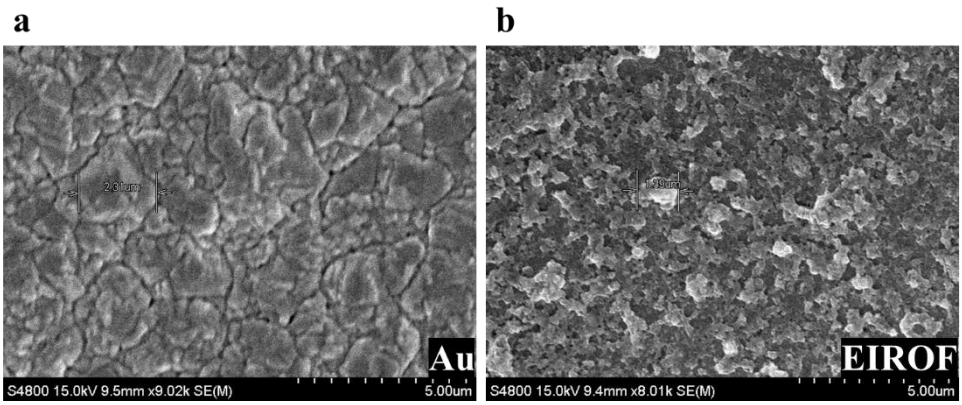

Figure 3.2.8 Scanning electron microscopy (SEM) images of **a**, Au and **b,** EIROF surface. Both images are taken at the same magnification (S-4800, Hitachi, Japan).

Figure 3.2.10**b**, respectively. From the bias level (V_{ipp}), an electrode faces *iR* drop at immediately after current pulse was applied. Amount of the potential drop is called an access voltage, which contains access resistance of the electrode as well as electrolyte. This voltage drop should be excluded for evaluating a charge injection capacity as they do not participate in the polarization across the electrode-electrolyte interface. Thus, the most negative polarization E_{mc} for cathodal phase can be calculated as follows

$$E_{mc} = E_{ipp} + (V_{drv} - V_a) \tag{3.2}$$

where V_{drv} is the driving voltage in Figure 3.2.8 [87, 88]. The most positive polarization (E_{ma}) can be similarly obtained using equation (3.2) for the anodic phase. Both E_{ma} and E_{mc} must not exceed a voltage range that occurs irreversible faradaic reaction, namely, -0.6− 0.8 V (vs. Ag|AgCl reference) for the water limit. From Figure 3.2.10, it can be seen that both Au and EIROF do not exceed the water

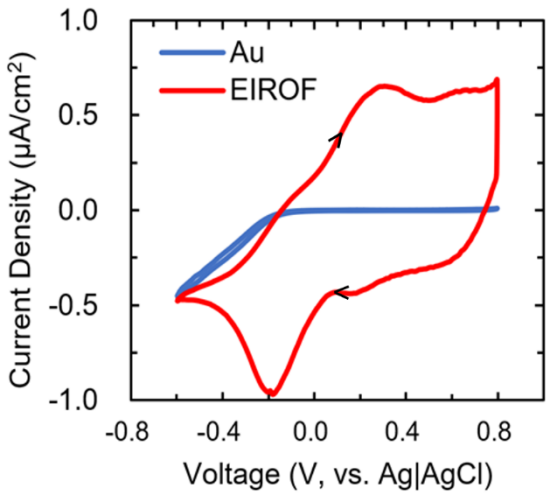

Figure 3.2.9 Representative plots of the cyclic voltammetry of Au (blue) and EIROF (red). The plots were extracted from fifth cycle of the voltammetry. CSC_c of EIROF was measured to be 88.9-fold higher than that of Au.

limit under stimulation parameter of 1 mA amplitude, 540 μs duration, and 100 Hz pulse rate. The polarization voltage across the interface, V_p, was drastically decreased for EIROF due to its low impedance, complying the result in Figure 3.2.7. Figure 3.2.11**a** shows the transient result with varying current level from 0.4 mA to 2.0 mA. Values of E_{mc} were far less than the cathodic water limit, -0.6 V, as can be

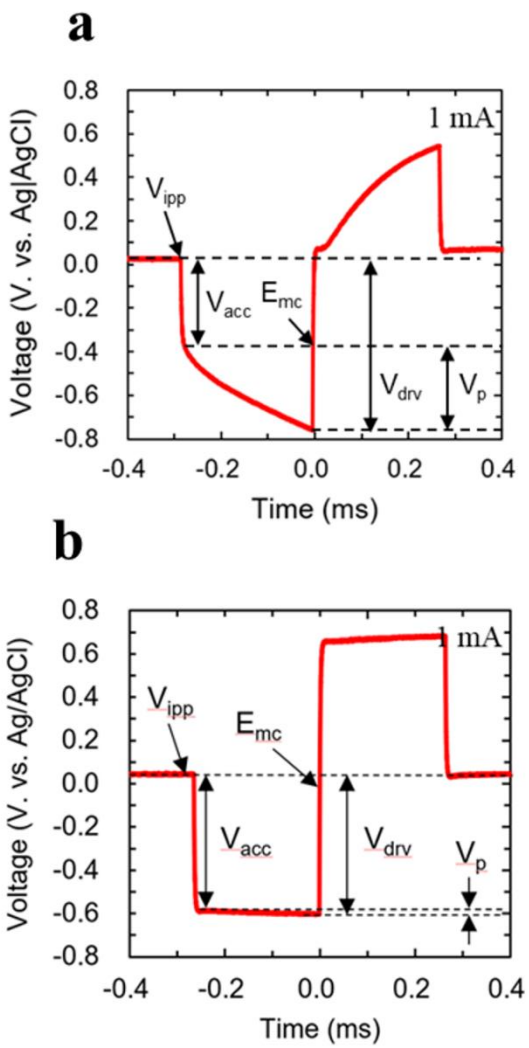

Figure 3.2.10 Voltage transient waveforms of **a,** Au **b,** EIROF. Biphasic current pulse was applied to soaked electrodes in PBS solution and the transient voltage across the electrodes was measured.

seen from the plot.

To figure out the charge injection limits of Au and EIROF, voltage transients of Au and EIROF were measured and plotted in $\underline{V_{drv}}$ and E_{mc} as a function of charge density (Figure 3.2.11**b**). Driving voltages of both Au and EIROF were increased as the charge density increased, but E_{mc} of EIROF remained relatively constant compared to E_{mc} of Au. This implies that V_a takes up most of the driving

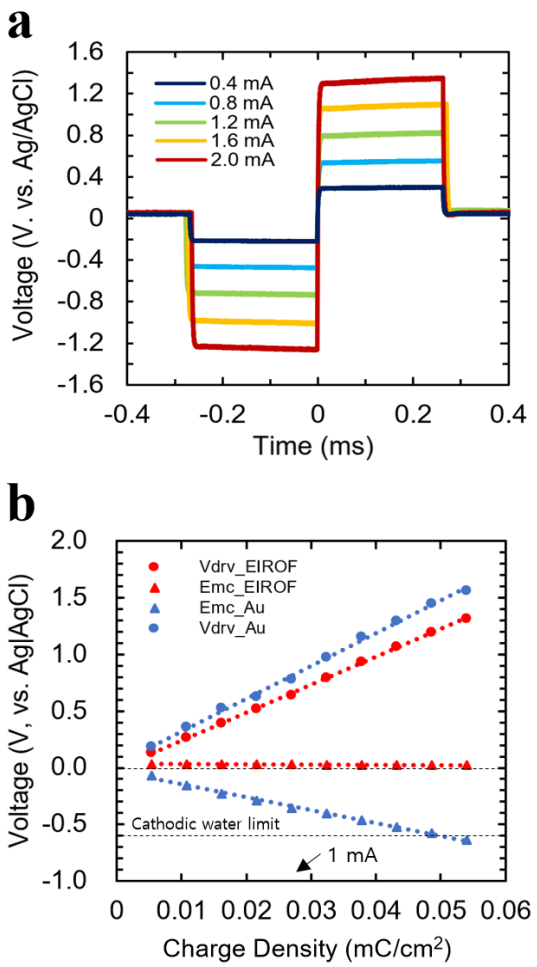

Figure 3.2.11 a, Voltage transient waveforms of EIROF by varying current level from 0.4 mA to 2 mA. E_{mc} was not exceeded even at 2.0 mA. **b,** Plots of V_{drv} and E_{mc} of EIROF and Au versus charge density. Au exceeded the water limit at 0.054 mC/cm^2.

voltage for EIROF and the polarization across the interface is very low. Au exceed the cathodic water limit when a charge density of 0.054 mC/cm^2 was applied while EIROF still remained in the limit. EIROF exceeded the water limit at 0.162 mC/cm^2, when the current level of 6 mA was applied. From the voltage transient results, it was shown that EIROF has around three-time higher charge injection limit, and both Au and EIROF were safe enough for the charge density of 0.027 mC/cm^2.

3.2.6. Animal Testing *In Vivo*

Figure 3.2.12**a** and Figure 3.2.12**b** shows the upper-airway snapshots under untreated conditions (inhalation, exhalation) while Figure 3.2.12**c** shows the behavior of the stimulation. The untreated results were provided as controls of the *in vivo* stimulation assessment. Any change of the soft palate was not noticeable in both inhalation and exhalation under the untreated conditions. On the other hand, distinctive deformation of the soft palate was observed when the stimulation was applied, leading a broaden retropalatal region. Further measurements to demonstrate therapeutic effect of the stimulation could not be performed because the subject was not OSA-modeled in the experiment. However, distinctive deformation of the soft palate was observed when the stimulation was applied, leading a broaden retropalatal region

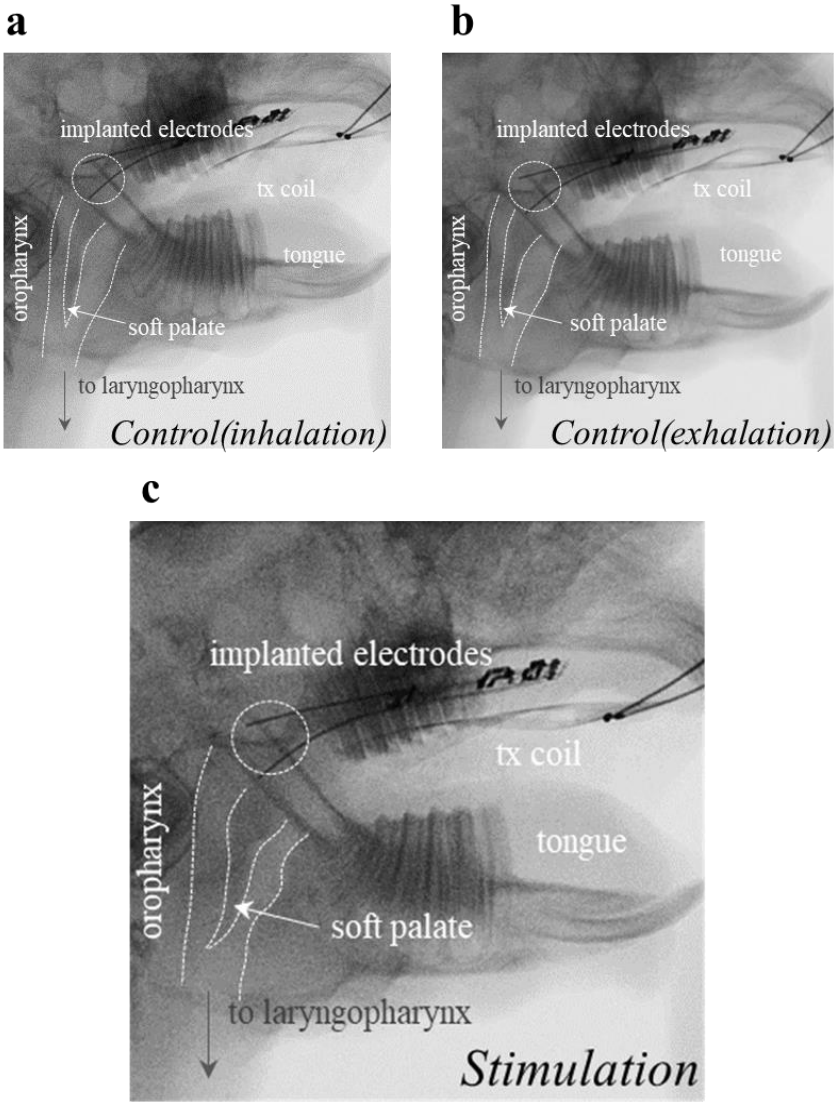

Figure 3.2.12. Snapshots of the upper-airway observed from C-arm fluoroscopy. **a,** Inhalation with no stimulation. **b,** Exhalation with no stimulation **c,** Stimulation applied. Distinctive constraint of the soft palate was observed during stimulation compared to the controls, **a**, **b.**

Chapter 4

Discussions

4.1 Magnetic Cuff System for HNS

4.1.1. Cuff-to-Nerve Diameter Ratio

Given that the curled radius of the MENCE cannot be regulated after it is installed, the cuff-to-nerve diameter ratio (CNR) may play a critical role in determining whether the cuff fits the nerve well. According to Naples *et al*., the relationship between a change in the internal radius and the pressure can be expressed as follows [68].

$$\Delta r = \frac{r_c \Delta P}{E[(r_c+h)^2 - {r_c}^2]} * [(1-v) + (1+v) * \frac{(r_c+h)^2}{{r_c}^2}] \quad (4.1)$$

Δr= Change in the Internal Radius

ΔP = Change in the Internal Pressure

r_c = Internal Cuff radius

h = Cuff Wall Thickness

E= Young's Modulus of the Substrate

v = Poisson's Ratio of the Substrate

It has been noted that the application of 20 mmHg of pressure to a peripheral nerve from a cuff electrode can evoke interference in the intraneural blood flow [12, 19]. Therefore, setting ΔP = 20 mmHg in equation (4.1) derives a critical Δr at which the cuff electrode can be installed without inhibiting the blood flow of the nerve. The MENCE had an internal cuff radius of 1.27 mm with a wall thickness of 50 μm. Young's modulus and Poisson's ratio are set to 2.5 and 0.4, respectively (as the Poisson's ratios of Vecstar CT-Z and CT-F are not provided,

that of the Sumikasuper E5000 is used instead). Replacing the variables in equation (4.1) with the values above, the Δr becomes 0.355 mm, which sets the critical CNR to 0.781 if the cuff is installed on a nerve with the same diameter. This means that the nerve will not undergo necrosis until the cuff radius becomes smaller than the nerve radius by 21.9 %. Thus, it is safe until the CNR of the MENCE reaches 0.781, the critical CNR, due to a poor installation or nerve swelling caused by scar tissue growth.

However, the above calculation is derived while neglecting the weight of the cuff itself. This is reasonable because the weight of conventional cuffs is too light compared to the pressure that evokes interference of the intraneural blood flow. On the other hand, because the MENCE has two Sm-Co magnets with LCP encapsulation layers, the validity of this assumption is unclear. The total weight of the MENCE is 0.873 mN, with 0.275 mN accounted for by the magnets. By taking the weight of the MENCE into consideration, additional 0.231 mmHg of pressure is added to the nerve, meaning that 0.873 mN of force is placed on the 28.26 mm^2 area of a half cylinder. The ΔP value, representing the pressure exerted on the nerve excluding the pressure from the weight of the MENCE, should then be 19.77 mmHg to calculate the critical CNR. The amount of the decrease in the ΔP becomes 1.15 % here, followed by the decrease in Δr of an identical amount, as Δr is directly proportional to ΔP in equation (4.1). Thus, Δr becomes 0.351 mm, establishing a critical CNR of 0.783, only showing an increase of 0.256 % compared to the result when neglecting the weight of the MENCE. Thus, we can conclude that this remains reasonable even if we neglect the weight of the MENCE when calculating

the CNR.

4.1.2. Magnetic Forces

As claimed several times before, one of the great advantages of using a MENCE is that the cuff can be repeatedly installed and detached easily. However, it is necessary to be demonstrated that detaching the MENCE from the nerve is indeed easy despite the presence of the attractive force between the magnets. To evaluate this, the amounts of force needed to detach the magnets along the lateral and vertical directions are measured over the displacement. The detached state is defined at the point that the direction of force is inverted, changing from increasing to decreasing. As shown in Figure 4.1.1, the magnets are detached when 0.18 N of force is applied in the lateral direction while 0.28 N of force is needed to detach the magnets in the vertical direction. Therefore, we can say that 0.18 N in the lateral direction is the critical force to slip off the MENCE. Considering that 1 N is the

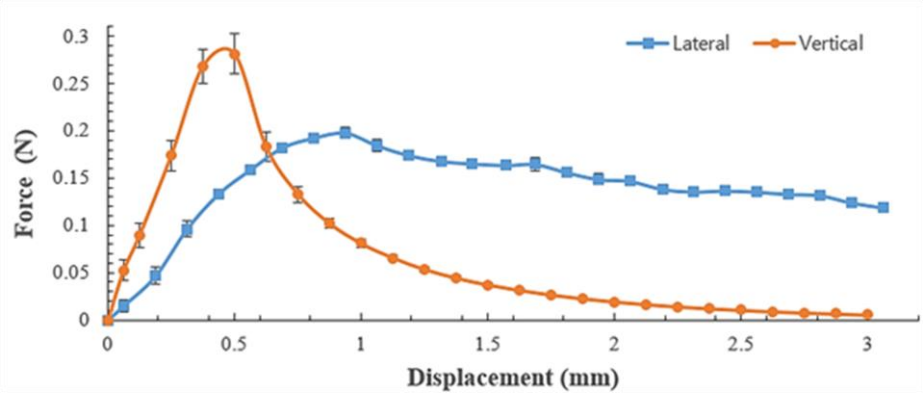

Figure 4.1.1 The forces needed to slip off the MENCE in the lateral direction (■), and the vertical direction (●). A critical force was defined at the point when the direction of gradient was changed from positive to negative.

amount force needed to hold up an object that weighs 100 g, 0.18 N is indeed a small amount of force. However, it is difficult for the MENCE to be detached in a body by itself, as the force should be applied to one magnet while the other magnet remains fixed. To summarize, users can slip off the MENCE by applying only 0.18 N of force in the lateral direction without any concern of the MENCE slipping off by itself.

4.1.3. Simulation Parameters

Though we used a current amplitude of 0.106 mA in the *in vivo* assessment, we also attempted to find a threshold. We decreased the stimulation level while

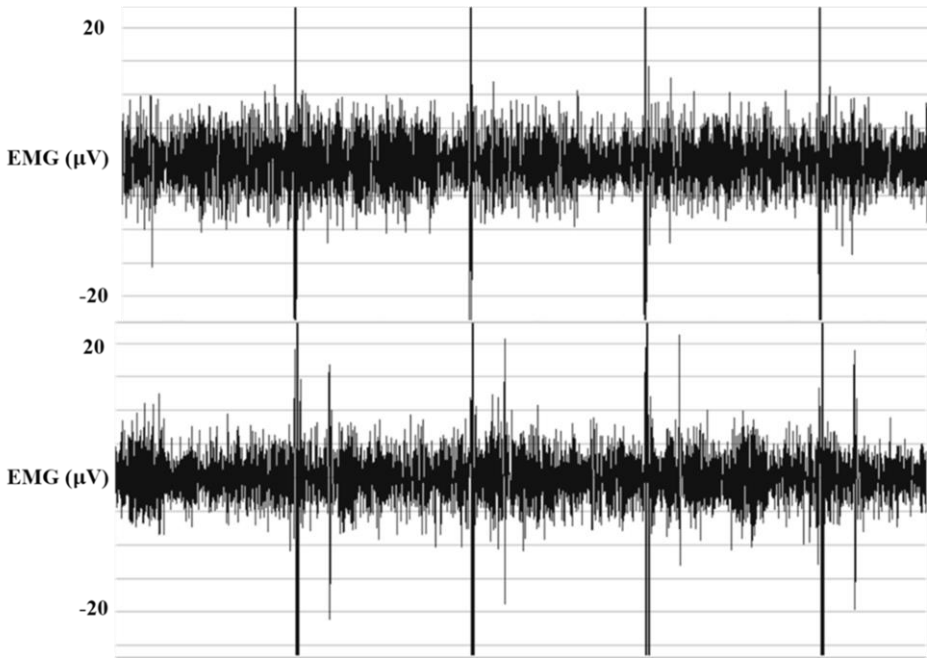

Figure 4.1.2. The measured EMG data at current level of 41.0 μA (top), and 53.2 μA (bottom).

observing the extent of tongue extrusion of the animal. The threshold level is found to be 41.0 μA at a rate of 0.635 kHz with 0.375 ms pulse duration.

As we increased the stimulation level, the tongue response became unnecessarily stronger. As it is hard to quantify the tongue behavior, we tried to correlate that with certain characteristics in chin EMG signals. Figure 4.1.2 shows the EMG signals measured using Embletta x100 (Natus Neurology Inc., USA) at the stimulation level of 41.0 μA (top) and 53.2 μA (bottom). The EMG signal with the lower stimulation level showed a series of one type of peak signals while two kinds of peaks are observed with the higher stimulation level. This second peak became a convenient mark for us to use as it indicates whether the stimulation level is excessive.

4.1.4. Weight and Size

The measured weight of the MENCE is 0.873 mN, with 0.275 mN of the weight from the magnets. The weight of the magnet accounts for 31.5 % of the total weight of the MENCE, which is a considerable amount which may be regarded as potentially putting additional pressure on the nerve on which it is installed. However, as demonstrated in 4.1.1, the influence of the increased amount of the weight on the nerve is negligible because the pressure of 20 mmHg, the pressure that evokes interference in the intraneural blood flow, is approximately 274 times higher than the increased amount. Thus, it is very unlikely that the weight of the MENCE will have any harmful effects on the nerve. On the other hand, the dimensions of the

MENCE may pose a problem under specific conditions. The dimension of the magnets is not an issue in this study, as the hypoglossal nerve is longer than the maximum length of the magnets and there is sufficient space to place the MENCE. However, in difficult conditions with greatly reduced space or tiny nerves, the magnets may be too bulky. In such case, smaller magnets will be necessary, thus necessitating a further research to find the minimum magnetic force to close the MENCE.

4.1.5. Cost Effectiveness

One of advantages of the MENCE is reusability when it comes to repeated acute experiments. With simple calculations of the costs of additional materials and the manufacturing process, it is estimated that the total fabrication cost of MENCE will be 63.3 % higher than that of an LCP-based conventional cuff electrode. The increase per unit is conspicuous, but we hold that the MENCE is more cost-effective with regard to repeated installations. Owing to its reusability, the expectation cost after several instances of installation of the MENCE will be lower than those of conventional electrodes which have low reinstallation rates due to their reliance on irreversible closing methods.

4.1.6. Extension to Multi-channels

Although only two electrodes are used for bipolar stimulation in this paper, our proposed closing method can be extended to multi-electrode cuff, such as the one developed by Schuettler et al. [89]. Their cuff included a dozen electrodes in

the polyimide cuff substrate, which is 1.5 mm in diameter and 40 mm long while the electrodes had a width of 500 μm and center-to-center spacing of 3.5 mm. We may simply use a long magnet in the cuff or we may construct the cuff with twelve single-channel cuffs each with a short magnet. In the latter construct, individual electrode of the cuff can be easily installed or removed by taking advantage of our proposed closing method.

4.2 Palatal Implant System for SPS

4.2.1. Reliability of Intra-Oral Device

The intra-oral device (IOD) is a device which is to be placed in the oral cavity. Though the device is encapsulated by silicone elastomer, there is a possibility for the device to fail due to penetration of saliva. Furthermore, heat generated from the power amplifier in the device may result in burn of oral mucosa. Therefore, an assessment was conducted to evaluate thermal and hygric reliability of the device and the setup of the assessment is shown in Figure 4.2.1**a**. The IOD was left in a convention oven for enough time until the temperature of the solution reaches 38 °C. Temperature of the solution near the device was measured at every 30 minutes, checking whether functions of the device were working well. Figure 4.2.1**b** shows the result. The IOD operated for 6 hours and the maximum increasement of temperature was 2.5 °C at the time of five hours from the start. After the five-hour, the temperature started to decrease and this seems to be due to

lowered power supply from the battery. From the result, the reliability of IOD on the head and moisture, was demonstrated.

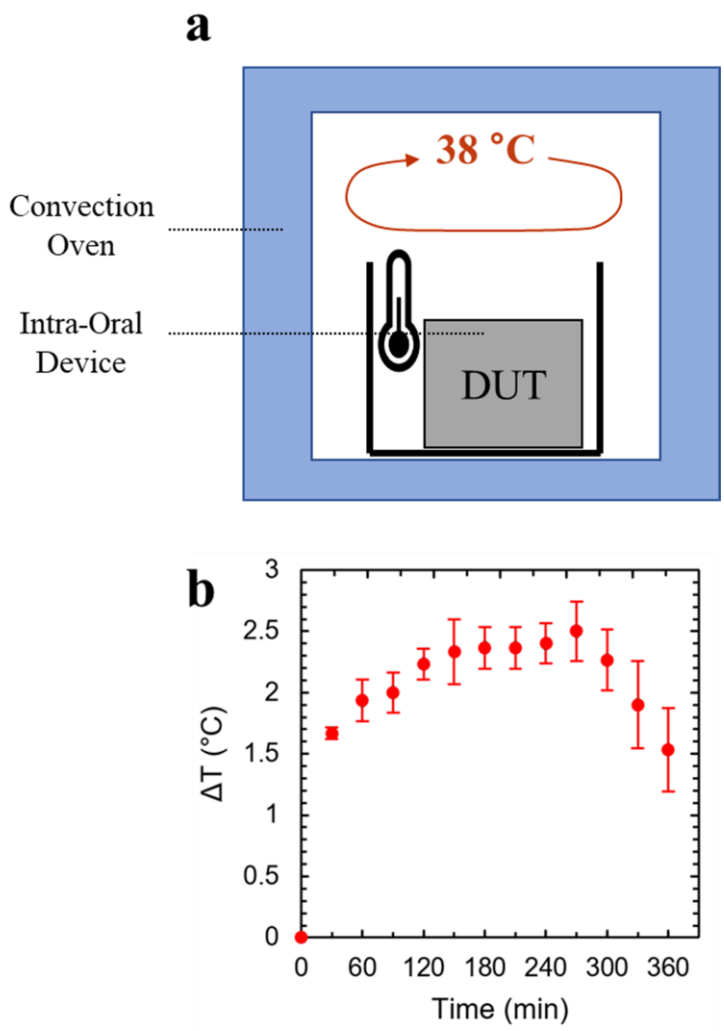

Figure 4.2.1 a, Test setup for assessing reliability of IOD on heat and moisture. The IOD was left in 38 °C for enough time. **b**, Temperature variance according to time. Temperature rise was measured after turn-on of the device, and rated peak change of 2.5 °C after 5 hours.

4.2.2. Palatoglossus Coupling

From the accumulated clinical experiments of the hypoglossal nerve stimulation, a retropalatal opening of OSA patients has been detected by researchers despite the fact that the hypoglossal nerve stimulation targets the retrolingual opening accomplished by contraction of genioglossus [54, 90]. The unique phenomenon, the palatoglossus coupling, can be explained with presence of the palatoglossus, which is the muscle that arises from the soft palate and extend to the sides of the tongue.

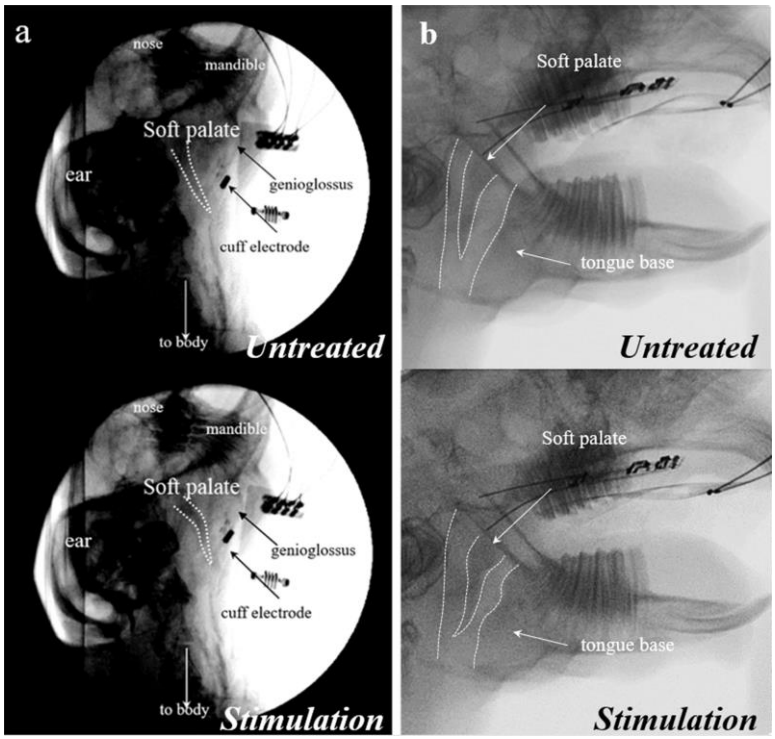

Figure 4.2.2 Palatoglossus coupling shown in *in vivo* assessments **a,** Contraction of soft palate during HNS (top: untreated, bottom: stimulated) **b,** Contraction of genioglossus during SPS

The couplings were observed through the experiments conducted in this thesis not only in the hypoglossal nerve stimulation but also, interestingly, in the soft palate stimulation. Figure 4.2.2**a** shows the effect of HNS on the soft palate. The clear contraction of the soft palate was observed with contraction of the genioglossus, simultaneously. On the other hand, contraction of the genioglossus was shown during the soft palate stimulation, as shown in Figure 4.2.2**b.** This supports that the soft palate and the genioglossus are crossly-linked together and shows possibility of multi-region opening through the upper-airway stimulation.

4.2.3. Potential Developments

4.2.3.1. Monolithic Packaging of Implant

The implant was fabricated on LCP substrates of which biocompatibility and long-term reliability have been repeatedly demonstrated in prior arts [91-96]. Yet, the implant was packaged by a silicone elastomer which is not suitable for long-term implantation due to its relatively high water absorption rate. Therefore, it is desirable to package the implant with a material with low water absorption rate and LCP can play such a role due to its nature of chemical inertness and extremely water absorption rate [58, 96]. Furthermore, an additional benefit of the LCP packaging comes from a monolithic package, which can prevent problems may otherwise occur due to seams at hetero-junctions. The LCP packaging method is well described in the reference and can be applied to the palatal implant, as shown in Figure 4.2.3 representing a mock-up of the suggested package [61].

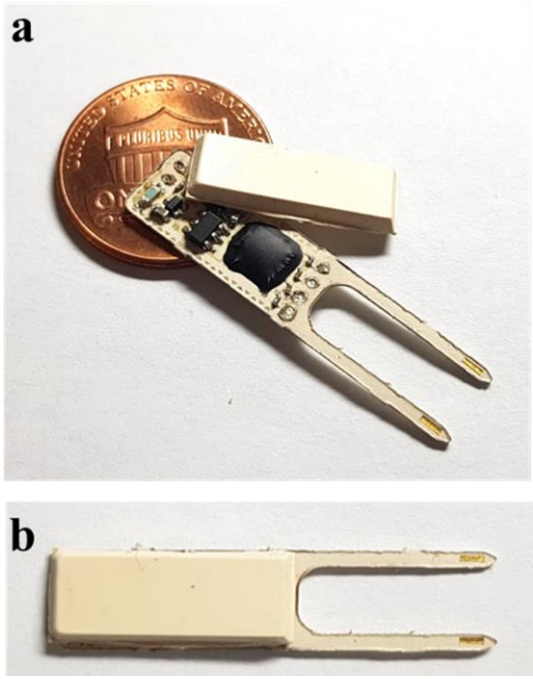

Figure 4.2.3 Suggested monolithic device packaged by LCP. **a,** Separated parts of the lid and the body, **b,** Mock-up of the integrated device.

4.2.3.2. Integration of sensors

The intra-oral device, shaped in a mouth-piece, can be synergetic if various sensors of temperature, pressure, and humidity are embedded for breath detection. With the acquired data, sleep patterns of OSA patients can be tracked and the data can be utilized for quantitative evaluation of sleep quality using an apnea-hypopnea (AHI) index. Furthermore, the signal synchronized to the breath pattern can contribute to constructing a closed-loop system of the palatal implant (Figure 4.2.4). By selectively stimulating the soft palate when apnea is detected, fatigue of the muscle as well as power consumption of the device can be decreased. A polymer pressure sensor made of PDMS and carbon nanotubes was fabricated to detect the

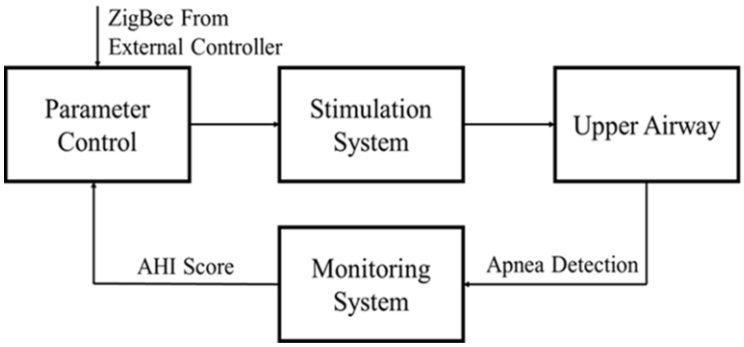

Figure 4.2.4 Suggested diagram of the closed-loop palatal implant system

oral pressure and a test result of breathing detection was represented in terms of changes of its diaphragm resistance [97]. The resistance change of the diaphragm was sensitive to small perturbations in air pressure and real time detection was available. With the accurate and sensitive breathing sensor, the palatal implant system can be more efficient and helpful device.

4.2.3.3. Application of Mandibular Advancement

A mandibular advancement device (MAD) is a treatment apparatus devised for retrolingual opening by advancing the mandible. Its efficacy has been reported to be under 50 % in a percentage reduction in AHI with high adherence, thereby suggested as an alternative to CPAP treatment [98-100]. Having a shape of an oral appliance, MAD can be applied to the intra-oral device of the palatal implant system, as illustrated in Figure 4.2.5. If the two devices are merged together, an improved therapeutic effect can be expected by opening both retropalatal and retroligual regions.

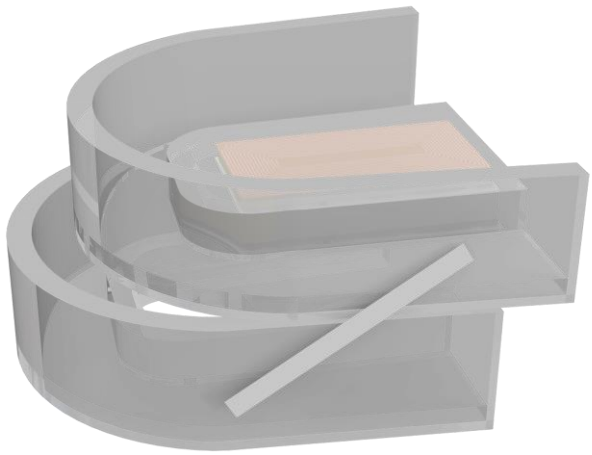

Figure 4.2.5 Suggested intra-oral device with mandibular advancement.

4.2.3.4. Improved ASIC Design for Palatal Implant

Application specific integrated circuit (ASIC) is essential to the implantable devices. The ASIC designed by K. S. Min (2014) successfully served as a biphasic current generator of the palatal implant. However, some points of the ASIC needed to be modified for an improved palatal implant.

First, the die size of the ASIC is 3.3 mm x 3.3 mm, which is quite large considering their land patterns and molding epoxies in a wire-bonding process. The large dimension is from unnecessarily many channels for this application and manual layouts of the digital circuit design. A small error margin of the PWM demodulation is also needed to be modified. The current demodulation depends on the number of rising pulses at DATA pin; 3− 7 for ‘0’, 8− 12 for ‘F’, and 13− 17 for ‘1’ while the others are considered as an error. However, existance of ‘F’ takes up unnecessary error margins, which may lead possibility of error in demoulation.

A new ASIC design is proposed to overcome the drawbacks of the existing ASIC in this section. The newly designed ASIC has a square dimension of 903.6 µm x 903.6 µm, while supporting eight output channels including a reference. The dimension could be minimized by reducing the number of channels and using a standard cell-based digital circuit design. Furthermore, a new protocol of the ASIC was designed without 'F' to increase error margins of '1' and '0'.

4.2.3.4.1. Circuit Design

The ASIC requires both power and data to generate a biphasic current pulse. The ASIC requires two power sources, one is VDDH (3.3 V) of a higher voltage level, and the other is VDD (1.8 V) of the lower voltage level. VDDH serves as a compliance voltage of the stimulation output while VDD is the supply for all other power-consuming components.

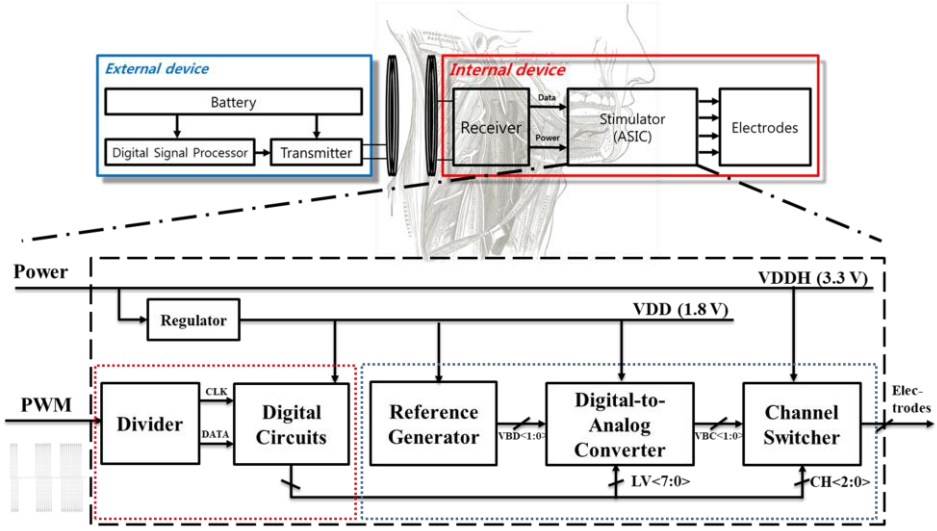

Figure 4.2.6 Block diagram of the designed ASIC. The demodulation part (red) and the pulse generator part (blue) are two major blocks of the chip.

First, in the demodulation part (red dotted region in Figure 4.2.6), the ASIC receives a PWM signal and regenerate a clock (CLK) and a train of data pulses (DATA) from the signal. Then the digital circuit demodulates the data and generates control signals that include information on level, frequency, duration, and channel selection.

In the pulse generator part (blue dotted region in Figure 4.2.6), there is a temperature-compensated reference current generator which is less sensitive to temperature variation, referencing a previous study [101]. The reference current is delivered to DAC through a current mirror. DAC multiplies the reference current based on the level control signal from the digital circuit. The determined current level is further delivered to a channel switcher consisting of H-bridges of which two channels are selected for a cathode and an anode, respectively.

4.2.3.4.2. Digital Protocol

Each bit comprising a word is determined by the number of received pulses in a PWM signal. Unlike the existing ASIC, the bit can be either ‘1’ or ‘0’, not F, the bit indicating end of the word. Rather, in this protocol, the end of each word is identified by counting the number of received pulses. By removing F, counting margins of the bit decision can be more flexibly determined. The number of pulses ranging from three to nine corresponds to a bit ‘1’, twelve to eighteen to ‘0’, and the others to an error. This is, duty cycles of PWM ranging over 15 %− 45 % corresponds to ‘1’, 60 %− 90 % to ‘0’.

Eleven bits constitute a word obeying the following protocol shown in

Table 4.2.1. The word has four modes; reset (RST), duration setting (DUR_SET), channel setting (CH_SET), and amplitude setting & stimulation (AM_SET_STIM) are those. To initialize the circuit, enough number of '0's over twelve should be provided in order to make sure that the circuit is under a reset state. When the first '1' is detected after the '0's, the circuit initialize a counter that counts the number of input bits to define end of the word. The second left-most bit determines the state to either setting modes (DUR_SET, CH_SET) or a stimulation mode. Duration and active channels of the stimulation output can be set in the setting modes. In the stimulation mode (AMP_SET_STIM), control signals switching transistors of the H-bridge are printed out according to the duration, active channel, and the amplitude information which is determined in the stimulation mode. Every word except RST has a parity bit at the right-most to check whether the word is in even-parity. By performing the parity check, the rate of erroneous demodulation can be

STATE	**[10]**	**[9]**	**[8]**	**[7]**	**[6]**	**[5]**	**[4]**	**[3]**	**[2]**	**[1]**
RST	0	0	0	0	0	0	0	0	0	0
DUR_SET	1	0	0	D[6]	D[5]	D[4]	D[3]	D[2]	D[1]	D[0]
CH_SET	1	0	1	Ch_a[2] X	Ch_a[1] X	Ch_a[0] X	Ch_c[2]	Ch_c[1]	Ch_c[0]	1(B) 0(M)
AMP_SET_STIM	1	1	A[7]	A[6]	A[5]	A[4]	A[3]	A[2]	A[1]	A[0]

Table 4.2.1 Designed protocol for broaden error margin of bit '1' and '0', by removing 'F'. Start and end of the frame is acknowledged by counting number of bits.

reduced.

4.2.3.4.3. Circuit Implementation

The brief illustration of the pulse generating circuit is depicted in the Figure 4.2.7. First, a reference generator creates a constant current level of 10 μA at 27 °C. The reference current is copied to the DAC in terms of bias voltages of the current mirror. The current is multiplied to eight branches each of which is controlled by digital signals. The ASIC is capable of generate the current amplitude from 10 μA to 2550 μA with 256 steps. The duration of the current is also controlled by the digital signals. The duration of the current pulse is ranging from 24 μs to 2028 μs with 128 linear steps of 16 μs, including a resting time of 8 μs. The pulse rate is determined by the rate of the rising edge of message signal, which is enable

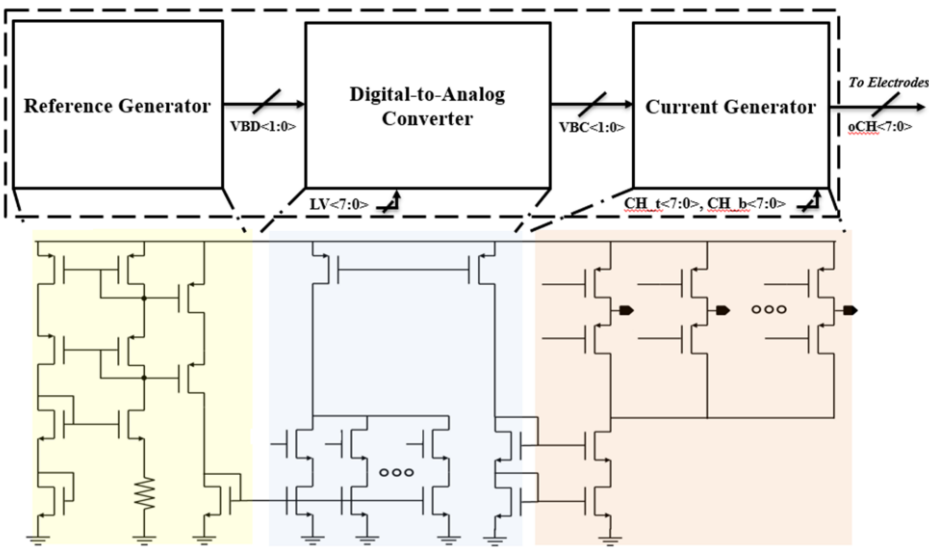

Figure 4.2.7 Pulse generating circuit of the designed ASIC. Temperature-compensated current generator is followed by DAC, and the current generator comprised of a series of H-bridges.

up to 125 kHz with the 2.5 MHz carrier frequency. The current amplitude is further mirrored to the current generator in terms of bias voltages. The current generator is supplied by VDDH, the high-voltage supply which serves as a compliance voltage of the current pulse. A series of the H-bridges are tied up to the current sink which is mirrored from the DAC. Therefore, the current output having parameters of the desired amplitude, duration, and frequency is generated through the desired channels. The integrated analog and digital circuit layout is shown in Figure 4.2.8. The die size of the chip was 0.90 x 0.90 square, with 0.30 x 0.28 rectangle digital core. The designed size is significantly small compared to the previous ASIC chip having dimension of 3.3 mm x 3.3 mm, 53.3 % reduction in the die size.

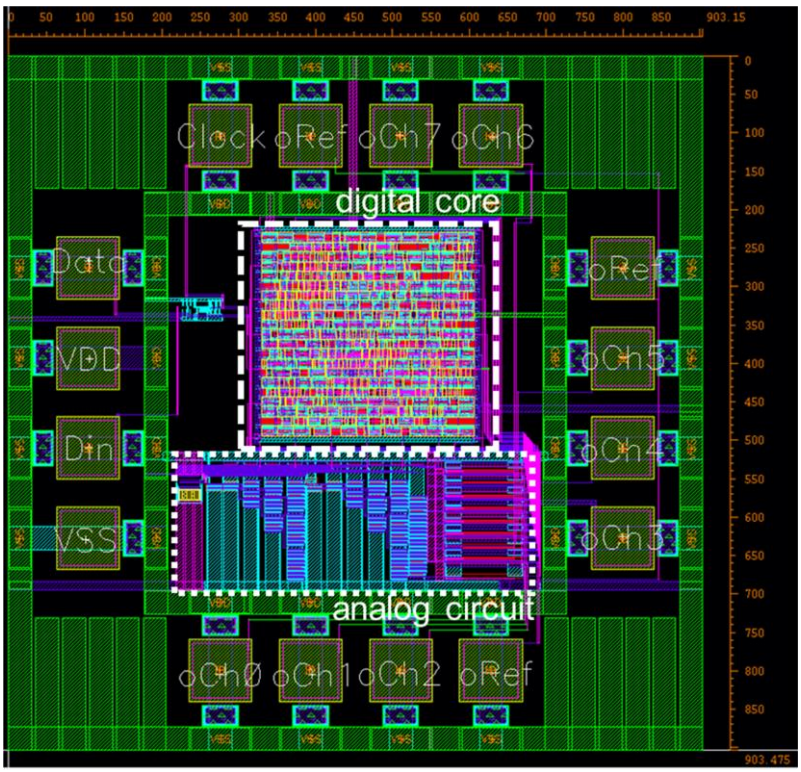

Figure 4.2.8 Designed chip layout with dimension of 0.9 mm x 0.9 mm including pads.

Chapter 5

Conclusion

In this thesis, neural prostheses were suggested as novel approaches to treat obstructive sleep apnea. Two prosthetic devices were designed, developed, and demonstrated for tongue-related and palate-related patient by opening the retrolingual and the retropalatal region, respectively.

First, as a method for retrolingual opening, a magnetic cuff system for hypoglossal nerve stimulation was designed and fabricated. The cuff electrode featuring magnetic closure provides repeated and reliable reinstallation, which is a very helpful feature to identify a correct nerve. A pair of rare-earth magnets were embedded in a liquid crystal polymer (LCP) substrate of which water absorption rate is very low compared to other implantable polymers such as polyimide, parylene-C, and PDMS. Thin gold layer (10 μm) was patterned on the LCP substrate using a series of semiconductor processes. Seed layers of Ti and Au were deposited on the LCP using an E-gun evaporator and then electroplated and etched for patterning the metal layer. Further thermal lamination and laser machining processes were performed to embed magnets and complete the fabrication. The fabricated electrode had its electrode site area of 3.5 mm x 1.6 mm with substrate thickness of 50 μm.

The fabricated cuff electrodes were evaluated both *in vivo* and *in vitro* to demonstrate its feasibility to the hypoglossal nerve stimulation. As *in vitro* evaluations, an electrochemical impedance spectroscopy (EIS) and cyclic voltammetry (CV) were conducted using three-electrode system in a phosphate buffer solution (PBS). From the EIS result, a magnitude of the impedance of the electrode at 1 kHz was 638 Ω with a phase angle of -67.8 °, which is several tens

times lower than conventional microelectrodes due to its large surface area. Cathodic charge storage capacity (CSC_c) was calculated from the CV plot and to be 1.69 mC/cm^2, which is large enough value compared to the required amount of charge for our stimulation, 7.68 nC. A seven-month-old New Zealand white rabbit was used as a subject of the *in vivo* evaluation. The cuff electrode was installed on the hypoglossal nerve of the rabbit and percutaneously connected to an external pulse generator. The stimulation current pulse had a parameter of 41.0 μA amplitude, 635 Hz pulse rate, and 375 μs duration. Snapshots of the upper airway of the subject were obtained using a C-arm fluoroscopy at both presence and absence of the stimulation. Protrusion of the tongue could be observed with bare eyes during the stimulation, synchronized to the applied pulse. Contraction of the genioglossus was also observed via the C-ram fluoroscopy snapshots.

A novel palatal implant system was proposed for the retropalatal opening. The system consists of an implant that delivers current pulse to the soft palate and an intra-oral device (IOD) that transmits power and data to the implant via an inductive link. In the implant, a multi-layered LCP laminate, encapsulated by PDMS, includes coil, electrode, and circuit layers in it, generating and delivering a biphasic current pulse for soft palate stimulation. The circuit regenerates power and data for the pulse generator ASIC by rectifying and demodulating received RF signal which is transmitted from the IOD. The RF signal is generated by a class-E amplifier in the IOD with attached ASK modulator which inputs data signal received via a ZigBee receiver. All the components of the IOD including a battery, are stacked into a 30 mm x 15 mm x 10 mm cuboid which is placed in the cavity of

an oral appliance.

Evaluations on the inductive link were performed to measure the power transmission and the reliability of the data telemetry. Received peak-to-peak voltage was 10 V and total power efficiency was 12.4 % at the telemetry distance of 5 mm. Duty-cycle error of demodulated PWM were measured at the distance of 2− 8 mm and the errors were all allowable within the error margin of 10 %.

In vitro Evaluations were conducted to measure and compare electrochemical impedance spectrum and cathodic charge storage capacity of Au and EIROF (electrodeposited iridium oxide film) electrode. The magnitudes of the impedance and CSC_c of EIROF were significantly lower than those of Au by a degree of hundreds. Voltage transient was also measured to ensure a safe stimulation and the charge injection capacity of EIROF did not exceed under 0.16 mC/cm^2, which is far less amount of charge to our stimulation parameter.

To demonstrate a feasibility of the system for soft palate stimulation, *in vivo* test was conducted using a rabbit. The implant was implanted into the palate of the rabbit and received power and data from a transmitter coil through the palatal skin. Biphasic current pulse, having a parameter set of 1.00 mA amplitude, 100 Hz pulse rate, and 540 μs duration, was applied to the soft palate. As a result of the stimulation, contractions of the palatoglossus muscle as well as the soft palate could be observed via a C-arm fluoroscopy.

In the discussion, possible developments of the palatal implant system were proposed such as sensor integration and an application of a mandibular advancement device. Finally, a design of mixed-signal ASIC chip for minimized

die-size and improved communication protocol was suggested.

Sleep apnea is becoming a prevalent disorder in the modern society. Still, there are patients who do not benefit from the existing therapies. Upper airway stimulation can play an important role for treating OSA considering that the airway patency is closely related to activation of pharyngeal muscles. We hope that the research conducted in this thesis to become a steppingstone for developing a break-through therapy that helps patients who suffer from OSA.

References

[1] P. E. Peppard, T. Young, J. H. Barnet, M. Palta, E. W. Hagen, and K. M. J. A. j. o. e. Hla, "Increased prevalence of sleep-disordered breathing in adults," vol. 177, no. 9, pp. 1006-1014, 2013.

[2] J.-D. L. Lattimore, D. S. Celermajer, and I. Wilcox, "Obstructive sleep apnea and cardiovascular disease," *Journal of the American College of Cardiology,* vol. 41, no. 9, pp. 1429-1437, 2003.

[3] M. F. Pengo and J. Steier, "Emerging technology: electrical stimulation in obstructive sleep apnoea," *Journal of thoracic disease,* vol. 7, no. 8, p. 1286, 2015.

[4] K. Sutherland, C. Phillips, and P. J. J. o. D. S. M. Cistulli, "Efficacy versus effectiveness in the treatment of obstructive sleep apnea: CPAP and oral appliances," vol. 2, no. 4, pp. 175-181, 2015.

[5] N. B. Kribbs *et al.*, "Objective measurement of patterns of nasal CPAP use by patients with obstructive sleep apnea," vol. 147, no. 4, pp. 887-895, 1993.

[6] D. Bartlett *et al.*, "Increasing adherence to obstructive sleep apnea treatment with a group social cognitive therapy treatment intervention: a randomized trial," vol. 36, no. 11, pp. 1647-1654, 2013.

[7] T. E. Weaver, A. J. O. Sawyer, and M. S. Clinics, "Management of obstructive sleep apnea by continuous positive airway pressure," vol. 21, no. 4, pp. 403-412, 2009.

[8] S. M. Caples *et al.*, "Surgical modifications of the upper airway for obstructive sleep apnea in adults: a systematic review and meta-analysis," vol. 33, no. 10, pp. 1396-1407, 2010.

[9] M. B. Blumen, I. Buchet, P. Meulien, C. Hausser Hauw, H. Neveu, and F. Chabolle, "Complications/adverse effects of maxillomandibular advancement for the treatment of OSA in regard to outcome," *Otolaryngology-Head and Neck Surgery,* vol. 141, no. 5, pp. 591-597, 2009.

[10] K. Sutherland, C. Phillips, and P. J. J. D. S. M. Cistulli, "Efficacy versus effectiveness in the treatment of obstructive sleep apnea: CPAP and oral appliances," vol. 2, no. 4, pp. 175-181, 2015.

[11] C. L. Phillips *et al.*, "Health outcomes of continuous positive airway pressure versus oral appliance treatment for obstructive sleep apnea: a randomized controlled trial," vol. 187, no. 8, pp. 879-887, 2013.

[12] A. Labra, A.-D. Huerta-Delgado, C. Gutierrez-Sanchez, S.-A. Cordero-Chacon, P. J. J. o. O.-.-H. Basurto-Madero, and N. Surgery, "Uvulopalatopharyngoplasty and uvulopalatal flap for the treatment of snoring: technique to avoid complications," vol. 37, no. 2, 2008.

[13] E. J. Kezirian *et al.*, "Incidence of serious complications after uvulopalatopharyngoplasty," vol. 114, no. 3, pp. 450-453, 2004.

[14] R. M. Esclamado, M. G. Glenn, T. M. Mcculloch, and C. W. J. T. L. Cummings, "Perioperative complications and risk factors in the surgical treatment of obstructive sleep apnea syndrome," vol. 99, no. 11, pp. 1125-1129, 1989.

[15] J. D. Harmon, W. Morgan, and B. J. S. m. j. Chaudhary, "Sleep apnea: morbidity and mortality of surgical treatment," vol. 82, no. 2, pp. 161-164, 1989.

[16] R. W. Riley *et al.*, "Obstructive sleep apnea surgery: risk management and complications," vol. 117, no. 6, pp. 648-652, 1997.

[17] K. A. Ferguson, K. Heighway, R. R. J. A. j. o. r. Ruby, and c. c. medicine, "A randomized trial of laser-assisted uvulopalatoplasty in the treatment of mild obstructive sleep apnea," vol. 167, no. 1, pp. 15-19, 2003.
[18] F. Larrosa, L. Hernandez, A. Morello, E. Ballester, L. Quinto, and J. J. E. R. J. Montserrat, "Laser-assisted uvulopalatoplasty for snoring: does it meet the expectations?," vol. 24, no. 1, pp. 66-70, 2004.
[19] R. P. Walker and C. J. T. L. Gopalsami, "Laser□assisted uvulopalatoplasty: postoperative complications," vol. 106, no. 7, pp. 834-838, 1996.
[20] C. Carenfelt and P. J. T. L. Haraldsson, "Frequency of complications after uvulopalatopharyngoplasty," vol. 341, no. 8842, p. 437, 1993.
[21] G. Berger, G. Stein, D. Ophir, Y. J. A. o. O. H. Finkelstein, and N. Surgery, "Is there a better way to do laser-assisted uvulopalatoplasty?," vol. 129, no. 4, pp. 447-453, 2003.
[22] V. Pavelec and P. J. T. L. Polenik, "Use of Er, Cr: YSGG versus standard lasers in laser assisted uvulopalatoplasty for treatment of snoring," vol. 116, no. 8, pp. 1512-1516, 2006.
[23] A. Khan, K. Ramar, S. Maddirala, O. Friedman, J. F. Pallanch, and E. J. Olson, "Uvulopalatopharyngoplasty in the management of obstructive sleep apnea: the mayo clinic experience," in *Mayo Clinic Proceedings*, 2009, vol. 84, no. 9, pp. 795-800: Elsevier.
[24] K. A. Franklin *et al.*, "Effects and side-effects of surgery for snoring and obstructive sleep apnea—a systematic review," vol. 32, no. 1, pp. 27-36, 2009.
[25] W.-k. Ho, W. I. Wei, K.-f. J. A. o. O. H. Chung, and N. Surgery, "Managing disturbing snoring with palatal implants: a pilot study," vol. 130, no. 6, pp. 753-758, 2004.
[26] S. Nordgård, K. Wormdal, V. Bugten, B. K. Stene, and K. W. J. A. o.-l. Skjøstad, "Palatal implants: a new method for the treatment of snoring," vol. 124, no. 8, pp. 970-975, 2004.
[27] M. B. Gillespie, J. E. Smith, J. Clarke, S. A. J. O. H. Nguyen, and N. Surgery, "Effectiveness of Pillar palatal implants for snoring management," vol. 140, no. 3, pp. 363-368, 2009.
[28] M. Friedman, P. Schalch, and N. J. J. T. L. Joseph, "Palatal stiffening after failed uvulopalatopharyngoplasty with the Pillar Implant System," vol. 116, no. 11, pp. 1956-1961, 2006.
[29] E. A. Server, Z. Alkan, O. Yigit, and A. G. Yasak, "Long-term results of pillar implant procedure," *Kulak Burun Bogaz Ihtis Derg,* vol. 26, no. 5, pp. 258-64, Sep-Oct 2016.
[30] M. A. Svirsky, A. M. Robbins, K. I. Kirk, D. B. Pisoni, and R. T. J. P. s. Miyamoto, "Language development in profoundly deaf children with cochlear implants," vol. 11, no. 2, pp. 153-158, 2000.
[31] W. F. J. A. o. O. House, Rhinology and Laryngology, "Cochlear implants," vol. 85, no. 3_suppl, pp. 3-3, 1976.
[32] G. Clark, "Cochlear implants," in *Speech processing in the auditory system*: Springer, 2004, pp. 422-462.
[33] B. S. Wilson, C. C. Finley, D. T. Lawson, R. D. Wolford, D. K. Eddington, and W. M. J. N. Rabinowitz, "Better speech recognition with cochlear implants," vol. 352, no. 6332, p. 236, 1991.
[34] J. F. J. J. o. N.-o. Rizzo III, "Update on retinal prosthetic research: the Boston Retinal Implant Project," vol. 31, no. 2, pp. 160-168, 2011.
[35] V. Chow and A. Y. Chow, "Multi-phasic microphotodiode retinal implant and

adaptive imaging retinal stimulation system," ed: Google Patents, 1999.
[36] E. J. S. Zrenner, "Will retinal implants restore vision?," vol. 295, no. 5557, pp. 1022-1025, 2002.
[37] P. H. Van de Heyning *et al.*, "Implanted upper airway stimulation device for obstructive sleep apnea," vol. 122, no. 7, pp. 1626-1633, 2012.
[38] P. J. Strollo Jr *et al.*, "Upper-airway stimulation for obstructive sleep apnea," vol. 370, no. 2, pp. 139-149, 2014.
[39] J. S. Perlmutter and J. W. J. A. R. N. Mink, "Deep brain stimulation," vol. 29, pp. 229-257, 2006.
[40] G. Deuschl *et al.*, "A randomized trial of deep-brain stimulation for Parkinson's disease," vol. 355, no. 9, pp. 896-908, 2006.
[41] H. S. Mayberg *et al.*, "Deep brain stimulation for treatment-resistant depression," vol. 45, no. 5, pp. 651-660, 2005.
[42] S. Robin, M. Sawan, J. Harvey, M. Abdel-Gawad, T. Abdel-Baky, and M. Elhilai, "A new implantable microstimulator dedicated to selective stimulation of the bladder," in *Proceedings of the 19th Annual International Conference of the IEEE Engineering in Medicine and Biology Society.'Magnificent Milestones and Emerging Opportunities in Medical Engineering'(Cat. No. 97CH36136)*, 1997, vol. 4, pp. 1792-1795: IEEE.
[43] D. W. Eisele, A. R. Schwartz, and P. L. Smith, "Tongue neuromuscular and direct hypoglossal nerve stimulation for obstructive sleep apnea," *Otolaryngologic clinics of North America,* vol. 36, no. 3, pp. 501-510, 2003.
[44] M. W. Keith, P. H. PEckHAM, G. B. Thrope, J. R. Buckett, K. C. Stroh, and V. Menger, "Functional neuromuscular stimulation neuroprostheses for the tetraplegic hand," *Clinical orthopaedics and related research,* no. 233, pp. 25-33, 1988.
[45] H. Chizek, R. Kobetic, E. Marsolais, J. Abbas, I. Donner, and E. Simon, "Control of functional neuromuscular stimulation systems for standing and locomotion in paraplegics," *Proceedings of the IEEE,* vol. 76, no. 9, pp. 1155-1165, 1988.
[46] G. Yarkony, R. Jaeger, E. Roth, A. Kralj, and J. Quintern, "Functional neuromuscular stimulation for standing after spinal cord injury," *Archives of physical medicine and rehabilitation,* vol. 71, no. 3, pp. 201-206, 1990.
[47] L. R. Sheffler and J. Chae, "Neuromuscular electrical stimulation in neurorehabilitation," *Muscle & Nerve: Official Journal of the American Association of Electrodiagnostic Medicine,* vol. 35, no. 5, pp. 562-590, 2007.
[48] R. G. Lee and P. van Donkelaar, "Mechanisms underlying functional recovery following stroke," *Canadian Journal of neurological sciences,* vol. 22, no. 4, pp. 257-263, 1995.
[49] R. T. Brouillette and B. T. J. J. o. A. P. Thach, "Control of genioglossus muscle inspiratory activity," vol. 49, no. 5, pp. 801-808, 1980.
[50] M. J. Decker, J. Haaga, J. L. Arnold, D. Atzberger, and K. P. J. J. o. A. P. Strohl, "Functional electrical stimulation and respiration during sleep," vol. 75, no. 3, pp. 1053-1061, 1993.
[51] D. W. Fairbanks, D. J. E. Fairbanks, nose,, and t. journal, "Neurostimulation for obstructive sleep apnea: investigations," vol. 72, no. 1, pp. 52-4, 57, 1993.
[52] A. R. Schwartz *et al.*, "Therapeutic electrical stimulation of the hypoglossal nerve in obstructive sleep apnea," vol. 127, no. 10, pp. 1216-1223, 2001.
[53] E. J. Kezirian *et al.*, "Electrical stimulation of the hypoglossal nerve in the treatment of obstructive sleep apnea," vol. 14, no. 5, pp. 299-305, 2010.
[54] C. Heiser, G. Edenharter, M. Bas, M. Wirth, and B. J. T. L. Hofauer, "Palatoglossus

coupling in selective upper airway stimulation," vol. 127, no. 10, pp. E378-E383, 2017.
[55] A. S. Jordan, D. P. J. R. p. White, and neurobiology, "Pharyngeal motor control and the pathogenesis of obstructive sleep apnea," vol. 160, no. 1, pp. 1-7, 2008.
[56] R. S. Schwartz, N. N. Salome, P. T. Ingmundon, and J. D. J. T. J. o. p. d. Rugh, "Effects of electrical stimulation to the soft palate on snoring and obstructive sleep apnea," vol. 76, no. 3, pp. 273-281, 1996.
[57] A. J. McWhorter, J. A. Rowley, D. W. Eisele, P. L. Smith, A. R. J. A. o. O. H. Schwartz, and N. Surgery, "The effect of tensor veli palatini stimulation on upper airway patency," vol. 125, no. 9, pp. 937-940, 1999.
[58] T. M. Gwon, C. Kim, S. Shin, J. H. Park, J. H. Kim, and S. J. Kim, "Liquid crystal polymer (LCP)-based neural prosthetic devices," *Biomedical Engineering Letters,* vol. 6, no. 3, pp. 148-163, 2016.
[59] T. M. Gwon *et al.*, "Fabrication and evaluation of an improved polymer-based cochlear electrode array for atraumatic insertion," *Biomedical microdevices,* vol. 17, no. 2, p. 32, 2015.
[60] J. Jeong, S. W. Lee, K. S. Min, S. Shin, S. B. Jun, and S. J. Kim, "Liquid Crystal Polymer(LCP), an Attractive Substrate for Retinal Implant," *Sensors and Materials,* vol. 24, no. 4, pp. 189-203, 2012.
[61] J. Jeong, S. H. Bae, K. S. Min, J.-M. Seo, H. Chung, and S. J. Kim, "A miniaturized, eye-conformable, and long-term reliable retinal prosthesis using monolithic fabrication of liquid crystal polymer (LCP)," *IEEE Transactions on Biomedical Engineering,* vol. 62, no. 3, pp. 982--989, 2015.
[62] S. E. Lee *et al.*, "A flexible depth probe using liquid crystal polymer," vol. 59, no. 7, pp. 2085-2094, 2012.
[63] S. Shim, H.-Y. Park, G. J. Choi, H.-C. Shin, and S. J. J. A. O. Kim, "A Simply Fabricated Neural Probe by Laser Machining of a Thermally Laminated Gold Thin Film on Transparent Cyclic Olefin Polymer," vol. 4, no. 2, pp. 2590-2595, 2019.
[64] Kuraray. (2012). *Kuraray LCP Film*. Available: https://www.kuraray.eu/fileadmin/presse/publikationen/downloads_k_fair_2013/New_business_development_division/Kuraray_LCP_Film_Brochure.pdf
[65] W. B. Van de Graaff, S. B. Gottfried, J. Mitra, E. van Lunteren, N. S. Cherniack, and K. P. J. J. o. A. P. Strohl, "Respiratory function of hyoid muscles and hyoid arch," vol. 57, no. 1, pp. 197-204, 1984.
[66] L. Mu and I. J. C. A. Sanders, "Human tongue neuroanatomy: nerve supply and motor endplates," vol. 23, no. 7, pp. 777-791, 2010.
[67] C. Heiser, B. Hofauer, L. Lozier, B. T. Woodson, and T. J. T. L. Stark, "Nerve monitoring–guided selective hypoglossal nerve stimulation in obstructive sleep apnea patients," vol. 126, no. 12, pp. 2852-2858, 2016.
[68] G. G. Naples, J. T. Mortimer, A. Scheiner, and J. D. J. I. t. o. b. e. Sweeney, "A spiral nerve cuff electrode for peripheral nerve stimulation," vol. 35, no. 11, pp. 905-916, 1988.
[69] M. K. Haugland, J. A. Hoffer, and T. J. I. T. o. R. E. Sinkjaer, "Skin contact force information in sensory nerve signals recorded by implanted cuff electrodes," vol. 2, no. 1, pp. 18-28, 1994.
[70] F. J. Rodri *et al.*, "Polyimide cuff electrodes for peripheral nerve stimulation," vol. 98, no. 2, pp. 105-118, 2000.
[71] M. Crampon, V. Brailovski, M. Sawan, and F. Trochu, "Nerve cuff electrode with shape memory alloy armature: design and fabrication," *Bio-medical materials and engineering,* vol. 12, no. 4, pp. 397-410, 2001.

[72] M. A. Crampon, M. Sawan, V. Brailovski, and F. Trochu, "New easy to install nerve cuff electrode using shape memory alloy armature," *Artificial organs,* vol. 23, no. 5, pp. 392-395, 1999.
[73] X. Kang, J.-Q. Liu, H. Tian, B. Yang, Y. Nuli, and C. Yang, "Self-Closed Parylene Cuff Electrode for Peripheral Nerve Recording," *Microelectromechanical Systems, Journal of,* vol. 24, no. 2, pp. 319-332, 2015.
[74] E. Romero, J.-F. Denef, J. Delbeke, A. Robert, and C. Veraart, "Neural morphological effects of long-term implantation of the self-sizing spiral cuff nerve electrode," *Medical and Biological Engineering and Computing,* vol. 39, no. 1, pp. 90-100, 2001.
[75] G. G. Naples, J. T. Mortimer, A. Scheiner, and J. D. Sweeney, "A spiral nerve cuff electrode for peripheral nerve stimulation," *Biomedical Engineering, IEEE Transactions on,* vol. 35, no. 11, pp. 905-916, 1988.
[76] F. J. Rodri *et al.*, "Polyimide cuff electrodes for peripheral nerve stimulation," *Journal of neuroscience methods,* vol. 98, no. 2, pp. 105-118, 2000.
[77] A. J. Bard and L. R. Faulkner, *Electrochemical methods: Fundamentals and Applications* 2nd ed. New York: Wiley, 2001.
[78] K. S. Min, S. H. Oh, M.-H. Park, J. Jeong, S. J. J. O. Kim, and Neurotology, "A polymer-based multichannel cochlear electrode array," vol. 35, no. 7, pp. 1179-1186, 2014.
[79] S. Shin *et al.*, "High charge storage capacity electrodeposited iridium oxide film on liquid crystal polymer-based neural electrodes," vol. 28, no. 3, pp. 243-60, 2016.
[80] N. O. J. Q. Sokal, "Class-E RF power amplifiers," vol. 204, no. 1, pp. 9-20, 2001.
[81] R. R. Harrison, "Designing efficient inductive power links for implantable devices," in *2007 IEEE International Symposium on Circuits and Systems*, 2007, pp. 2080-2083: IEEE.
[82] P. Vaillancourt, A. Djemouai, J. Harvey, and M. Sawan, "EM radiation behavior upon biological tissues in a radio-frequency power transfer link for a cortical visual implant," in *Proceedings of the 19th Annual International Conference of the IEEE Engineering in Medicine and Biology Society.'Magnificent Milestones and Emerging Opportunities in Medical Engineering'(Cat. No. 97CH36136)*, 1997, vol. 6, pp. 2499-2502: IEEE.
[83] S. S. Mohan, M. del Mar Hershenson, S. P. Boyd, and T. H. J. I. J. o. s.-s. c. Lee, "Simple accurate expressions for planar spiral inductances," vol. 34, no. 10, pp. 1419-1424, 1999.
[84] S. F. J. A. R. B. E. Cogan, "Neural stimulation and recording electrodes," vol. 10, pp. 275-309, 2008.
[85] J. Seo *et al.*, "Wireless navigation of pigeons using polymer-based fully implantable stimulator: A pilot study using depth electrodes," in *2017 39th Annual International Conference of the IEEE Engineering in Medicine and Biology Society (EMBC)*, 2017, pp. 917-920: IEEE.
[86] R. T. Leung, M. N. Shivdasani, D. A. Nayagam, and R. K. J. I. T. o. B. E. Shepherd, "In VivoandIn VitroComparison of the Charge Injection Capacity of Platinum Macroelectrodes," vol. 62, no. 3, pp. 849-857, 2014.
[87] S. F. Cogan, "Neural stimulation and recording electrodes," *Annu. Rev. Biomed. Eng.,* vol. 10, pp. 275-309, 2008.
[88] S. F. Cogan, T. Plante, and J. Ehrlich, "Sputtered iridium oxide films (SIROFs) for low-impedance neural stimulation and recording electrodes," in *The 26th Annual International Conference of the IEEE Engineering in Medicine and Biology Society*, 2004, vol. 2, pp. 4153-4156: IEEE.

[89] M. Schuettler, N. Donaldson, V. Seetohul, and J. Taylor, "Fibre-selective recording from the peripheral nerves of frogs using a multi-electrode cuff," *Journal of neural engineering,* vol. 10, no. 3, p. 036016, 2013.

[90] F. Safiruddin *et al.*, "Effect of upper-airway stimulation for obstructive sleep apnoea on airway dimensions," *European Respiratory Journal,* vol. 45, no. 1, pp. 129-138, 2015.

[91] K. Aihara, M. J. Chen, C. Chen, and A.-V. H. Pham, "Reliability of liquid crystal polymer air cavity packaging," *IEEE Transactions on Components, Packaging and Manufacturing Technology,* vol. 2, no. 2, pp. 224-230, 2012.

[92] V. Sundaram *et al.*, "High density electrical interconnections in liquid crystal polymer (LCP) substrates for retinal and neural prosthesis applications," in *2011 IEEE 61st Electronic Components and Technology Conference (ECTC)*, 2011, pp. 1308-1313: IEEE.

[93] G.-T. Hwang *et al.*, "In vivo silicon-based flexible radio frequency integrated circuits monolithically encapsulated with biocompatible liquid crystal polymers," *Acs Nano,* vol. 7, no. 5, pp. 4545-4553, 2013.

[94] T. M. Gwon, J. H. Kim, G. J. Choi, and S. J. Kim, "Mechanical interlocking to improve metal–polymer adhesion in polymer-based neural electrodes and its impact on device reliability," *Journal of materials science,* vol. 51, no. 14, pp. 6897-6912, 2016.

[95] S. W. Lee, K. S. Min, J. Jeong, J. Kim, and S. J. Kim, "Monolithic encapsulation of implantable neuroprosthetic devices using liquid crystal polymers," *IEEE Transactions on Biomedical Engineering,* vol. 58, no. 8, pp. 2255-2263, 2011.

[96] J. Jeong, S. H. Bae, J.-M. Seo, H. Chung, and S. J. Kim, "Long-term evaluation of a liquid crystal polymer (LCP)-based retinal prosthesis," *Journal of neural engineering,* vol. 13, no. 2, p. 025004, 2016.

[97] S. J. K. Tallis H. da Costa, Jeong-Whun Kim, Jungmin Seo, Jin-Woo Choi, "Breathing Detection Using a Polymer Pressure Sensor," presented at the SMIT-IBEC 2018, Seoul, Korea, November, 2018.

[98] E. C. Brown, S. Cheng, D. K. McKenzie, J. E. Butler, S. C. Gandevia, and L. E. J. S. Bilston, "Respiratory movement of upper airway tissue in obstructive sleep apnea," vol. 36, no. 7, pp. 1069-1076, 2013.

[99] A. S. Chan *et al.*, "The effect of mandibular advancement on upper airway structure in obstructive sleep apnoea," vol. 65, no. 8, pp. 726-732, 2010.

[100] J. Cobo, F. de Carlos, and A. Suarez, "Mandibular advancement device (MAD®) to treat sleet apnoea-hypopnoea syndrome and chronic snoring," in *25th Southern Biomedical Engineering Conference 2009, 15–17 May 2009, Miami, Florida, USA*, 2009, pp. 349-354: Springer.

[101] F. Fiori, P. S. J. I. T. o. C. Crovetti, and S. I. E. Briefs, "A new compact temperature-compensated CMOS current reference," vol. 52, no. 11, pp. 724-728, 2005.

국문초록

수면 무호흡은 북미 남성의 13% 그리고 여성의 6%가 겪고 있을 정도로 유병률이 높은 질병이다. 단순히 밤에 불편한 것 정도로 생각될 수 있지만, 수면 무호흡은 인슐린 저항성, 심혈관 질환, 그리고 과도한 졸림으로 인한 삶의 질 저하와 같은 심각한 후유증을 유발할 수 있다. 양압기도법 (CPAP), 구강 장치, 외과적 수술과 같은 기존의 치료법들은 낮은 효과, 낮은 순응도, 또는 높은 침습성 때문에 일부 환자들에게는 적용이 불가능한 점이 있다. 따라서, 이러한 기존 치료법들의 한계점을 극복하기 위해서는 혁신적인 치료법을 개발할 필요가 있다.

본 학위 논문에서는 수면 무호흡을 치료하기 위한 새로운 접근법으로써 두개의 삽입형 전자 장치를 제안한다. 이 장치들은 인두 폐쇄의 주된 원인인 설 기저부 및 연구개 기저부의 개방성을 확보하기 위한 특별한 방법을 제공한다. 먼저, 혀의 외부 근육을 연결하는 설하 신경을 자극하기 위해 마그네틱 커프 시스템을 디자인하고 제작하였다. 이 시스템은 자석이 내장된 신경 커프 전극과 자극 펄스 생성기로 이루어져 있다. 전극에 사용된 기판 물질은 액정 폴리머인데 생체 호환적이며 유연하고 뛰어난 밀봉성을 특징으로 한다. 전극에 내장된 희토류 자석의 자기력 덕분에 전극을 신경에 쉽게 설치하거나 떼어낼 수 있다. 제작된 전극의 설하 신경 자극에의 실행 가능성을 검증하기 위해, 실험관 내 실험 및 생체 내 실험이 수행되었다. 1 Hz 에서 100 kHz에 이르는 주파수에서 임피던스의 크기와 위상을 알아내기 위해, PBS 용액에 설치된 삼전극 시스템에서 전기화학적 임피던스 스펙트럼을 측정하였다. 또한, 토끼의 설하신경을 자극하기 위해 생체 내 실험이 수행되었다. 자극이 인가되는 동안, 이설근의 수축을 C-arm fluoroscopy 장치

를 통해 확인할 수 있었으며 및 맨 눈으로도 혀의 돌출을 확인할 수 있었다.

전기 자극이 연구개 수축을 유발한다는 가정 하에서, 전기 자극이 연구개 기저부 개방성에 미치는 효과를 알아보기 위해 사전 실험이 수행되었다. 이 실험을 통하여, 1.10 mA의 진폭, 636.3 μs의 지속 시간, 100 Hz의 주파수를 가진 전류 자극이 연구개의 위치를 상승시킨다는 것을 C-arm fluoroscopy를 통하여 확인할 수 있었다.

위의 발견을 기반으로 하여, 구개 임플란트 시스템이 디자인되고 제작되었다. 이 시스템은 외부 컨트롤러로부터 지그비 통신을 통해 자극 파라미터를 수신하는 구강 내 장치와 유도 결합을 통해 구강 내 장치로부터 파워와 데이터를 수신하는 임플란트로 구성되어 있다. 시스템의 퍼포먼스를 평가하기 위해서, 송신 및 수신 안테나 코일 사이의 거리를 변화시키면서 총 파워 효율, 공급/수신 파워와 같은 파워와 관련된 항들이 측정하였다. 또한, 그 거리 범위에서 수신단에서 복구한 PWM 신호의 평균 duty-cycle 에러를 측정된 값을 기반으로 계산하였다. PBS 용액을 이용한 금속-전해질 계면에서 자극 전극으로써의 사용 가능성을 확인하기 위해서 시험관 내 검증이 추가적으로 수행되었다. 전기화학 임피던스 스펙트럼을 통해 전극의 임피던스, 전하 저장 용량, 그리고 전하 주입 용량을 구하고 분석하였다. 시험관 내 검증이 끝난 후에, 토끼의 연구개 자극을 위하여 생체 내 실험이 진행되었다. 예상했던 대로, 전기 자극이 인가되었을 때, 연구개 자극이 수축되는 것을 C-arm fluoroscopy를 통하여 확인할 수 있었다. 마지막으로, 개발된 장치들에 대한 몇몇의 discussion이 다루어졌다.

주요어: 폐쇄성 수면 무호흡, 생체 이식형 전자 장치, 액정 폴리머, 설하 신경 자극술, 연구개 자극술, 자기 유도 결합

학번: 2014-21648